
Article:
Keklikoglou, I., Cianciaruso, C., Güç, E. et al. (16 more authors) (2019) Chemotherapy elicits pro-metastatic extracellular vesicles in breast cancer models. Nature Cell Biology, 21 (2). pp. 190-202. ISSN 1465-7392

https://doi.org/10.1038/s41556-018-0256-3

Chemotherapy elicits pro-metastatic extracellular vesicles in breast cancer models

Ioanna **Keklikoglou**[1,*,#], Chiara **Cianciaruso**[1,*], Esra **Güç**[2], Mario Leonardo **Squadrito**[1], Laura M. **Spring**[3], Simon **Tazzyman**[4], Lore **Lambein**[4], Amanda **Poissonnier**[5], Gino B. **Ferraro**[6], Caroline **Baer**[1], Antonino **Cassará**[1], Alan **Guichard**[1], M. Luisa **Iruela-Arispe**[1,7], Claire E. **Lewis**[4], Lisa M. **Coussens**[5,8], Aditya **Bardia**[3], Rakesh K. **Jain**[6], Jeffrey W. **Pollard**[2,9], & Michele **De Palma**[1,#]

[1]Swiss Institute for Experimental Cancer Research (ISREC), School of Life Sciences, École Polytechnique Fédérale de Lausanne (EPFL), Lausanne, 1015, Switzerland.

[2]MRC Centre for Reproductive Health, Queen's Medical Research Institute, The University of Edinburgh, Scotland, EH16 4TJ, United Kingdom.

[3]Massachusetts General Hospital Cancer Center, Harvard Medical School, Boston, Massachusetts, 02114, USA.

[4]Department of Oncology and Metabolism, University of Sheffield, Medical School, Sheffield, S10 2RX, United Kingdom.

[5]Department of Cell, Developmental and Cancer Biology, Oregon Health & Sciences University, Portland, Oregon, 97239, USA.

[6]Edwin L. Steele Laboratories, Department of Radiation Oncology, Massachusetts General Hospital, Harvard Medical School, Boston, Massachusetts, 02114, USA.

[7]Department of Molecular Cell and Developmental Biology, Molecular Biology Institute, Jonsson Comprehensive Cancer Center, University of Los Angeles, California, 90024, USA.

[8]Knight Cancer Institute, Oregon Health & Science University, Portland, Oregon, 97239, USA.

[9]Department of Developmental and Molecular Biology, Albert Einstein College of Medicine, New York, 10461, USA.

*Equal contribution

[#]Correspondence: michele.depalma@epfl.ch (MDP) and ioanna.keklikoglou@epfl.ch (IK)

Abstract

Cytotoxic chemotherapy is an effective treatment for invasive breast cancer. However, experimental studies in mice also suggest pro-metastatic effects of chemotherapy. Primary tumours release extracellular vesicles (EVs), including exosomes, that can facilitate the seeding and growth of metastatic cancer cells in distant organs, but the effects of chemotherapy on tumour-derived EVs remain unclear. Here we show that two classes of cytotoxic drugs broadly employed in pre-operative (neoadjuvant) breast cancer therapy, taxanes and anthracyclines, elicit tumour-derived EVs with enhanced pro-metastatic capacity. Chemotherapy-elicited EVs are enriched in annexin-A6 (ANXA6), a Ca^{2+}-dependent protein that promotes NF-kB-dependent endothelial cell activation, *Ccl2* induction, and $Ly6C^{+}CCR2^{+}$ monocyte expansion in the pulmonary pre-metastatic niche to facilitate the establishment of lung metastasis. Genetic inactivation of *Anxa6* in cancer cells, or *Ccr2* in host cells, blunts the pro-metastatic effects of chemotherapy-elicited EVs. ANXA6 is detected, and potentially enriched, in the circulating EVs of breast cancer patients undergoing neoadjuvant chemotherapy.

Introduction

Neoadjuvant chemotherapy may provide long-term clinical benefit in patients diagnosed with invasive breast cancer, especially when the primary tumour fully regresses before surgery [1-6]. However, the therapeutic benefits of neoadjuvant chemotherapy may be limited by tumour-promoting host responses that are induced by certain cytotoxic drugs [7]. Several reports have documented pro-metastatic effects of cytotoxic agents in mouse mammary tumour models [8-13]. For example, paclitaxel (PTX), a microtubule-stabilizing drug often used in breast cancer therapy [5,6], was reported to enhance expression of vascular-endothelial growth factor receptor-1 (VEGFR1) on pulmonary endothelial cells to facilitate cancer-cell adhesion and subsequent metastasis [13]. Both PTX and doxorubicin (DOX) – an anthracycline also used in breast cancer therapy [5,6] – increased the ability of perivascular $TIE2^{+}$ macrophages [14-16] to promote cancer-cell intravasation in primary mammary tumours, resulting in heightened pulmonary metastasis [8,12]. Collectively, pre-clinical data in mouse models suggest that the pro-metastatic capacity of certain chemotherapies may involve facilitation of both cancer cell intravasation in primary tumours and extravasation to secondary, metastatic sites.

Primary tumours release extracellular vesicles (EVs) that can modulate the biology of distant organ niches to enhance seeding and growth of metastatic cancer cells [17-24]. In this study, we examined the effects of PTX and DOX on the release, properties and pro-metastatic potential of tumour-derived EVs in mouse models of chemoresistant breast cancer.

Results

PTX enhances pulmonary metastasis in mouse mammary tumour models

We examined the effects of PTX on metastasis in two mouse breast cancer models: transgenic MMTV-PyMT mice (FVB/n background), which develop multifocal mammary tumours [25-27], and

immunodeficient *Rag1*$^{-/-}$ (C57BL/6 background) or *Swiss nu/nu* mice challenged with 4T1 cancer cells [28]. In order to trace metastasis, the 4T1 cells were modified to express a fluorescent CD9-mCherry (mCh) fusion protein targeted to cellular membranes; in some experiments, 4T1 cells were further modified to express a human *ERBB2* (HER2) transgene [29]. The 4T1 tumour studies used immunodeficient mice to avoid potential anti-tumour immune responses against mCh or HER2.

Tumour-bearing mice received 3 doses of PTX (10 mg/kg) or vehicle (cremophor, CREMO) before analysis (**Fig. 1a)**. PTX had modest, if any, inhibitory activity on the growth of primary mammary tumours in both MMTV-PyMT and 4T1 models (**Fig. 1b-e**). However, it increased pulmonary tumour deposits in a fraction of the mice, in line with previous findings [8-12]. In particular, PTX increased the incidence (**Fig. 1f, g**) and mean size (**Fig. 1f, h, i**) of spontaneous metastases in lungs of MMTV-PyMT mice, as well as the seeding of mCh$^+$ 4T1 cancer cells in the lungs of tumour-bearing *Rag1*$^{-/-}$ mice (**Fig. 1j-k**), compared to vehicle. PTX also enhanced pulmonary seeding of mCh$^+$HER2$^+$ cancer cells in some tumour-bearing *Swiss nu/nu* mice (**Fig. 1l**), although it did not augment the frequency of mCh$^+$HER2$^+$ cancer cells in the systemic circulation (**Fig. 1m**). Together, these results indicate that PTX may augment, rather than limit, lung metastasis in mouse models of chemoresistant breast cancer.

Chemotherapy-elicited EVs promote mammary tumour metastasis in mice

Tumour-derived EVs facilitate metastasis of primary tumours by altering the properties of pre-metastatic niche-associated host cells [17-24]. In order to gauge the participation of tumour-derived EVs in PTX-induced mammary tumour metastasis, we used sequential ultracentrifugation to isolate EVs [30,31] from cell culture media of unmodified 4T1 cancer cells treated with either PTX or CREMO (PTX-EV and CREMO-EV, respectively). The resulting preparations were highly enriched in small EVs, as shown by both transmission electron microscopy (TEM; **Fig. 2a**) and nanoparticle tracking analysis (NTA; **Supplementary Fig. 1a**). Also, the EV-associated proteins CD9, CD81 and syntenin-1 were enriched in EVs compared to producer cells, as demonstrated by Western blotting analysis (**Supplementary Fig. 1b**). Although we cannot rule out co-purification of small apoptotic bodies, the physical and molecular properties of the preparations are consistent with *bona fide* EVs [30-32] with mode size comprised between 100 and 150 nm.

We pre-conditioned immunocompetent Balb/c mice with either PTX-EV or CREMO-EV (two doses, each corresponding to about 4x10^9 EVs; **Supplementary Fig. 1c**), followed by intravenous injection of 4T1 cells (**Fig. 2b**). In this lung colonization assay, PTX-EV increased the number of metastatic lung nodules compared to CREMO-EV (**Fig. 2c**). We then asked if PTX could also affect the pro-metastatic capacity of EVs released from an intact tumour microenvironment. To this aim, we treated MMTV-PyMT mice with PTX or CREMO (see **Fig. 1a** above), excised mammary tumours three days after the last dose, and cultured tumour-derived cell suspensions for 48h in order to isolate EVs from conditioned media (**Fig. 2d**). We assessed the purity and properties of EV preparations by TEM (**Supplementary Fig. 1d**), NTA (**Supplementary Fig. 1e-f**), and Western

blotting analysis (**Supplementary Fig. 1g**), and found no obvious differences between PTX-EV and CREMO-EV. We then pre-conditioned immunocompetent FVB/n mice with either EV preparation (**Fig. 2b**), followed by the intravenous injection of freshly isolated MMTV-PyMT tumour-derived cells. Similar to results obtained with 4T1 cells, PTX-EV increased the number of metastatic nodules in this MMTV-PyMT-based lung colonization assay (**Fig. 2e**).

Anthracyclines are broadly employed in neoadjuvant breast cancer therapy [1,5,6]. DOX, a lead anthracycline, was reported previously to modify the microenvironment of primary mammary tumours to potentially facilitate metastasis [8,33]. We treated MMTV-PyMT mice with DOX or vehicle (PBS) and purified tumour-derived DOX-EV and PBS-EV, respectively, according to the method shown in **Fig. 2d**. Similar to results obtained with PTX-EV, DOX-EV enhanced metastasis, compared to PBS-EV, in an MMTV-PyMT-based lung colonization assay (**Fig. 2f**). Of note, neither PTX nor DOX directly increased metastasis in this assay; rather, the free drugs limited, or even abated, lung colonization by MMTV-PyMT tumour-derived cells (**Fig. 2g**). These results indicate that chemotherapy-elicited, tumour-derived EVs mediate the pro-metastatic activity of the cytotoxic drugs.

PTX-elicited EVs facilitate tumour colonization in a zebrafish embryo model

Because tumour-derived EVs cannot be isolated from mouse plasma in amounts sufficient to perform EV transfer experiments in mice, we examined the pro-metastatic capacity of circulating PTX-EV in a zebrafish embryo model. In this system, cancer cells injected into the circulation extravasate to, and colonize the caudal haematopoietic area (CHA) of the tail of embryos; these events can be imaged by confocal microscopy, as embryos are translucent [34,35]. We found that PTX-EV isolated from plasma of 4T1-mCh tumour-bearing *Rag1*$^{-/-}$ mice (**Fig. 2h**) enhanced CHA colonization by human MDA-MB-435 melanoma cells stably expressing cyan fluorescent protein (CFP), compared to CREMO-EV (**Fig. 2i-l**). Of note, free PTX did not facilitate CHA colonization by cancer cells in the same assay.

PTX modulates EV release from cancer cells

We then examined the effects of chemotherapy on EV release from cancer cells. PTX increased the release of EVs from both mouse and human mammary carcinoma cell lines (**Supplementary Fig. 2a-c**). It also increased mCh fluorescence in the blood of mice carrying 4T1-mCh tumours (**Supplementary Fig. 2d-f**). In these experiments, mCh fluorescence was associated with *bona fide* EVs (**Supplementary Fig. 2g-i**) and was resistant to proteolysis (**Supplementary Fig. 2j-k**), indicating intra-vesicular localization of the CD9-mCh fusion protein.

Cytotoxic agents, including PTX, promote cancer cell death in a dose-dependent manner (**Supplementary Fig. 2a** and **Supplementary Fig. 3a-b**). Although drug-induced cell stress may influence release of EVs and other microvesicles from pre-apoptotic cells [32], PTX-induced EV release from 4T1 cells was apoptosis-independent (**Supplementary Fig. 3c**).

RAB GTPases control EV biogenesis and release in mammalian cells [36,37]. Accordingly, both basal and PTX-induced EV release were reduced in *Rab27a*-deficient 4T1 cells (**Supplementary Fig. 3d-g**). PTX may enhance EV release from cancer cells by enforcing the trafficking of intracellular vesicles to plasma membranes (**Supplementary Fig. 3h**); this process may involve the association of RAB27A with microtubules, which are stabilized by taxanes [38]. We observed enhanced EV release also from 4T1 cells exposed to a different taxane, docetaxel (**Supplementary Fig. 3i**). Conversely, DOX did not promote EV release from mammary carcinoma cells (**Supplementary Fig. 3j, k**). Therefore, whereas taxanes may increase mammary tumour metastasis by enhancing both the release and pro-metastatic properties of tumour-derived EVs, anthracyclines may do so by specifically reinforcing the pro-metastatic features of the EVs.

Chemotherapy-elicited EVs are enriched in ANXA6

Enhanced pro-metastatic capacity of chemotherapy-elicited EVs may depend on their protein repertoire. We performed proteomic analysis of 4T1-derived PTX-EV and CREMO-EV using liquid chromatography-tandem mass spectrometry (LC-MS/MS). Unsupervised clustering analysis of the EV proteomes (**Fig. 3a**) revealed substantial differences (**Supplementary Table 1**). Over-represented proteins in PTX-EVs included annexin-A6 (ANXA6; **Fig. 3b**), a Ca^{2+}-binding membrane-associated protein (**Fig. 3c**). ANXA6 controls membrane trafficking and cell signalling [39], and has been previously implicated in both the positive and negative regulation of cancer cell invasion [40-42]. Validation experiments by Western blotting revealed that ANXA6 was more robustly detected in PTX-EV compared to the producer 4T1 cells or CREMO-EV (**Fig. 3d**). Notably, both PTX and DOX promoted ANXA6 loading into EVs of 4T1 cells and the MMTV-PyMT tumour-derived cell line PyMT-IK1 (**Fig. 3e**).

Both taxanes [43] and anthracyclines [44] augment intracellular calcium ion levels. Interestingly, chemotherapy-induced ANXA6 loading into EVs was Ca^{2+}-dependent (**Fig. 3f-i**), whereas EV release *per se* was Ca^{2+}-independent (**Fig. 3j**). Western blotting and density gradient fractionation of EVs [30] purified from medium conditioned by 4T1 or 4T1-mCh cells confirmed that ANXA6 was associated with *bona fide* EVs (**Supplementary Fig. 1b** above and **Supplementary Fig. 4a-b**) and, in particular, with the inner leaflet of EVs (**Supplementary Fig. 4c-d**). Neither PTX nor DOX increased ANXA6 in EVs released by non-transformed cells, such as mouse primary bone marrow dendritic cells and embryonic fibroblasts (**Supplementary Fig. 4e-h**).

EV-associated ANXA6 promotes mammary tumour metastasis

The aforementioned results suggested a potential role for ANXA6 in modulating chemotherapy-induced mammary tumour metastasis. To test this possibility, we generated *Anxa6* knockout (KO) 4T1-mCh cells using CRISPR/Cas9 technology (**Fig. 4a**). We obtained two *Anxa6*-deficient clones (**Fig. 4b**), which were used in subsequent experiments. ANXA6 was exhaustively depleted from *Anxa6*-KO 4T1-mCh-derived EVs treated with either CREMO or PTX (**Fig. 4c**). ANXA6 deficiency in

4T1-mCh cells did not impair the enhancement of EV release by PTX (**Fig. 4d**); furthermore, *Anxa6*-proficient (WT) and KO EVs were indistinguishable based on TEM (**Fig. 4e**) and NTA (**Fig. 4f-g**).

We then isolated *Anxa6*-WT and KO EVs from 4T1-mCh cells treated *in vitro* with either PTX or DOX (or the appropriate vehicle) to pre-condition *Rag1*$^{-/-}$ mice before the intravenous injection of 4T1-mCh cells, according to a lung colonization assay (see **Fig. 2b** above). Remarkably, ANXA6 deficiency in PTX-EV or DOX-EV disrupted their capacity to facilitate lung colonization by 4T1-mCh cells (**Fig. 4h-i**). The depletion of ANXA6 from 4T1 cells (**Supplementary Fig. 4i**) did not alter loading of PTX or DOX into EVs (**Supplementary Fig. 4j**), arguing against the possibility that ANXA6-deficient EVs had compromised pro-metastatic capacity owing to changes in intravesicular drug levels, which were negligible irrespective of ANXA6 status (**Supplementary Fig. 4k**).

PTX induces CCL2 expression and Ly6C$^+$ monocyte expansion in lungs of mammary tumour-bearing mice

We analysed expression of cytokines known to facilitate mammary tumour metastasis, such as CCL2, CXCL12, CSF1 and ANGPT2 [45], in lungs of tumour-free and 4T1-mCh tumour-bearing *Rag1*$^{-/-}$ mice treated with either PTX or CREMO. PTX significantly increased *Ccl2* expression both at the mRNA (**Fig. 5a**) and protein (**Fig. 5b**) level in lungs of 4T1-mCh tumour-bearing but not tumour-free mice.

CCL2 was reported previously to enhance Ly6C$^+$CCR2$^+$ monocyte-assisted metastasis of mammary tumours [46-49]. Consistent with upregulation of CCL2, PTX increased the relative abundance of Ly6C$^+$ monocytes in lungs of 4T1-mCh tumour-bearing *Rag1*$^{-/-}$ mice, 4T1 tumour-bearing Balb/c mice, 4T1-mCh/HER2 tumour-bearing *Swiss nu/nu* mice, and transgenic MMTV-PyMT mice, compared to vehicle (**Fig. 5c-g**). Conversely, PTX did not alter the relative abundance of Ly6C$^+$ monocytes in the lungs of tumour-free mice (**Fig. 5h-i**). These results indicate that signals emanating from primary tumours are required for PTX-induced upregulation of CCL2 and expansion of Ly6C$^+$ monocytes in lungs.

Chemotherapy-elicited EVs induce pulmonary CCL2 expression and Ly6C$^+$ monocyte expansion

We examined whether the effects of PTX on CCL2 and Ly6C$^+$ monocytes were dependent on EVs. To this aim, we performed pre-conditioning studies with EVs in tumour-free mice (**Fig. 6a**). PTX-EV isolated from 4T1 or 4T1-mCh cells increased lung *Ccl2* expression in Balb/c and *Rag1*$^{-/-}$ tumour-free mice, respectively (**Fig. 6b, c**). We obtained similar results when we pre-conditioned tumour-free FVB/n mice with PTX-EV isolated *ex vivo* from MMTV-PyMT tumour-derived cells (see **Fig. 2d** above, and **Fig. 6d**). Paralleling *Ccl2* expression, the relative abundance of lung Ly6C$^+$CCR2$^+$ monocytes increased in response to PTX-EV (**Fig. 6e-i**). Notably, both *Ccl2* expression and Ly6C$^+$ monocytes were also increased in response to DOX-EV isolated *ex vivo* from MMTV-PyMT tumour-derived cells (**Fig. 6j-k**).

The pro-metastatic capacity of chemotherapy-elicited EVs is dependent on Ly6C$^+$CCR2$^+$ monocytes and ANXA6

To explore the functional involvement of Ly6C$^+$CCR2$^+$ monocytes in PTX-EV-mediated pulmonary metastasis, we performed pre-conditioning experiments with EVs in *Ccr2* KO mice (C57Bl/6 background), which have impaired monocyte-assisted mammary cancer metastasis [49]. Whereas PTX-EV derived from E0771-LG mouse mammary carcinoma cells enhanced pulmonary seeding of firefly luciferase-expressing E0771-LG:Fl cells in *Ccr2* WT mice, they failed to do so in *Ccr2* KO mice (**Fig. 6l**). Interestingly, *Ccr2* was upregulated in Ly6C$^+$ monocytes, but not other myeloid cells, that were sorted from the lungs of tumour-free FVB/n mice pre-conditioned with PTX-EV (**Fig. 6m**). These data strongly argue that Ly6C$^+$CCR2$^+$ monocytes mediate EV-induced, pulmonary mammary cancer metastasis.

Because *Anxa6* KO PTX-EV failed to enhance pulmonary colonization by 4T1-mCh cells (see **Fig. 4h-i** above), we asked whether PTX-EV-mediated effects on pulmonary CCL2 expression and Ly6C$^+$ monocyte expansion were also dependent on ANXA6 in EVs. ANXA6 deficiency in PTX-EV isolated from 4T1-mCh cells prevented *Ccl2* and *Ccr2* upregulation (**Fig. 6n**) and the increase of Ly6C$^+$ monocytes (**Fig. 6o**) in the lungs of *Rag1*$^{-/-}$ mice. Together, these results indicate that chemotherapy-induced enrichment of ANXA6 in mammary tumour-derived EVs supports a pro-metastatic cascade in the lung that is dependent on local Ly6C$^+$ monocyte expansion.

Chemotherapy-elicited EVs promote inflammatory EC activation through ANXA6 transfer

The internalization of breast cancer-derived EVs into lung endothelial cells (ECs) may influence the initial steps of pulmonary metastasis by altering the biology of those cells in the pre-metastatic niche [24,50]. We observed increased proportions of lung ECs displaying mCh fluorescence after treating 4T1-mCh tumour-bearing *Rag1*$^{-/-}$ or 4T1-mCh/HER2 tumour-bearing Swiss *nu/nu* mice with PTX, compared to CREMO (**Fig. 7a-c**).

Increased mCh fluorescence in lung ECs may denote internalization of tumour-derived EVs, a process that can occur through EV-cell fusion [51]. We then used a murine EC line, bEnd.3, to study effects of EVs on ECs. bEnd.3 cells internalized mCh$^+$ EVs in a dose-dependent manner (**Supplementary Fig. 5a, b**); interestingly, bEnd.3 cells exposed to medium conditioned by PTX-treated 4T1-mCh or PyMT-IK1-mCh cancer cells displayed higher mCh fluorescence than bEnd.3 cells exposed to medium conditioned by CREMO-treated cells (**Supplementary Fig. 5c**). Moreover, PTX-EV from either 4T1-mCh or PyMT-IK1-mCh cells were internalized by bEnd.3 cells more efficiently than matched amounts of CREMO-EV (**Supplementary Fig. 5d**). Finally, uptake of EVs by bEnd.3 cells was independent of ANXA6 (**Supplementary Fig. 5e**), suggesting that other molecules (**Supplementary Table 1**), such as integrins [38], could mediate the preferential uptake of PTX-EV.

PTX-EV isolated from either 4T1-mCh or PyMT-IK1-mCh cells transferred ANXA6 (and mCh)

to bEnd.3 cells that were made *Anxa6*-deficient using CRISPR/Cas9 (**Fig. 7d** and **Supplementary Fig. 6a-b**). Duolink proximity ligation assay, which enables imaging of protein pairs that co-localize within 40 nm, indicated that PTX-EV-mediated transfer of ANXA6 to *Anxa6* KO bEnd.3 cells was conducive to ANXA6 co-localization with the NF-kB subunit p65 (**Fig. 7e** and **Supplementary Fig. 6c-d**), consistent with the ability of ANXA6 to interact with p65 (Ref [52]). Of note, matched doses of CREMO-EV did not reveal detectable ANXA6/p65 proximity in the same assay, possibly because PTX-EV fuse more efficiently than CREMO-EV with bEnd.3 cells (see **Supplementary Fig. 5c-e** above) and contain higher amounts of ANXA6 than CREMO-EV (see **Fig. 3d-j** above).

NF-kB (p65/*Rela*) activates *Ccl2* transcription [53]. In order to gain insight into a potential mechanistic link between ANXA6 transfer to ECs and *Ccl2* upregulation, we generated *Rela* (p65) KO bEnd.3 cells, which had defective NF-kB activation and *Ccl2* expression (**Fig. 7f** and **Supplementary Fig. 6e**). PTX-EV isolated from 4T1-mCh cells failed to induce NF-kB activation (**Fig. 7g**) and *Ccl2* upregulation (**Fig. 7h**) in *Rela* KO bEnd.3 cells. Conversely, PTX-EV isolated from 4T1-mCh or PyMT-IK1 cells increased NF-kB activity and *Ccl2* expression in *Rela*-proficient bEnd.3 cells; notably, these responses required ANXA6 in EVs. Accordingly, *Anxa6* KO bEnd.3 cells had defective NF-kB activation and *Ccl2* transcription in response to tumour-necrosis factor (TNF) compared to *Anxa6* WT cells; of note, neither *Csf1* nor *Cxcl12* were regulated by ANXA6 (**Supplementary Fig. 6f-i**). Similar to PTX-EV, DOX-EV from 4T1 cells also increased *Ccl2* transcript levels (**Fig. 7i**) and NF-kB activity (**Fig. 7j**) in bEnd.3 cells. Therefore, EV-associated ANXA6 triggers an NF-kB-dependent pro-inflammatory response in ECs.

We then examined whether PTX-EV could activate *Ccl2* transcription in lung ECs, which are a source of CCL2 in mammary tumour-bearing mice [54]. We used fluorescence-activated cell sorting (FACS) to isolate lung ECs of tumour-free FVB/n mice pre-conditioned with MMTV-PyMT tumour-derived PTX-EV or CREMO-EV (see **Fig. 2d** above) and found enhanced *Ccl2* expression in lung ECs exposed to PTX-EV (**Fig. 7k**). Taken together, these findings suggest that chemotherapy-elicited tumour EVs promote pro-inflammatory EC activation, CCL2 upregulation, Ly6C$^+$ monocyte accumulation, and tumour colonization at metastatic sites through a mechanism involving horizontal transfer of EV-associated ANXA6 to the pulmonary endothelium.

Chemotherapy-elicited EVs display broad cellular tropism in tumour-bearing mice

Besides ECs, other lung-resident cells may mediate metastasis in response to chemotherapy-induced EVs. Indeed, CD11b$^+$Gr1$^-$ lung macrophages/monocytes also internalized mCh$^+$ EVs in PTX-treated, 4T1-mCh *Rag1*$^{-/-}$ or 4T1-mCh/HER2 Swiss *nu/nu* tumour-bearing mice (**Supplementary Fig. 7a-b**). Moreover, PTX-EV isolated from MMTV-PyMT tumour-derived cells upregulated interleukin-6 (*Il6*) expression in the lung (**Supplementary Fig. 7c**) and, specifically, lung-associated non-alveolar macrophages (**Supplementary Fig. 7d**) of tumour-free FVB/n mice; of note, IL-6 was previously implicated in chemotherapy resistance [55] and macrophage-assisted mammary tumour metastasis [47,56].

Finally, PTX-EV transferred mCh to liver sinusoidal ECs more efficiently than CREMO-EV (**Supplementary Fig. 7e, f**), suggesting that chemotherapy-elicited EVs might also promote breast cancer metastasis to the liver. However, the rapid growth kinetics of both primary tumours and pulmonary metastasis in the breast cancer models employed in our study complicate the assessment of slow-growing liver metastases.

ANXA6 is detected in circulating EVs of breast cancer patients undergoing neoadjuvant chemotherapy

We finally investigated effects of chemotherapy on EV-associated ANXA6 in human breast cancer cells and patients with breast cancer. Both PTX and DOX increased ANXA6 protein levels in EVs released by human MDA-MB-231 breast cancer cells (**Fig. 8a**). Furthermore, EVs purified from the plasma of breast cancer patients undergoing neoadjuvant chemotherapy (**Supplementary Table 2** and **Fig. 8b**) had increased ANXA6 content by LC-MS/MS in five out of six cases, compared to pre-treatment levels (**Fig. 8c**, **Supplementary Fig. 8** and **Supplementary Table 3**). Because we could isolate limited amounts of EVs from each sample, we were only able to verify the LC-MS/MS data by Western blotting in one case (patient #56; **Fig. 8d**). Notably, ANXA6 levels in the EVs decreased at the end of neoadjuvant therapy in the patients who achieved a partial or complete response (five out of six), probably reflecting shrinkage of the tumour in response to chemotherapy. Also, the finding that EV-associated ANXA6 levels increased on-therapy in one patient with progressive disease (#52) strongly suggested that EV-associated ANXA6 was, in fact, of cancer cell origin. While limited, these data support the notion that chemotherapy augments ANXA6 levels in circulating EVs of patients with breast cancer.

Discussion

Neoadjuvant chemotherapy improves the management of invasive breast cancer by inducing pathological complete responses associated with significantly reduced risk of recurrence in a fraction of the patients [1-6]. However, therapy-induced host responses [7], such as those described in our study, may limit the benefits of pre-operatory treatments in some patients. It is tempting to speculate that human primary breast tumours that fail to readily regress on neoadjuvant chemotherapy (a condition of partial or complete chemoresistance) may also release pro-metastatic EVs that, in turn, facilitate seeding, survival or early colonization of metastatic niches by chemoresistant cancer cells. However, it should be cautioned that we did not study mouse survival in association with the various treatments, so we currently ignore whether increased metastatic seeding and outgrowth in response to chemotherapy-elicited EVs would translate into shorter survival in our experimental cancer models.

The potential participation of tumour-derived EVs in the process of human breast cancer metastasis is currently poorly understood and may be challenging to explore, given the lack of validated breast-cancer-specific EV markers [57]. In the future, chemotherapy-elicited EVs might

provide biomarkers for predicting metastasis risk associated with neoadjuvant chemotherapy in patients who do not achieve a complete response. Interestingly, ANXA6 has been detected in EVs isolated from the MDA-MB-231-derived clone 4175, which has lung tropism [20]. Furthermore, EV-associated ANXA6 has been implicated in the progression of pancreatic cancer in a mouse model [42]. The significance of EV-associated ANXA6 for breast cancer metastasis may, therefore, merit further investigation.

Acknowledgements

We thank C. Rmili-Wyser, A. Bellotti, B. Torchia, D. Laoui (M.D.P.'s laboratory) and M. Duquette (R.K.J.'s laboratory) for help with some experiments; T. Kitamura (University of Edinburgh, United Kingdom) for advice on lung colonization assays and for providing E0771-LG and E0771-LG:Fl cells; and H. G. Augustin (DKFZ, Heidelberg, Germany) for critical comments on the manuscript.

The EPFL core facilities of flow cytometry (FCCF), histology (HCF) and bioimaging/optics platform (BIOp) are acknowledged for skilled technical assistance; R. Hamelin and M. Moniatte of the proteomics facility (PCF, EPFL) for performing LC-MS/MS on EVs; T. J. Chico for providing access to zebrafish lines in the aquarium at the University Sheffield, UK; and R. Klemke for the kind gift of CFP-MDA-MB-435 cells.

This work was primarily funded by grants from the Swiss Cancer League (KFS-3007-08-2012), Swiss National Science Foundation (SNF 31003A-165963), and European Research Council (ERC EVOLVE-72505) to M.D.P. L.M.S. was supported by NIH Grant KL2 TR001100. C.E.L. acknowledges support from Cancer Research UK (C11712/A13028), Yorkshire Cancer Research (S382), and Breast Cancer Now (2016MayPR746 and 2016NovPCC003). M.L.I.-A. was supported by NIH (NCI 1R01CA197943). L.M.C. acknowledges support from a DOD BCRP Era of Hope Scholar Expansion Award (W81XWH-08-PRMRP-IIRA), Susan B Komen Foundation (KG110560), and Breast Cancer Research Foundation. A.B was supported by Susan B Komen Foundation (CCR15224703). R.K.J. acknowledges support from the Ludwig Center at Harvard, National Foundation for Cancer Research, and NCI (R35CA197743). J.W.P. was supported by the Wellcome Trust (101067/Z/13/Z) and MRC (MR/N022556/1).

Author Contributions

I.K. designed and performed most of the experiments, analysed and interpreted data, and wrote the manuscript. C.C. designed and performed experiments, analysed and interpreted data, and wrote the manuscript. E.G. and J.W.P. designed, performed and analysed experiments in *Ccr2* KO mice. M.L.S. designed lentiviral vectors for gene knockout, overexpression and reporter activity. A.C., C.B., A.G. and G.B.F. assisted with some experiments. A.P. and L.M.C. designed, performed and analysed experiments in MMTV-PyMT mice ("OHSU cohort"). S.T., L.L., and C.E.L designed, performed and analysed zebrafish experiments. M.L.I.-A. designed and performed some experiments while on sabbatical in M.D.P.'s laboratory. L.M.S., A.B and R.K.J. provided clinical

samples, discussed and interpreted the results. All authors provided intellectual input, reviewed the data and the manuscript. M.D.P. designed, supervised and coordinated research, interpreted the data, and wrote the manuscript.

Competing interests

L.M.S. reports consulting fees from Novartis. L.M.C. is a paid consultant for Cell Signaling Technologies; received reagent support from Plexxikon and NanoString Technologies; and is a member of the Scientific Advisory Boards of Syndax Pharmaceuticals, Carisma Therapeutics, and Verseau Therapeutics. A.B. reports consulting fees from Genentech/Roche, Immunomedics, Novartis, Pfizer, Merck, Radius Health, Spectrum Pharma and Taiho Pharma; and received a research grant from Biothernostics. R.K.J. received honoraria from Amgen and consultancy fees from Merck, Ophthotech, Pfizer, SPARC, SynDevRx, XTuit; owns equity in Enlight, Ophthotech, SynDevRx; and serves on the Boards of Trustees of Tekla Healthcare Investors, Tekla Life Sciences Investors, Tekla Healthcare Opportunities Fund, Tekla World Healthcare Fund. M.D.P. reports honoraria from Merck and Sanofi/Regeneron Pharmaceuticals; received sponsored research grants from Hoffmann La-Roche, MedImmune and Deciphera Pharmaceuticals; and serves on the Scientific Advisory Boards of Deciphera Pharmaceuticals and Genenta.

The other authors declare no competing interests. Neither materials nor funding from the above organizations were used in this study.

Figure legends

Figure 1. PTX enhances pulmonary metastasis in mammary tumour-bearing mice

a. Drug scheduling in tumour-bearing mice.

b. Cumulative weight of multifocal mammary tumours (mean ± s.e.m.) in MMTV-PyMT mice. CREMO, n=14 mice; PTX, n=16. Each dot represents one mouse carrying several tumours. Data show two independent experiments combined (EPFL cohort).

c. Volume of 4T1 or 4T1-mCh tumours (mean ± s.e.m.; n=7 mice/group) in untreated *Rag1*$^{-/-}$ mice.

d. Weight of 4T1-mCh tumours (mean ± s.e.m.) in *Rag1*$^{-/-}$ mice. CREMO, n=12 mice; PTX, n=14. Data show two independent experiments combined.

e. Weight of 4T1 (n=4) or 4T1-mCh/HER2 tumours (mean ± s.e.m.) in *Swiss nu/nu* mice. PBS, n=7 mice; CREMO, n=8; PTX, n=9. Statistical analysis by one-way ANOVA with Tukey's multiple comparison test.

f. Representative hematoxylin/eosin (H&E) images of lung sections of MMTV-PyMT mice from the experiment shown in (b). Scale bars, 1 mm. Data are quantified in (g) and (h).

g-i. Number (g) and mean area (h, i) of pulmonary metastases (mean ± s.e.m.) in MMTV-PyMT mice. (g, h): CREMO, n=14 mice; PTX, n=16; two independent experiments combined (EPFL cohort). (i): PBS, n=21; PTX, n=49; five independent experiments combined (OHSU cohort). Statistical analysis in (g) and (i) by unpaired two-tailed Student's t-test.

j. Fluorescence-activated cell sorting (FACS) analysis of mCh^{+}CD31^{-} cancer cells (mean ± s.e.m.; relative to viable CD45^{-} lung-derived cells) in lungs of 4T1-mCh tumour-bearing mice. CREMO, n=8 mice; PTX, n=9. Statistical analysis as in (g). The FACS panels on the right show the gating strategy.

k. Representative confocal immunofluorescence images showing mCh^{+} (red) 4T1 cancer cells in lung sections of mice from the experiment in (j). Nuclei are stained with DAPI (blue). Scale bars, 200 µm (left and middle panel) and 50 µm (right panel).

l. FACS analysis of mCh^{+}CD31^{-} cancer cells (mean ± s.e.m.) in lungs of 4T1 (n=4) or 4T1-mCh/HER2 tumour-bearing mice. PBS, n=7 mice; CREMO, n=8; PTX, n=9.

m. FACS analysis of mCh^{+}HER2^{+}CD45^{-} cancer cells (mean ± s.e.m.; absolute cell counts) in blood of 4T1-mCh/HER2 tumour-bearing mice. PBS, n=7 mice; CREMO, n=8; PTX, n=9. The FACS panels on the right show the gating strategy.

Source data are shown in **Supplementary Table 5**.

Figure 2. Chemotherapy-elicited EVs are pro-metastatic in mouse and zebrafish tumour model

a. TEM images of CREMO-EV (n=1 biological sample) and PTX-EV (n=2 independent biological samples) isolated from 4T1 cells. One representative image is shown for each EV type. Bottom panels show magnified fields of upper panels. Scale bars, 200 nm (upper panels) and 100 nm

(bottom panels).

b. Schematics illustrating lung pre-conditioning and tumour colonization assays.

c. Number of 4T1 metastatic nodules (mean ± s.e.m.; n=8 mice/group) in lungs of pre-conditioned Balb/c mice. Statistical analysis by unpaired two-tailed Student's t-test. Right panels show representative H&E images of lung sections (magnified fields below). Scale bars, 1 mm.

d. Procedure to isolate tumour-derived EVs from chemotherapy-treated MMTV-PyMT mice.

e, f. Number of MMTV-PyMT metastatic nodules (mean ± s.e.m.) in lungs of pre-conditioned FVB/n mice; CREMO-EV, n=13 mice; PTX-EV, n=14; PBS-EV, n=8; DOX-EV, n=9. Statistical analysis as in (c). Lower panels in (e) show representative H&E images of lung sections. Scale bars, 1 mm.

g. Number of MMTV-PyMT metastatic nodules (mean ± s.e.m.) in lungs of pre-conditioned FVB/n mice. PBS, n=9 mice; CREMO 1, n=9; CREMO 10, n=8; PTX 1 mg/kg, n=9; PTX 10 mg/kg, n=9; DOX, n=9. CREMO 1 and 10 are the vehicle controls for 1 and 10 mg/kg PTX, respectively. Statistical analysis by one-way ANOVA with Tukey's multiple comparison test.

h. Concentration (mean ± s.e.m.; n=5 acquisitions of one sample/condition) and size distribution of EVs isolated from plasma of 4T1-mCh tumour-bearing mice treated as indicated, determined by NTA.

i. Schematics illustrating experiments in zebrafish embryos.

j. Volume of tumour deposits (mean ± s.e.m.) in embryos injected with CREMO-EVs (n=24), PTX-EVs (n=22), CREMO (n=12) or PTX (n=12), determined by confocal imaging analysis. Statistical analysis as in (g).

k. Confocal image of a representative zebrafish embryo injected with CFP^+ MDA-MB-453 cells (blue). Blood vessels are GFP^+ (green). The right panel shows the caudal haematopoietic area (CHA) with CFP^+ tumour deposits. Scale bar, 0.5 mm.

l. Representative confocal images of the CHA of zebrafish embryos, imaged as in (k). Scale bar, 70 μm. Quantitative data are shown in (j).

Source data are shown in **Supplementary Table 5**.

Figure 3. PTX enriches ANXA6 in EVs in a Ca^{2+}-dependent manner

a. Unsupervised clustering of proteins in CREMO-EV and PTX-EV (n=6 independent EV preparations/condition) from 4T1 cells, determined by LC-MS/MS analysis.

b. LC-MS/MS analysis of CREMO-EV and PTX-EV (n=6 independent EV preparations) showing total spectrum count (mean ± s.d.) of ANXA6, CD9 and CD81. Statistical analysis by two-way ANOVA with Sidak's multiple comparison test.

c. Western blotting analysis of ANXA6, calnexin (CANX), GAPDH and RAB7 in 4T1 cells treated with CREMO or PTX for 24h before subcellular fractionation. The "membranes" fraction encompasses early and late endosomes, endoplasmic reticulum and mitochondria. The experiment was performed once.

d. Western blotting analysis of ANXA6 and CD9 in CREMO- or PTX-treated 4T1 cells, or matched

CREMO-EV or PTX-EV. Additional experiments are shown in Fig. 3e, f, h; Fig. 4c; and Supplementary Fig. 1b.

e. Western blotting analysis of ANXA6 and CD81 in the indicated EV preparations isolated from either 4T1 or PyMT-IK1 cells.

f. Western blotting analysis of the indicated proteins in PyMT-IK1 cells and matched EVs 48h after treatment of the cells with PBS, CREMO, PTX, DMSO or DOX, with or without the calcium chelator BAPTA-AM. One representative experiment is shown of three performed for EVs and one for cells.

g. ANXA6 band intensity (mean ± s.d.; n=3 independent experiments, one of which is shown in (f) above) in the indicated EV preparations analysed by Western blotting. Statistical analysis as in (b).

h. Western blotting analysis of EVs from 4T1 cells treated for 48h with PBS, CREMO or PTX, with or without BAPTA-AM. One representative experiment is shown of three performed.

i. ANXA6 band intensity (normalized to CD81; mean ± s.d.; n=3 independent experiments, one of which is shown in (h) above) in the indicated EV preparations. Statistical analysis as in (b).

j. Protein content by BCA (left panel) and concentration by NTA (right panel) of the indicated EVs (mean ± s.d.; n=3 independent EV preparation/condition) obtained from 4T1 cells treated with or without BAPTA-AM. Statistical analysis as in (b).

Source data are shown in **Supplementary Table 5**. Unprocessed blots are shown in **Supplementary Fig. 9**.

Figure 4. EV-associated ANXA6 promotes mammary tumour metastasis

a. Schematics of the lentiviral vectors used to disrupt the expression of *Anxa6*, *Rab27a* or *Rela* in cells.

b, c. Western blotting analysis of ANXA6, GAPDH and CD81 in 4T1-mCh cells (b) or secreted EVs (c). *Anxa6*-WT (parental line) and two independent *Anxa6*-KO clones are shown, either untreated (b) or treated as indicated (c). The experiments were performed once.

d. mCh mean fluorescence intensity (MFI; left y axis) and concentration by NTA (right y axis) of EVs (mean ± s.d.; n=3 independent cell cultures/condition) released by *Anxa6*-KO 4T1-mCh cells (clone #1) treated for 72h with CREMO or PTX. Statistical analysis by unpaired two-tailed Student's t-test.

e. Representative wide-field TEM images of the indicated EVs isolated from *Anxa6*-WT (top panels) or *Anxa6*-KO (clone #1, bottom panels) 4T1-mCh cells. Scale bars, 200 nm. The experiment was performed once.

f. Mode size (mean values ± s.d.) of the indicated EVs isolated from *Anxa6*-WT (top panel) or *Anxa6*-KO (clone #1, bottom panel) 4T1-mCh cells, determined by NTA. Data show results from n=5 (*Anxa6*-WT) and n=3 (*Anxa6*-KO) independent EV preparations.

g. Concentration (mean ± s.e.m.; n=3 acquisitions of one sample/condition) and size distribution of EVs isolated from medium conditioned by CREMO- or PTX-treated *Anxa6*-KO 4T1-mCh cells (clone #1), determined by NTA.

h. mCh^+ metastatic area fraction per lung section (mean ± s.e.m.) in *Rag1*$^{-/-}$ mice pre-conditioned

with the indicated EVs. CREMO-EV/*Anxa6*-WT, n=7 mice; PTX-EV/*Anxa6*-WT, n=7; CREMO-EV/*Anxa6*-KO (clone #1), n=7; PTX-EV/*Anxa6*-KO (clone #1), n=7. Statistical analysis by two-way ANOVA with Tukey's multiple comparison test. Representative images of lung sections stained with DAPI (white) are shown on the right; the mCh signal (red) was acquired as direct fluorescence. Scale bars, 1 mm.

i. mCh^+ metastatic area fraction per lung section (mean ± s.e.m.) in *Rag1*$^{-/-}$ mice pre-conditioned with EVs. DMSO-EV/*Anxa6*-WT, n=7 mice; DOX-EV/*Anxa6*-WT, n=8; DMSO-EV/*Anxa6*-KO (clone #1), n=8; DOX-EV/*Anxa6*-KO (clone #1), n=8. Statistical analysis as in (h).

Source data are shown in **Supplementary Table 5**. Unprocessed blots are shown in **Supplementary Fig. 9**.

Figure 5. PTX induces CCL2 expression and Ly6C$^+$ monocyte expansion in lungs of mammary tumour-bearing mice

a. Quantitative polymerase chain reaction (qPCR) analysis of the indicated genes (mean ± s.e.m.) in lungs of either tumour-free (TF) or 4T1 tumour-bearing (TB) mice treated as indicated. TF + CREMO, n=5 mice; TF + PTX, n=5; TB + CREMO, n=8; TB + PTX, n=9. Statistical analysis by two-way ANOVA with Tukey's multiple comparison test.

b. ELISA-based CCL2 protein (mean ± s.e.m.) in lungs of mice treated as in (a). Tumour-free + CREMO, n=5 mice; Tumour-free + PTX, n=5; Tumour-bearing + CREMO, n=6; Tumour-bearing + PTX, n=6. Statistical analysis as in (a).

c. FACS analysis of $CD45^+CD11b^+Ly6C^+Ly6G^-F4/80^+$ monocytes ($Ly6C^+$ Mo) in lungs of tumour-bearing mice. A representative sample is shown to illustrate the gating strategy. FMO, fluorescence minus one.

d-g. FACS analysis of $Ly6C^+$ Mo (mean ± s.e.m.) in tumour-bearing mice treated as indicated. Data show the frequency of $Ly6C^+$ monocytes in the $CD45^+$ population, relative to control (CREMO or PBS). (d): CREMO, n=7 mice; PTX, n=8. (e): PBS, n=5; CREMO, n=5; PTX, n=5. (f): PBS, n=7; CREMO, n=8; PTX, n=9. (g): CREMO, n=13; PTX, n=14. Statistical analysis by unpaired two-tailed Student's t-test (d, g) or one-way ANOVA with Tukey's multiple comparison test (e, f). Data in (g) show three independent experiments combined.

h, i. FACS analysis of $Ly6C^+$ Mo (mean ± s.e.m.) in lungs of tumour-free FVB/n (h) or *Rag1*$^{-/-}$ (i) mice treated as indicated and analysed two days after treatment. (h): PBS, n=12 mice; CREMO, n=6; PTX 1 mg/kg, n=8; PTX 10 mg/kg, n=6; DOX, n=6. (i): CREMO, n=5; PTX, n=5. Statistical analysis by one-way ANOVA with Tukey's multiple comparison test (h) or unpaired two-tailed Student's t-test (i).

Source data are shown in **Supplementary Table 5**.

Figure 6. Ly6C$^+$ monocytes mediate the pro-metastatic activity of chemotherapy-elicited EVs

a. Schematics of EV pre-conditioning studies in tumour-free mice.

b-d. qPCR analysis of *Ccl2* (mean ± s.e.m.) in lungs of tumour-free mice that received EVs. (b): CREMO-EV, n=8; PTX-EV, n=9. (c): CREMO-EV, n=8; PTX-EV, n=7. (d): CREMO-EV, n=10; PTX-EV, n=9. Statistical analysis by unpaired two-tailed Student's t-test.

e-g. FACS analysis of Ly6C$^+$ Mo (mean ± s.e.m.) in lungs of tumour-free mice that received EVs. (e): CREMO-EV, n=8; PTX-EV, n=9. (f): CREMO-EV, n=6; PTX-EV, n=7. (g): PBS (no EVs), n=11; CREMO-EV, n=14; PTX-EV, n=15. Statistical analysis by unpaired two-tailed Student's t-test (e, f) or one-way ANOVA with Tukey's multiple comparison test (g).

h. qPCR analysis of *Ccr2* (mean ± s.e.m.) in lungs of mice that received MMTV-PyMT tumour-derived CREMO-EV (n=10) or PTX-EV (n=9). Statistical analysis as in (b).

i. Correlation between *Ccl2* and *Ccr2* transcript levels in lungs of FVB/n mice shown in (d) and (h). The Pearson correlation coefficient (r) is indicated.

j, k. qPCR analysis of *Ccl2* (j) and FACS analysis of Ly6C$^+$ Mo (k) in the lungs of tumour-free mice (mean ± s.e.m.) that received PBS-EV (n=5) or DOX-EV (n=5). Statistical analysis as in (b).

l. Bioluminescence (BL) analysis (total photon flux; mean ± s.e.m.) of *Ccr2* WT or KO mice pre-conditioned with EVs, analysed at day 10 post-cell injection. The right panel shows representative mice. CREMO-EV/*Ccr2*-WT, n=10; PTX-EV/*Ccr2*-WT, n=11; CREMO-EV/*Ccr2*-KO, n=7; PTX-EV/*Ccr2*-KO, n=8. Statistical analysis by two-way ANOVA with Tukey's multiple comparison test. Data show three independent experiments combined.

m. qPCR analysis of *Ccr2* (mean ± s.e.m.) in myeloid cells (Ly6C$^+$ Mo; Ly6C^{low} Mo; and non-alveolar macrophages, Mac) FACS-sorted from lungs of tumour-free mice that received MMTV-PyMT tumour-derived CREMO-EV (n=5; except for Mac, n=4) or PTX-EV (n=6). Statistical analysis as in (l).

n, o. qPCR analysis of *Ccl2* and *Ccr2* (n) and FACS analysis of Ly6C$^+$ Mo (o) in lungs of mice (mean ± s.e.m; n=6 mice) that received CREMO-EV or PTX-EV from either *Anxa6*-WT or *Anxa6*-KO 4T1-mCh cells. Statistical analysis by two-way ANOVA with Sidak's multiple comparison test.

Source data are shown in **Supplementary Table 5**.

Figure 7. Chemotherapy-elicited EVs promote inflammatory EC activation through ANXA6 transfer

a. FACS of mCh$^+$ ECs (mean ± s.e.m.) in lungs of 4T1 (n=6) or 4T1-mCh (CREMO, n=8; PTX, n=9) tumour-bearing *Rag1*$^{-/-}$ mice. Statistical analysis by one-way ANOVA with Tukey's multiple comparison test. Right panels show gating strategy.

b. Representative confocal images of anti-CD31 endothelial (green) and anti-mCh (magenta) immunostaining of lung sections from 4T1-mCh tumour-bearing mice treated as in (a); nuclei are stained with DAPI (blue). Scale bars, 10 μm.

c. FACS of mCh$^+$ ECs (mean ± s.e.m.) in lungs of 4T1 (n=4) or 4T1-mCh/HER2 (PBS, n=7; CREMO, n=8; PTX, n=9) tumour-bearing *Swiss nu/nu* mice. Statistical analysis as in (a).

d. Western blotting analysis of the indicated proteins in *Anxa6*-KO bEnd.3 cells. The experiment was

performed twice; Supplementary Fig. 6b shows a replicate experiment.

e. Duolink staining of *Anxa6*-KO bEnd.3 cells showing ANXA6/p65 proximity (number of white dots/cell; mean ± s.e.m.; n=8 randomly selected images, each containing at least 12 cells). Statistical analysis as in (a). Right panels show representative images; nuclei are stained with DAPI (blue). Scale bars, 30 μm. Data show one experiment of two performed.

f. Western blotting analysis of p65 (left), NF-kB activity (middle), and qPCR of *Ccl2* (right) in bEnd.3 cells (mean ± s.d.; n=3 independent cell cultures/condition). Statistical analysis by unpaired two-tailed Student's t-test.

g, h. NF-kB activity (g) and qPCR of *Ccl2* (h) in bEnd.3 cells (mean ± s.d.; n=3 independent cell cultures/condition). Statistical analysis by two-way ANOVA with Sidak's multiple comparison test. Data show one experiment of two (g) or three (h) performed.

i, j. qPCR analysis of *Ccl2* (i) and NF-kB activity (j) in bEnd.3 cells (mean ± s.d.; n=3 independent cell cultures/condition). Statistical analysis by two-way ANOVA with Tukey's multiple comparison test (i, left panel) or unpaired two-tailed Student's t-test (i, right panel; and j).

k. qPCR of *Ccl2* in $mCh^{+}CD31^{+}CD45^{-}$ ECs sorted from lungs of FVB/n mice (mean ± s.e.m.; n=5 mice). Statistical analysis by unpaired one-tailed Student's t-test. Right panel shows the purity of the sorted ECs.

Source data are shown in **Supplementary Table 5**. Unprocessed blots are shown in **Supplementary Fig. 9**.

Figure 8. ANXA6 is detected in circulating EVs of breast cancer patients undergoing neoadjuvant chemotherapy

a. Western blotting analysis of EVs isolated from MDA-MB-231 cells treated as indicated. The experiment was performed three times for PTX and once for DOX.

b. Schematic of the treatment timeline and time-points of blood collection in breast cancer patients (n=6). AC, anthracycline (DOX) plus cyclophosphamide.

c. LC-MS/MS-based quantification of ANXA6 in EVs isolated from plasma of breast cancer patients (n=6) before chemotherapy (pre-treatment), after AC, and after PTX. The data show quantitative values of ANXA6 presented as fold-change *versus* pre-treatment level. Note that the amount of EVs that could be isolated from patient #38 after PTX was insufficient to perform LC-MS/MS analysis. Tumour response was assessed at the time of surgery.

d. Western blotting analysis of ANXA6 in plasma EVs of one patient (#56), analysed at the indicated time-points. The experiment was performed once.

Source data are shown in **Supplementary Table 5**. Unprocessed blots are shown in **Supplementary Fig. 9**.

References

1 Rastogi, P. *et al.* Preoperative chemotherapy: updates of National Surgical Adjuvant Breast and Bowel Project Protocols B-18 and B-27. *J Clin Oncol.* **26**, 778-785 (2008).
2 Fisher, E. R. *et al.* Pathobiology of preoperative chemotherapy: findings from the National Surgical Adjuvant Breast and Bowel (NSABP) protocol B-18. *Cancer* **95**, 681-695 (2002).
3 DeMichele, A., Yee, D. & Esserman, L. Mechanisms of Resistance to Neoadjuvant Chemotherapy in Breast Cancer. *N Engl J Med.* **377**, 2287-2289 (2017).
4 Spring, L. *et al.* Pathologic Complete Response After Neoadjuvant Chemotherapy and Long-Term Outcomes Among Young Women With Breast Cancer. *J Natl Compr Canc Netw.* **15**, 1216-1223 (2017).
5 Zardavas, D. & Piccart, M. Neoadjuvant therapy for breast cancer. *Annu Rev Med.* **66**, 31-48 (2015).
6 Gampenrieder, S. P., Rinnerthaler, G. & Greil, R. Neoadjuvant chemotherapy and targeted therapy in breast cancer: past, present, and future. *J Oncol.* **2013**, 732047 (2013).
7 Shaked, Y. Balancing efficacy of and host immune responses to cancer therapy: the yin and yang effects. *Nat Rev Clin Oncol.* **13**, 611-626 (2016).
8 Karagiannis, G. S. *et al.* Neoadjuvant chemotherapy induces breast cancer metastasis through a TMEM-mediated mechanism. *Sci Transl Med.* **9**, doi:10.1126/scitranslmed.aan0026 (2017).
9 Voloshin, T. *et al.* Blocking IL1beta Pathway Following Paclitaxel Chemotherapy Slightly Inhibits Primary Tumor Growth but Promotes Spontaneous Metastasis. *Mol Cancer Ther* **14**, 1385-1394 (2015).
10 Volk-Draper, L. *et al.* Paclitaxel therapy promotes breast cancer metastasis in a TLR4-dependent manner. *Cancer Re.* **74**, 5421-5434 (2014).
11 Liu, G. *et al.* Specific chemotherapeutic agents induce metastatic behaviour through stromal- and tumour-derived cytokine and angiogenic factor signalling. *J Pathol.* **237**, 190-202 (2015).
12 Chang, Y. S., Jalgaonkar, S. P., Middleton, J. D. & Hai, T. Stress-inducible gene Atf3 in the noncancer host cells contributes to chemotherapy-exacerbated breast cancer metastasis. *Proc Natl Acad Sci U S A.* **114**, E7159-E7168 (2017).
13 Daenen, L. G. *et al.* Chemotherapy enhances metastasis formation via VEGFR-1-expressing endothelial cells. *Cancer Res.* **71**, 6976-6985 (2011).
14 De Palma, M., Biziato, D. & Petrova, T. V. Microenvironmental regulation of tumour angiogenesis. *Nature Rev Cancer* **17**, 457-474 (2017).
15 De Palma, M. *et al.* Tie2 identifies a hematopoietic lineage of proangiogenic monocytes required for tumor vessel formation and a mesenchymal population of pericyte progenitors. *Cancer Cell* **8**, 211-226 (2005).
16 Harney, A. S. *et al.* Real-Time Imaging Reveals Local, Transient Vascular Permeability, and Tumor Cell Intravasation Stimulated by TIE2hi Macrophage-Derived VEGFA. *Cancer Discov.* **5**, 932-943 (2015).
17 Costa-Silva, B. *et al.* Pancreatic cancer exosomes initiate pre-metastatic niche formation in the liver. *Nat Cell Biol.* **17**, 816-826 (2015).
18 Becker, A. *et al.* Extracellular Vesicles in Cancer: Cell-to-Cell Mediators of Metastasis. *Cancer Cell* **30**, 836-848 (2016).
19 Tkach, M. & Thery, C. Communication by Extracellular Vesicles: Where We Are and Where We Need to Go. *Cell* **164**, 1226-1232 (2016).
20 Hoshino, A. *et al.* Tumour exosome integrins determine organotropic metastasis. *Nature* **527**, 329-335 (2015).
21 Yokoi, A. *et al.* Malignant extracellular vesicles carrying MMP1 mRNA facilitate peritoneal dissemination in ovarian cancer. *Nature Commun.* **8**, 14470 (2017).
22 Zhou, W. *et al.* Cancer-secreted miR-105 destroys vascular endothelial barriers to promote metastasis. *Cancer Cell* **25**, 501-515 (2014).
23 Kalluri, R. The biology and function of exosomes in cancer. *J Clin Invest* **126**, 1208-1215 (2016).
24 Peinado, H. *et al.* Pre-metastatic niches: organ-specific homes for metastases. *Nat Rev Cancer* **17**, 302-317 (2017).
25 Guy, C. T., Cardiff, R. D. & Muller, W. J. Induction of mammary tumors by expression of polyomavirus middle T oncogene: a transgenic mouse model for metastatic disease. *Mol Cell Biol.* **12**, 954-961 (1992).
26 Lin, E. Y. *et al.* Progression to malignancy in the polyoma middle T oncoprotein mouse breast cancer model provides a reliable model for human diseases. *Am J Pathol.* **163**, 2113-2126 (2003).
27 DeNardo, D. G. *et al.* Leukocyte complexity predicts breast cancer survival and functionally regulates response to chemotherapy. *Cancer Discov.* **1**, 54-67 (2011).
28 Pulaski, B. A. & Ostrand-Rosenberg, S. Mouse 4T1 breast tumor model. *Current protocols in immunology* **Chapter 20**, Unit 20 22, doi:10.1002/0471142735.im2002s39 (2001).
29 Squadrito, M. L., Cianciaruso, C., Hansen, S. K. & De Palma, M. EVIR: chimeric receptors that enhance dendritic cell cross-dressing with tumor antigens. *Nat Methods* **15**, 183-186 (2018).
30 Kowal, J. *et al.* Proteomic comparison defines novel markers to characterize heterogeneous populations of extracellular vesicle subtypes. *Proc Natl Acad Sci U S A.* **113**, E968-977 (2016).
31 Thery, C., Amigorena, S., Raposo, G. & Clayton, A. Isolation and characterization of exosomes from cell

culture supernatants and biological fluids. *Current protocols in cell biology* **Chapter 3**, Unit 3 22 (2006).
32 Montermini, L. *et al.* Inhibition of oncogenic epidermal growth factor receptor kinase triggers release of exosome-like extracellular vesicles and impacts their phosphoprotein and DNA content. *J Biol Chem* **290**, 24534-24546 (2015).
33 Nakasone, E. S. *et al.* Imaging tumor-stroma interactions during chemotherapy reveals contributions of the microenvironment to resistance. *Cancer Cell* **21**, 488-503 (2012).
34 White, R., Rose, K. & Zon, L. Zebrafish cancer: the state of the art and the path forward. *Nat Rev Cancer* **13**, 624-636 (2013).
35 Teng, Y. *et al.* Evaluating human cancer cell metastasis in zebrafish. *BMC Cancer* **13**, 453 (2013).
36 Bobrie, A. *et al.* Rab27a supports exosome-dependent and -independent mechanisms that modify the tumor microenvironment and can promote tumor progression. *Cancer Res.* **72**, 4920-4930 (2012).
37 Ostrowski, M. *et al.* Rab27a and Rab27b control different steps of the exosome secretion pathway. *Nat Cell Biol* **12**, 19-30 (2010).
38 van Niel, G., D'Angelo, G. & Raposo, G. Shedding light on the cell biology of extracellular vesicles. *Nat Rev Mol Cell Biol.* **19**, 213-228 (2018).
39 Gerke, V. & Moss, S. E. Annexins: from structure to function. *Physiol Rev.* **82**, 331-371 (2002).
40 Qi, H. *et al.* Role of annexin A6 in cancer. *Oncology letters* **10**, 1947-1952 (2015).
41 Sakwe, A. M., Koumangoye, R., Guillory, B. & Ochieng, J. Annexin A6 contributes to the invasiveness of breast carcinoma cells by influencing the organization and localization of functional focal adhesions. *Exp Cell Res.* **317**, 823-837 (2011).
42 Leca, J. *et al.* Cancer-associated fibroblast-derived annexin A6+ extracellular vesicles support pancreatic cancer aggressiveness. *J Clin Invest.* **126**, 4140-4156 (2016).
43 Kidd, J. F. *et al.* Paclitaxel affects cytosolic calcium signals by opening the mitochondrial permeability transition pore. *J Biol Chem.* **277**, 6504-6510 (2002).
44 Octavia, Y. *et al.* Doxorubicin-induced cardiomyopathy: from molecular mechanisms to therapeutic strategies. *J Mol Cell Cardiol.* **52**, 1213-1225 (2012).
45 Steeg, P. S. Targeting metastasis. *Nat Rev Cancer* **16**, 201-218, doi:10.1038/nrc.2016.25 (2016).
46 Qian, B. Z. *et al.* CCL2 recruits inflammatory monocytes to facilitate breast-tumour metastasis. *Nature* **475**, 222-225, doi:10.1038/nature10138 (2011).
47 Bonapace, L. *et al.* Cessation of CCL2 inhibition accelerates breast cancer metastasis by promoting angiogenesis. *Nature* **515**, 130-133 (2014).
48 Doak, G. R., Schwertfeger, K. L. & Wood, D. K. Distant Relations: Macrophage Functions in the Metastatic Niche. *Trends Cancer* **4**, 445-459 (2018).
49 Kitamura, T. *et al.* CCL2-induced chemokine cascade promotes breast cancer metastasis by enhancing retention of metastasis-associated macrophages. *J Exp Med.* **212**, 1043-1059 (2015).
50 Hiratsuka, S. *et al.* Primary tumours modulate innate immune signalling to create pre-metastatic vascular hyperpermeability foci. *Nature Commun* **4**, 1853, doi:10.1038/ncomms2856 (2013).
51 Yanez-Mo, M. *et al.* Biological properties of extracellular vesicles and their physiological functions. *J Extracell Vesicles* **4**, 27066 (2015).
52 Campbell, K. A. *et al.* Annexin A6 interacts with p65 and stimulates NF-kappaB activity and catabolic events in articular chondrocytes. *Arthritis Rheum.* **65**, 3120-3129 (2013).
53 Ueda, A. *et al.* NF-kappa B and Sp1 regulate transcription of the human monocyte chemoattractant protein-1 gene. *J Immunol.* **153**, 2052-2063 (1994).
54 Srivastava, K. *et al.* Postsurgical adjuvant tumor therapy by combining anti-angiopoietin-2 and metronomic chemotherapy limits metastatic growth. *Cancer Cell* **26**, 880-895 (2014).
55 Incio, J. *et al.* Obesity promotes resistance to anti-VEGF therapy in breast cancer by up-regulating IL-6 and potentially FGF-2. *Sci Transl Med.* **10**, doi:10.1126/scitranslmed.aag0945 (2018).
56 Zhang, H. *et al.* Circulating Tumor Microparticles Promote Lung Metastasis by Reprogramming Inflammatory and Mechanical Niches via a Macrophage-Dependent Pathway. *Cancer Immunol Res.* **6**, 1046-1056 (2018).
57 Schwich, E. & Rebmann, V. The Inner and Outer Qualities of Extracellular Vesicles for Translational Purposes in Breast Cancer. *Front Immunol.* **9**, 584 (2018).

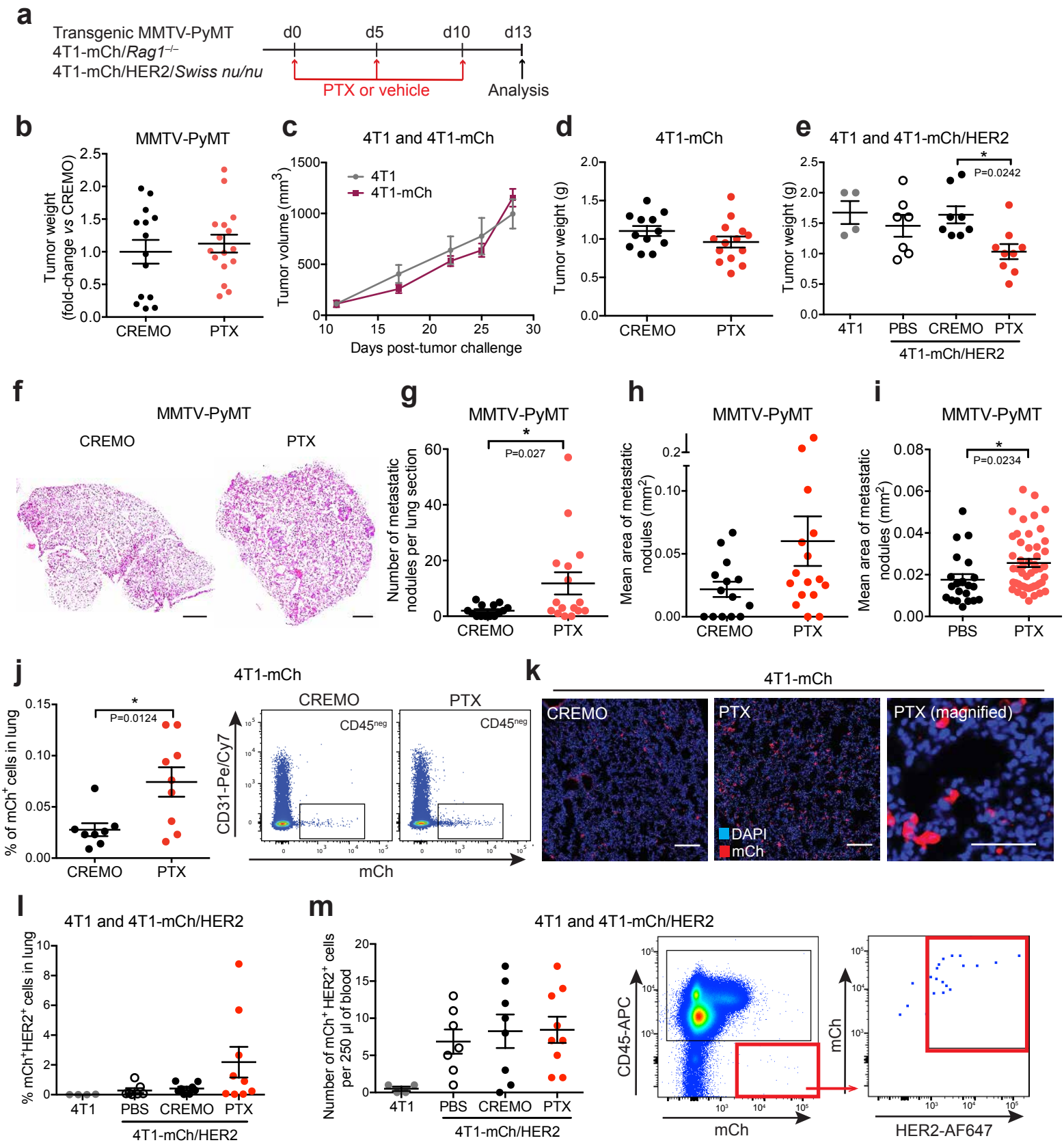
a
Transgenic MMTV-PyMT
4T1-mCh/Rag1−/−
4T1-mCh/HER2/Swiss nu/nu
d0
d5
d10
d13
PTX or vehicle
Analysis
b
MMTV-PyMT
Tumor weight (fold-change vs CREMO)
CREMO
PTX
c
4T1 and 4T1-mCh
Tumor volume (mm3)
4T1
4T1-mCh
Days post-tumor challenge
d
4T1-mCh
Tumor weight (g)
CREMO
PTX
e
4T1 and 4T1-mCh/HER2
Tumor weight (g)
P=0.0242
4T1
PBS
CREMO
PTX
4T1-mCh/HER2
f
MMTV-PyMT
CREMO
PTX
g
MMTV-PyMT
Number of metastatic nodules per lung section
P=0.027
CREMO
PTX
h
MMTV-PyMT
Mean area of metastatic nodules (mm2)
CREMO
PTX
i
MMTV-PyMT
Mean area of metastatic nodules (mm2)
P=0.0234
PBS
PTX
j
4T1-mCh
% of mCh+ cells in lung
P=0.0124
CREMO
PTX
CD45neg
CD31-Pe/Cy7
mCh
k
4T1-mCh
CREMO
PTX
PTX (magnified)
DAPI
mCh
l
4T1 and 4T1-mCh/HER2
% mCh+HER2+ cells in lung
4T1
PBS
CREMO
PTX
4T1-mCh/HER2
m
4T1 and 4T1-mCh/HER2
Number of mCh+ HER2+ cells per 250 µl of blood
4T1
PBS
CREMO
PTX
4T1-mCh/HER2
CD45-APC
mCh
HER2-AF647

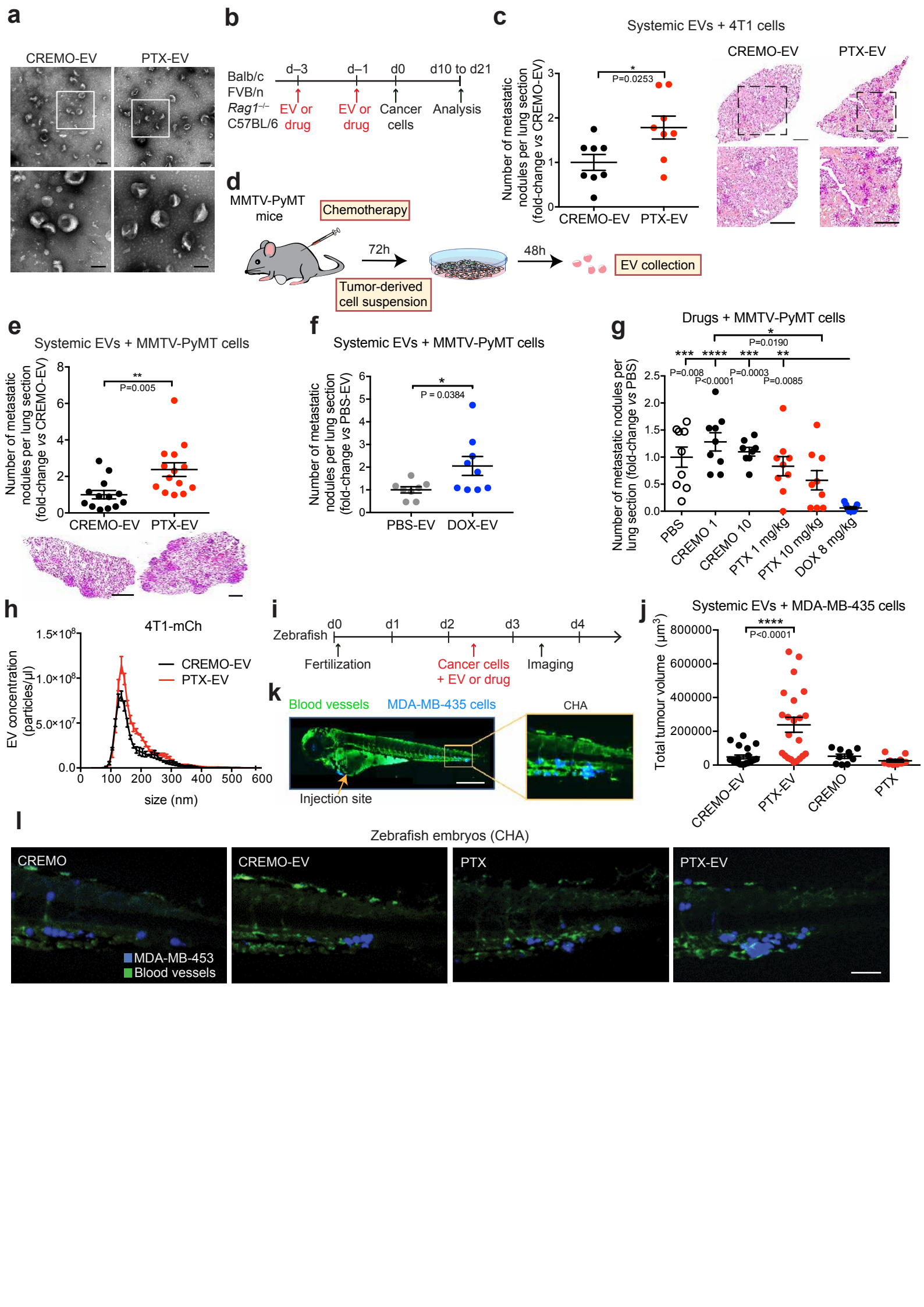
a
CREMO-EV
PTX-EV
b
Balb/c
FVB/n
Rag1−/−
C57BL/6
d–3
d–1
d0
d10 to d21
EV or drug
EV or drug
Cancer cells
Analysis
c
Systemic EVs + 4T1 cells
Number of metastatic nodules per lung section (fold-change vs CREMO-EV)
*
P=0.0253
CREMO-EV
PTX-EV
d
MMTV-PyMT mice
Chemotherapy
72h
48h
EV collection
Tumor-derived cell suspension
e
Systemic EVs + MMTV-PyMT cells
Number of metastatic nodules per lung section (fold-change vs CREMO-EV)
**
P=0.005
CREMO-EV
PTX-EV
f
Systemic EVs + MMTV-PyMT cells
Number of metastatic nodules per lung section (fold-change vs PBS-EV)
*
P = 0.0384
PBS-EV
DOX-EV
g
Drugs + MMTV-PyMT cells
Number of metastatic nodules per lung section (fold-change vs PBS)
*
P=0.0190
***
****
***
**
P=0.008
P<0.0001
P=0.0003
P=0.0085
PBS
CREMO 1
CREMO 10
PTX 1 mg/kg
PTX 10 mg/kg
DOX 8 mg/kg
h
4T1-mCh
EV concentration (particles/µl)
CREMO-EV
PTX-EV
size (nm)
i
Zebrafish
d0
d1
d2
d3
d4
Fertilization
Cancer cells + EV or drug
Imaging
k
Blood vessels
MDA-MB-435 cells
CHA
Injection site
j
Systemic EVs + MDA-MB-435 cells
Total tumour volume (µm3)
****
P<0.0001
CREMO-EV
PTX-EV
CREMO
PTX
l
Zebrafish embryos (CHA)
CREMO
CREMO-EV
PTX
PTX-EV
MDA-MB-453
Blood vessels

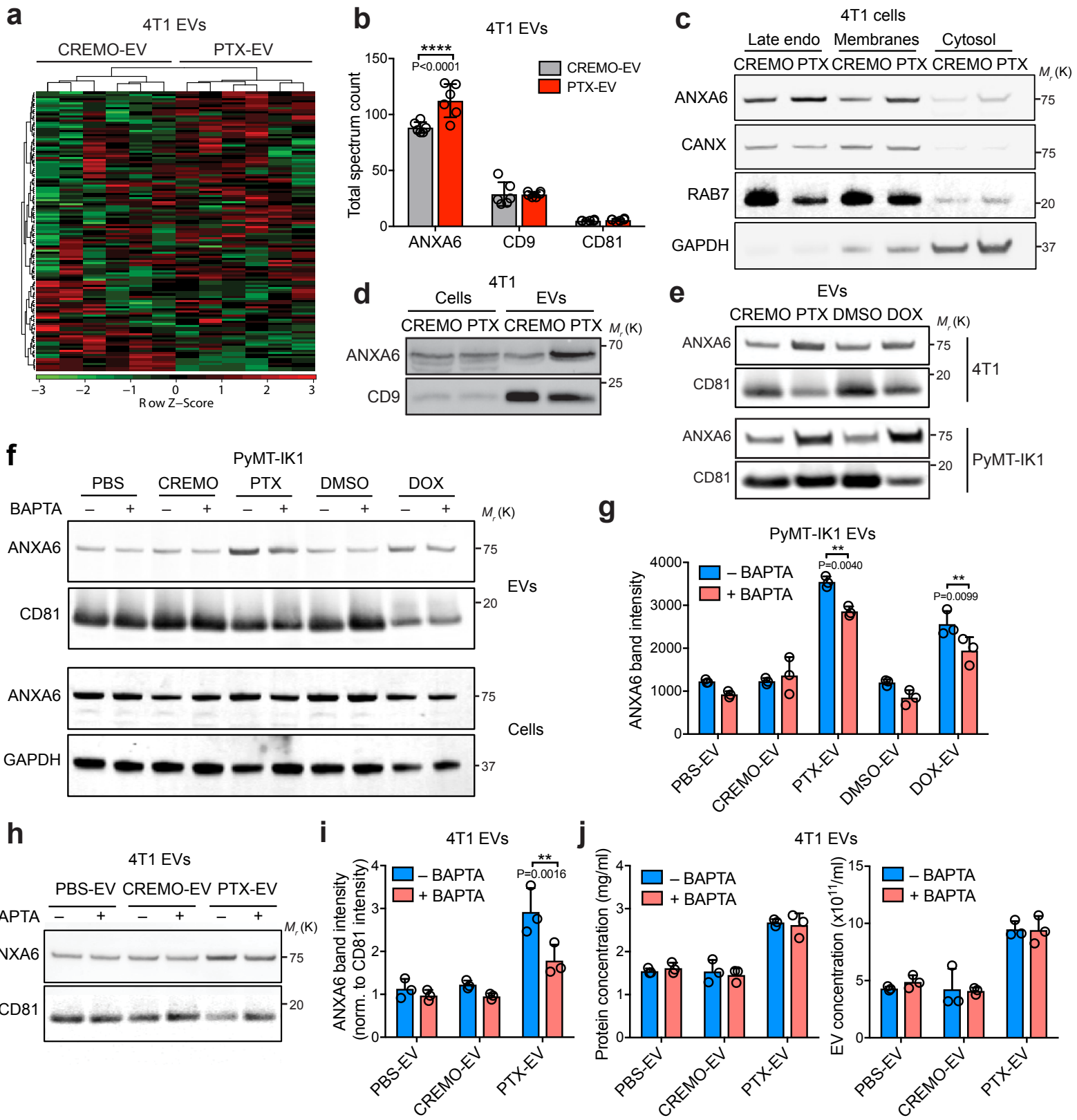
a
4T1 EVs
CREMO-EV
PTX-EV
−3 −2 −1 0 1 2 3
Row Z−Score
b
4T1 EVs
****
P<0.0001
CREMO-EV
PTX-EV
Total spectrum count
150
100
50
0
ANXA6
CD9
CD81
c
4T1 cells
Late endo
Membranes
Cytosol
CREMO PTX CREMO PTX CREMO PTX
Mr (K)
ANXA6
CANX
RAB7
GAPDH
75
75
20
37
d
4T1
Cells
EVs
CREMO PTX CREMO PTX
Mr (K)
ANXA6
CD9
70
25
e
EVs
CREMO PTX DMSO DOX
Mr (K)
ANXA6
CD81
75
20
4T1
ANXA6
CD81
75
20
PyMT-IK1
f
PyMT-IK1
PBS
CREMO
PTX
DMSO
DOX
BAPTA
Mr (K)
ANXA6
CD81
75
20
EVs
ANXA6
GAPDH
75
37
Cells
g
PyMT-IK1 EVs
– BAPTA
+ BAPTA
**
P=0.0040
**
P=0.0099
ANXA6 band intensity
4000
3000
2000
1000
0
PBS-EV
CREMO-EV
PTX-EV
DMSO-EV
DOX-EV
h
4T1 EVs
PBS-EV CREMO-EV PTX-EV
BAPTA
Mr (K)
ANXA6
CD81
75
20
i
4T1 EVs
– BAPTA
+ BAPTA
**
P=0.0016
ANXA6 band intensity (norm. to CD81 intensity)
4
3
2
1
0
PBS-EV
CREMO-EV
PTX-EV
j
4T1 EVs
– BAPTA
+ BAPTA
Protein concentration (mg/ml)
4
3
2
1
0
PBS-EV
CREMO-EV
PTX-EV
– BAPTA
+ BAPTA
EV concentration (x10^11/ml)
15
10
5
0
PBS-EV
CREMO-EV
PTX-EV

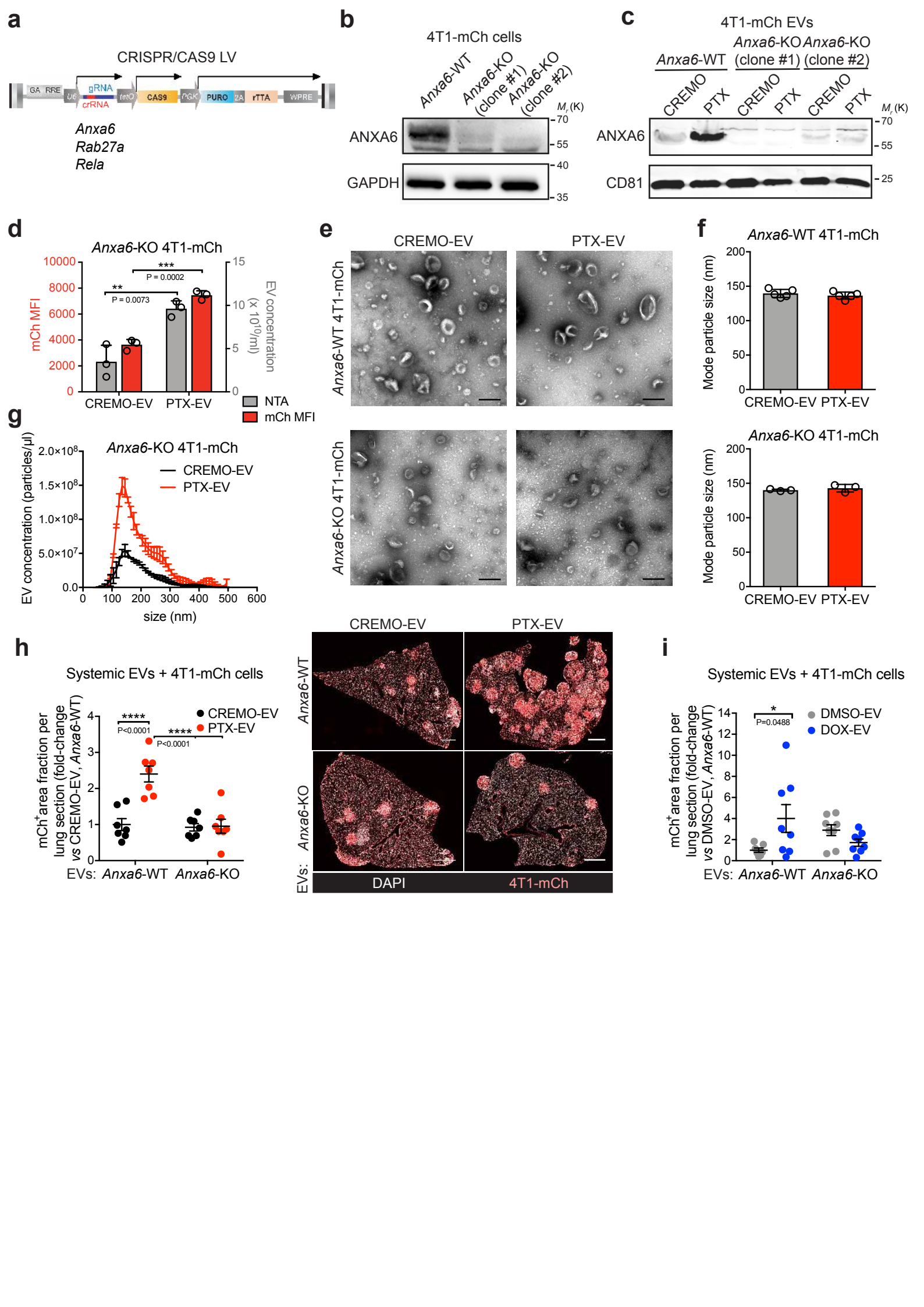
a
CRISPR/CAS9 LV
GA RRE
gRNA
U6
crRNA
tetO
CAS9
PGK
PURO
2A
rTTA
WPRE
Anxa6
Rab27a
Rela
b
4T1-mCh cells
Anxa6-WT
Anxa6-KO (clone #1)
Anxa6-KO (clone #2)
Mr (K)
ANXA6
GAPDH
70
55
40
35
c
4T1-mCh EVs
Anxa6-WT
Anxa6-KO (clone #1)
Anxa6-KO (clone #2)
CREMO
PTX
ANXA6
CD81
70
55
25
d
Anxa6-KO 4T1-mCh
mCh MFI
EV concentration (x 10^10/ml)
P = 0.0073
P = 0.0002
CREMO-EV
PTX-EV
NTA
mCh MFI
e
CREMO-EV
PTX-EV
Anxa6-WT 4T1-mCh
Anxa6-KO 4T1-mCh
f
Anxa6-WT 4T1-mCh
Anxa6-KO 4T1-mCh
Mode particle size (nm)
CREMO-EV PTX-EV
g
Anxa6-KO 4T1-mCh
EV concentration (particles/µl)
CREMO-EV
PTX-EV
size (nm)
h
Systemic EVs + 4T1-mCh cells
mCh+area fraction per lung section (fold-change vs CREMO-EV, Anxa6-WT)
P<0.0001
P<0.0001
CREMO-EV
PTX-EV
EVs: Anxa6-WT Anxa6-KO
CREMO-EV
PTX-EV
Anxa6-WT
Anxa6-KO
EVs:
DAPI
4T1-mCh
i
Systemic EVs + 4T1-mCh cells
mCh+area fraction per lung section (fold-change vs DMSO-EV, Anxa6-WT)
P=0.0488
DMSO-EV
DOX-EV
EVs: Anxa6-WT Anxa6-KO

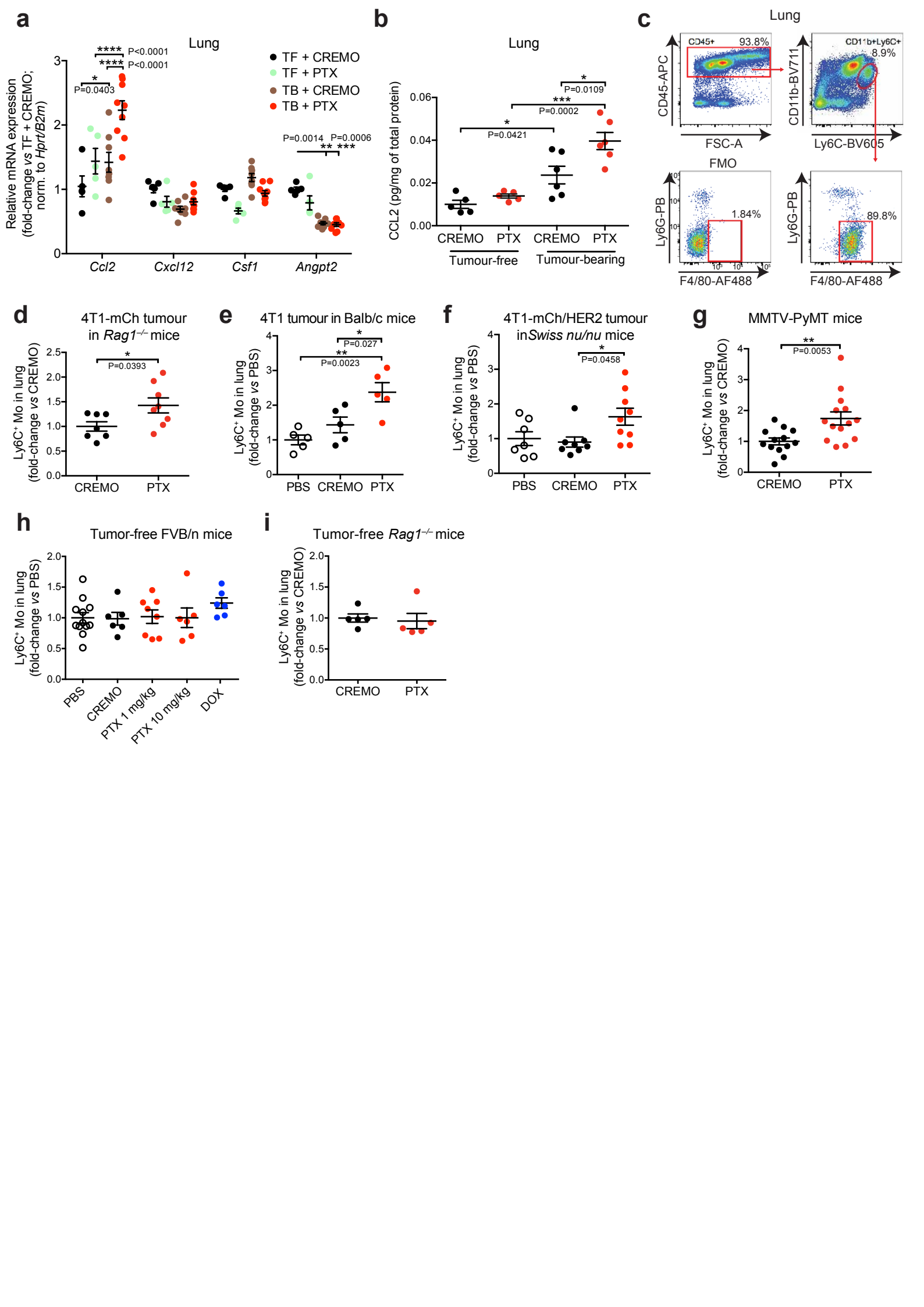
a
Lung
Relative mRNA expression (fold-change vs TF + CREMO; norm. to Hprt/B2m)
TF + CREMO
TF + PTX
TB + CREMO
TB + PTX
****
P<0.0001
****
P<0.0001
*
P=0.0403
P=0.0014
P=0.0006
**
***
Ccl2
Cxcl12
Csf1
Angpt2
b
Lung
CCL2 (pg/mg of total protein)
*
P=0.0109
***
P=0.0002
*
P=0.0421
CREMO
PTX
CREMO
PTX
Tumour-free
Tumour-bearing
c
Lung
CD45+
93.8%
CD45-APC
FSC-A
CD11b+Ly6C+
8.9%
CD11b-BV711
Ly6C-BV605
FMO
1.84%
89.8%
Ly6G-PB
F4/80-AF488
d
4T1-mCh tumour in Rag1−/− mice
Ly6C+ Mo in lung (fold-change vs CREMO)
*
P=0.0393
CREMO
PTX
e
4T1 tumour in Balb/c mice
Ly6C+ Mo in lung (fold-change vs PBS)
*
P=0.027
**
P=0.0023
PBS
CREMO
PTX
f
4T1-mCh/HER2 tumour in Swiss nu/nu mice
Ly6C+ Mo in lung (fold-change vs PBS)
*
P=0.0458
PBS
CREMO
PTX
g
MMTV-PyMT mice
Ly6C+ Mo in lung (fold-change vs CREMO)
**
P=0.0053
CREMO
PTX
h
Tumor-free FVB/n mice
Ly6C+ Mo in lung (fold-change vs PBS)
PBS
CREMO
PTX 1 mg/kg
PTX 10 mg/kg
DOX
i
Tumor-free Rag1−/− mice
Ly6C+ Mo in lung (fold-change vs CREMO)
CREMO
PTX

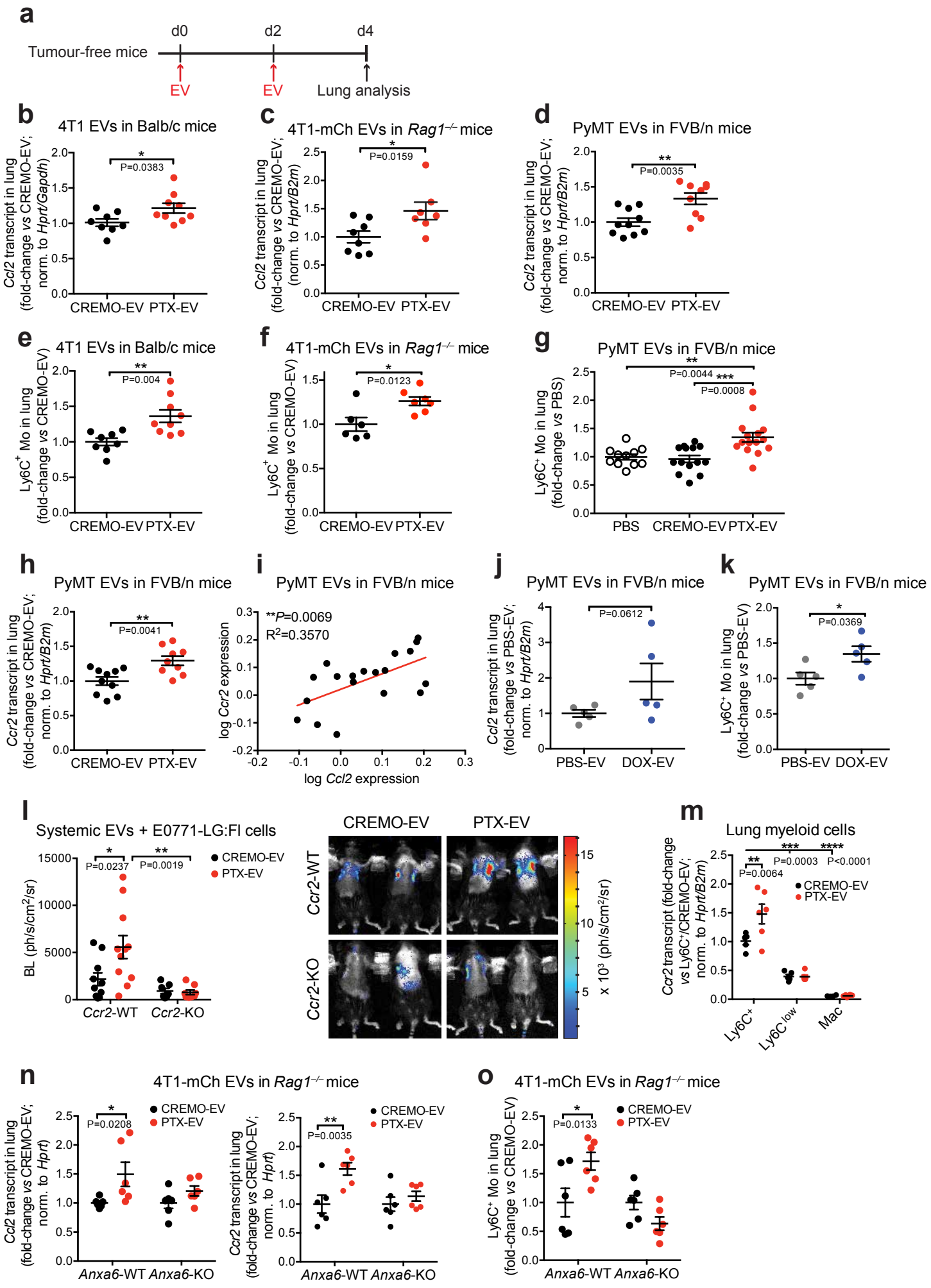
a
d0
d2
d4
Tumour-free mice
EV
EV
Lung analysis
b
4T1 EVs in Balb/c mice
Ccl2 transcript in lung (fold-change vs CREMO-EV; norm. to Hprt/Gapdh)
P=0.0383
CREMO-EV PTX-EV
c
4T1-mCh EVs in Rag1−/− mice
Ccl2 transcript in lung (fold-change vs CREMO-EV; (norm. to Hprt/B2m)
P=0.0159
CREMO-EV PTX-EV
d
PyMT EVs in FVB/n mice
Ccl2 transcript in lung (fold-change vs CREMO-EV; norm. to Hprt/B2m)
P=0.0035
CREMO-EV PTX-EV
e
4T1 EVs in Balb/c mice
Ly6C+ Mo in lung (fold-change vs CREMO-EV)
P=0.004
CREMO-EV PTX-EV
f
4T1-mCh EVs in Rag1−/− mice
Ly6C+ Mo in lung (fold-change vs CREMO-EV)
P=0.0123
CREMO-EV PTX-EV
g
PyMT EVs in FVB/n mice
Ly6C+ Mo in lung (fold-change vs PBS)
P=0.0044
P=0.0008
PBS CREMO-EV PTX-EV
h
PyMT EVs in FVB/n mice
Ccr2 transcript in lung (fold-change vs CREMO-EV; norm. to Hprt/B2m)
P=0.0041
CREMO-EV PTX-EV
i
PyMT EVs in FVB/n mice
**P=0.0069
R2=0.3570
log Ccr2 expression
log Ccl2 expression
j
PyMT EVs in FVB/n mice
Ccl2 transcript in lung (fold-change vs PBS-EV; norm. to Hprt/B2m)
P=0.0612
PBS-EV DOX-EV
k
PyMT EVs in FVB/n mice
Ly6C+ Mo in lung (fold-change vs PBS-EV)
P=0.0369
PBS-EV DOX-EV
l
Systemic EVs + E0771-LG:FI cells
BL (ph/s/cm2/sr)
P=0.0237
P=0.0019
CREMO-EV
PTX-EV
Ccr2-WT Ccr2-KO
CREMO-EV
PTX-EV
Ccr2-WT
Ccr2-KO
x 10³ (ph/s/cm²/sr)
m
Lung myeloid cells
Ccr2 transcript (fold-change vs Ly6C+/CREMO-EV; norm. to Hprt/B2m)
P=0.0064
P=0.0003
P<0.0001
CREMO-EV
PTX-EV
Ly6C+ Ly6Clow Mac
n
4T1-mCh EVs in Rag1−/− mice
Ccl2 transcript in lung (fold-change vs CREMO-EV; norm. to Hprt)
P=0.0208
CREMO-EV
PTX-EV
Anxa6-WT Anxa6-KO
Ccr2 transcript in lung (fold-change vs CREMO-EV; norm. to Hprt)
P=0.0035
CREMO-EV
PTX-EV
Anxa6-WT Anxa6-KO
o
4T1-mCh EVs in Rag1−/− mice
Ly6C+ Mo in lung (fold-change vs CREMO-EV)
P=0.0133
CREMO-EV
PTX-EV
Anxa6-WT Anxa6-KO

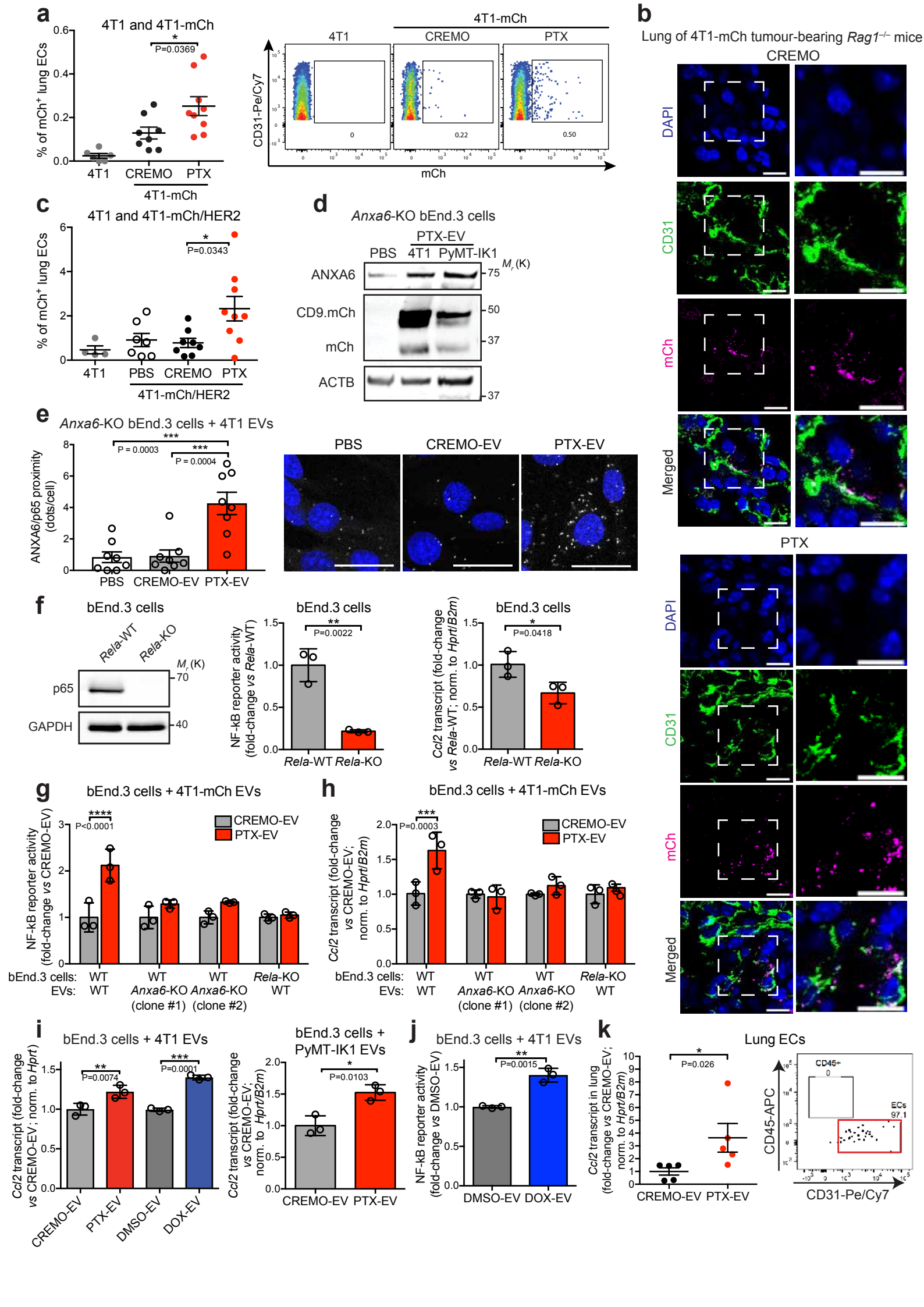
a
4T1 and 4T1-mCh
% of mCh+ lung ECs
P=0.0369
4T1
CREMO
PTX
4T1-mCh
4T1-mCh
CD31-Pe/Cy7
mCh
0
0.22
0.50
b
Lung of 4T1-mCh tumour-bearing Rag1−/− mice
CREMO
PTX
DAPI
CD31
mCh
Merged
c
4T1 and 4T1-mCh/HER2
P=0.0343
PBS
4T1-mCh/HER2
d
Anxa6-KO bEnd.3 cells
PTX-EV
PBS
4T1
PyMT-IK1
ANXA6
CD9.mCh
mCh
ACTB
e
Anxa6-KO bEnd.3 cells + 4T1 EVs
ANXA6/p65 proximity (dots/cell)
P = 0.0003
P = 0.0004
PBS
CREMO-EV
PTX-EV
f
bEnd.3 cells
Rela-WT
Rela-KO
p65
GAPDH
NF-kB reporter activity (fold-change vs Rela-WT)
P=0.0022
Ccl2 transcript (fold-change vs Rela-WT; norm. to Hprt/B2m)
P=0.0418
g
bEnd.3 cells + 4T1-mCh EVs
NF-kB reporter activity (fold-change vs CREMO-EV)
P<0.0001
CREMO-EV
PTX-EV
bEnd.3 cells:
EVs:
WT
Anxa6-KO (clone #1)
Anxa6-KO (clone #2)
Rela-KO
h
bEnd.3 cells + 4T1-mCh EVs
Ccl2 transcript (fold-change vs CREMO-EV; norm. to Hprt/B2m)
P=0.0003
i
bEnd.3 cells + 4T1 EVs
Ccl2 transcript (fold-change vs CREMO-EV; norm. to Hprt)
P=0.0074
P=0.0001
CREMO-EV
PTX-EV
DMSO-EV
DOX-EV
bEnd.3 cells + PyMT-IK1 EVs
Ccl2 transcript (fold-change vs CREMO-EV; norm. to Hprt/B2m)
P=0.0103
j
bEnd.3 cells + 4T1 EVs
NF-kB reporter activity (fold-change vs DMSO-EV)
P=0.0015
DMSO-EV
DOX-EV
k
Lung ECs
Ccl2 transcript in lung (fold-change vs CREMO-EV; norm. to Hprt/B2m)
P=0.026
CD45-APC
CD31-Pe/Cy7
ECs
97.1

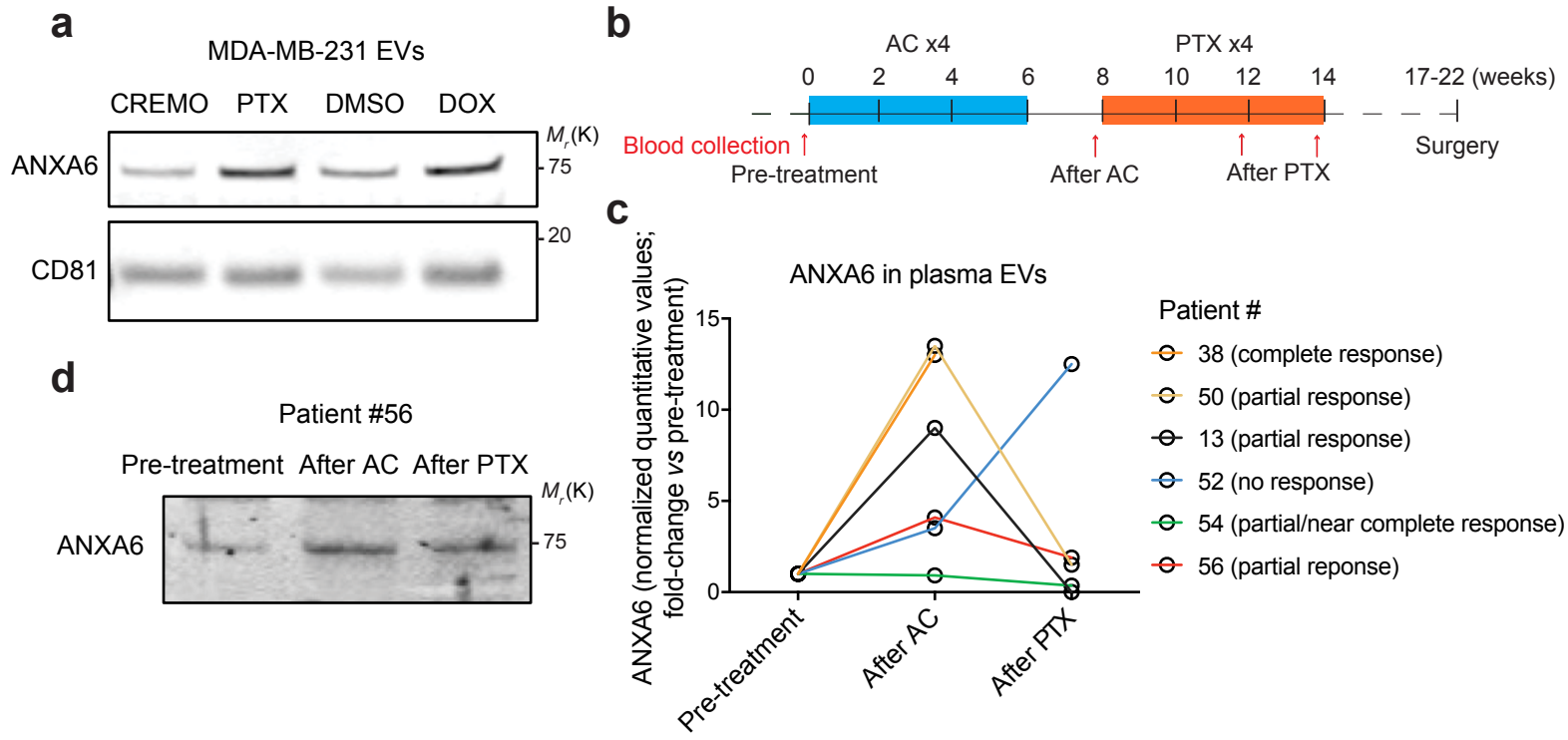
a
MDA-MB-231 EVs
CREMO
PTX
DMSO
DOX
ANXA6
CD81
M_r(K)
75
20
b
AC x4
PTX x4
0
2
4
6
8
10
12
14
17-22 (weeks)
Blood collection
Pre-treatment
After AC
After PTX
Surgery
c
ANXA6 in plasma EVs
ANXA6 (normalized quantitative values; fold-change vs pre-treatment)
15
10
5
0
Pre-treatment
After AC
After PTX
Patient #
38 (complete response)
50 (partial response)
13 (partial response)
52 (no response)
54 (partial/near complete response)
56 (partial reponse)
d
Patient #56
Pre-treatment
After AC
After PTX
ANXA6
M_r(K)
75

Online Methods

Mice

FVB/n, Balb/c, C57BL/6 and *Swiss nu/nu* mice were purchased from Charles River Laboratories. *Ccr2*-KO mice (C57BL/6 background) were obtained from The Jackson Laboratory (https://www.jax.org) and bred under standard conditions at the University of Edinburgh (United Kingdom). *Rag1*$^{-/-}$ mice (C57BL/6 background) were available in the EPFL mouse facility (Switzerland). Transgenic MMTV-PyMT mice (FVB/n background) were available in both EPFL mouse facility and Department of Comparative Medicine barrier facility (Oregon). Male mice heterozygous for the Polyoma virus middle TAg (PyMT) were bred with wild-type females; pups were genotyped by Transnetyx (http://www.transnetyx.com). All mice employed in this study were maintained in pathogen-free barrier animal facilities in accord with State regulations for the care and use of mice in experimental research.

The studies involving mice were compliant with all relevant ethical regulations regarding animal research. Most of the experiments were performed at EPFL; some experiments were performed at the University of Edinburgh (*Ccr2*-KO mice) and at Oregon Health & Science University (OHSU), Portland (MMTV-PyMT mice, *partim*). All procedures were performed according to protocols approved by the Veterinary Authorities of the Canton Vaud according to the Swiss Law (licenses 2577, 2577.1 and 2916); the UK Animal Scientific Procedures Act (1986) license (PPL 70/8065); and the Public Health Service of USA (PHS), the Office for the Protection from Research Risks (OPRR) A-3304-01, the United States Department of Agriculture (USDA) 92-R-001, and the Association for Assessment and Accreditation of Laboratory Animal Care (AAALAC) International. OHSU maintains AAALAC International accreditation and OLAW assurance (A3304-01), and all procedures with small animals at OHSU were IACUC approved (IS00001484).

Cell lines

The mouse cell lines 4T1 (mammary adenocarcinoma; from ATCC), bEnd.3 (brain endothelial cells; provided by F. Bussolino, University of Turin, Italy), 293T (provided by L. Naldini, San Raffaele Scientific Institute, Milan, Italy), and PyMT-IK1 (mammary adenocarcinoma; isolated in the De Palma's lab) were maintained in Iscove's modified Dulbecco's medium (IMDM, Sigma) supplemented with 10% fetal bovine serum (FBS; Gibco), L-glutamine (Amimed) and penicillin/streptomycin (Gibco). The PyMT-IK1 cell line was isolated from a primary mammary tumour of a 14-week old, transgenic MMTV-PyMT female mouse. Mouse E0771-LG cells (mammary adenocarcinoma; derived from the parental cell line E0771), either unmodified or stably transfected with a firefly luciferase cDNA for *in vivo* bioluminescence imaging (E0771-LG:Fl; both provided by T. Kitamura, University of Edinburgh, United Kingdom) [49,58], were maintained in Dulbecco's medium (DMEM, Gibco) with 10% FBS, L-glutamine and penicillin/streptomycin. The human cell line MDA-MB-231 (breast adenocarcinoma; from ATCC) was cultured in RPMI 1640 (Gibco) with 10% FBS and penicillin/streptomycin. The human melanoma cell line MDA-MB-435 stably transfected to express cyan fluorescent protein (CFP; provided by R. Klemke, University of Sheffield, United Kingdom) was maintained in DMEM with 10% fetal calf serum (FCS; BioWhittaker, United Kingdom) and 50 µg/ml G418 (Sigma) to maintain CFP expression. All cell lines used tested negative for *Mycoplasma* contamination.

Primary cell cultures

Bone marrow dendritic cells (BMDCs) were obtained by flushing long bones of 6-week old C57BL/6 mice, as described previously [29], and cultured for 6 days in RPMI 1640 medium with 10% FBS, L-glutamine, penicillin/streptomycin, and GM-CSF (100 ng/ml, Peprotech).

Mouse embryonic fibroblasts (MEFs) were obtained from C57BL/6 mice on day E14.5, as described previously [59], and cultured in DMEM with 10% FBS, L-glutamine, penicillin/streptomycin. We verified the purity of MEFs ($CD45^-CD31^-EpCAM^-CD140a^+$) by fluorescence-activated cell sorting (FACS).

In order to obtain MMTV-PyMT tumour-derived cells, primary mammary tumours of 14-week old female MMTV-PyMT mice were dissected, minced and digested with collagenase IV (0.2 mg/ml, Worthington), dispase (2 mg/ml, Life Technologies) and DNaseI (0.002 mg/ml, Life Technologies) in IMDM medium for 30 min at 37°C. The cell suspensions were filtered using a cell strainer (70 µm) before plating. Tumour-derived cells were then cultured for 48h in IMDM supplemented with 5% EV-depleted FBS, L-glutamine, and penicillin/streptomycin before intraveneous injection in tumour-free mice.

Treatment of primary cells with chemotherapeutic drugs was conducted in complete medium supplemented with EV-depleted, 5% FBS for 3 days. At the end of the treatment, the viability of BMDCs and MEFs was assessed by Trypan Blue staining and WST-1 assay, respectively.

Generation, production and use of lentiviral vectors (LVs)

Lentiviral vectors (LVs) expressing a CD9.mCherry fusion protein or human HER2 were described previously [29,60]. In order to disrupt *Rab27a*, *Rela* or *Anxa6* in bEnd.3 or 4T1 cells, we generated self-inducible CRISPR-Cas9-based LVs, as described previously [29]. Briefly, we annealed and ligated the DNA sequences shown below using the BsmBI restriction site in the U6-(sgRNA).TetO-CAS9.hPGK-PURO/2A/rtTA LV (Ref 29):

Rab27a sense: ACCGTATCCAGTTTCGGACATTG

Rab27a antisense: AAACCAATGTCCGAAACTGGATA

Rela sense: ACCGGGCTGGGGTCGGCGTACGG

Rela antisense: AAACCCGTACGCCGACCCCAGCC

Anxa6 sense: ACCGGATTCCAGGTCTCGCTCAT

Anxa6 antisense: AAACATGAGCGAGACCTGGAATC.

To generate the NF-kB reporter LV, we isolated the minimal mouse *Fos* promoter element and three copies of the major histocompatibility complex (MHC) class I KB element (TGGGGATTCCCCA) by digesting a plasmid obtained from Addgene (https://www.addgene.org/26699/) with HincII and PvuII restriction enzymes. The sequence was then inserted downstream to the minimal CMV promoter (mCMV) of a bidirectional hPGK.GFP/mCMV.mCh LV, after digestion with EcoRV.

Vesicular stomatitis virus (VSV)-pseudotyped, third-generation LVs were produced by transient four-plasmid co-transfection into 293T cells and concentrated by ultracentrifugation, as described previously [61]. Expression titres of LVs encoding fluorescent proteins were determined in 293T cells by limiting dilution. LV stocks were stored at –80°C.

PyMT-IK1 and 4T1 cells were transduced with LVs expressing CD9.mCh; 4T1-mCh cells were further

transduced with a HER2-expressing LV for use in some experiments. Cells expressing HER2 and/or mCh were sorted by FACS (Aria II apparatus, BD Biosciences) to establish pure cell populations expressing the transgene(s) of interest.

bEnd.3 and 4T1-mCh cells were transduced with CRISPR-Cas9 LVs to disrupt *Rab27a*, *Rela* or *Anxa6*. After transduction, the cells were cultured in complete IMDM medium with puromycin (5-10 µg/ml, Sigma) and doxycycline (10 µg/ml, Sigma) for 4 days to select transduced cells. The cells were then plated in normal medium to isolate cell clones. Cell colonies showing no expression of RAB27A, RELA or ANXA6 by Western blotting were expanded and employed in further experiments.

Cytotoxic drugs

Paclitaxel (PTX) dissolved in cremophor EL (Labatec) was obtained at stock concentration of 6 mg/ml. PTX was used at 100 ng/ml (cell culture experiments), 10 mg/kg (mouse models) or 100 nM (zebrafish models), unless indicated otherwise. Cremophor EL (CREMO; Sigma) was used as control vehicle for PTX, both *in vitro* and *in vivo*. Oregon Green-488-conjugated PTX (Thermo Fisher Scientific) was reconstituted in DMSO and used at a concentration of 100 ng/ml. Doxorubicin and docetaxel (Sigma) were reconstituted in DMSO, while gemcitabine (Sigma) was reconstituted in water. Unless indicated otherwise, doxorubicin, docetaxel and gemcitabine were used in cell culture experiments at 200, 100 and 10 ng/ml, respectively. For mouse studies, doxorubicin (DOX; adriblastine; Pfizer) was dissolved in PBS and used at 8 mg/kg.

Cytotoxic drugs (or control vehicle) were added once to the cell culture medium and the experiments terminated after 24 to 72h. Mice received three doses of either PTX or DOX, as described below.

Treatment of transgenic MMTV-PyMT mice

Female transgenic mice were treated with 10 mg/kg PTX or CREMO in PBS intraperitoneally (EPFL cohort) or intraveneously (OHSU cohort), or 8 mg/kg DOX or PBS intraperitoneally. All mice received 3 drug/vehicle doses at 5-day (PTX) or 7-day (DOX) intervals, starting at 11-12 weeks of age, when multifocal mammary tumours are evident in this model [46]. The mice were euthanized 3 days after the last dose. Tumour weight measurements were performed at necropsy by dissecting the ten mammary glands.

Treatment of mice carrying subcutaneous tumours

Subcutaneous 4T1 tumours were established by implanting 10^6 4T1, 4T1-mCh or 4T1-mCh/HER2 cells in the right flank of 6 to 8-week old Balb/c, *Rag1*$^{-/-}$ or *Swiss nu/nu* mice. Both female and male *Rag1*$^{-/-}$ mice were employed; only female Balb/c and *Swiss nu/nu* mice were employed. Treatments were initiated when the tumour volume reached 100-200 mm^3; the mice were euthanized 3 days after the last drug dose. Tumour growth was monitored biweekly and the tumour size determined by caliper measurements. The tumour volume was calculated using the formula: tumour volume [mm^3] = (length [mm]) × (width [mm]) × (height [mm]) × 0.5236. Tumour weight measurements were performed at necropsy.

Isolation of EVs from media conditioned by continuous and primary cell cultures

In order to isolate EVs, cells were cultured and expanded in the appropriate medium. Cells at about 40-50% confluence were then moved to medium containing 5% EV-depleted FBS obtained by ultracentrifugation of

standard FBS at 134000 x g for 16h at 4°C, followed by filtering through a 0.1 µm vacuum filtration bottle. EVs were isolated from the conditioned medium using sequential ultracentrifugation, as described [29,30]. Briefly, conditioned medium was centrifuged at 500 x g for 5 min; 2000 x g for 10 min; and 4600 x g for 20 min, at 4°C to remove dead cells and debris. The medium was then ultracentrifuged at 134000 x g for 70 min at 4°C using a Beckman ultracentrifuge and SW32Ti rotor. The pellet was washed in 35 ml of PBS and ultracentrifuged again at 134000 x g for 70 min at 4°C. The resulting EV preparation was dissolved in PBS or RIPA buffer (Sigma), depending on the application, and either used immediately or stored at −80°C. The average EV yield obtained from 4T1, PyMT-IK1, MDA-MD-231, E0771-LG, BMDCs and MEFs was, respectively, 7.3, 0.8, 0.8, 1.8, 0.1 and 1 µg of EVs (determined by BCA) per ml of cell culture medium.

Isolation of MMTV-PyMT tumour-derived EVs

After treatment of the mice with cytotoxic drugs, primary MMTV-PyMT tumours were made into single cell suspensions as described above. The tumour-derived cells were cultured for 48h in IMDM supplemented with 5% EV-depleted FBS, L-glutamine and penicillin/streptomycin before EV isolation by ultracentrifugation. The average yield of purified EVs was 50 µg per gram of tumour.

Isolation of EVs from mouse or human plasma

We obtained blood of 4T1-mCh tumour-bearing mice treated with PTX or CREMO by cardiac puncture after deep sedation (150 mg/kg pentobarbital, intraperitoneally). To obtain plasma for EV isolation or mCh quantification, blood was centrifuged at 500 x g for 5 min; 2000 x g for 15 min; and 10000 x g for 20 min at 4°C to remove cells, debris and large vesicles. Human plasma was obtained as described below.

To isolate EVs, plasma was ultracentrifuged at 134000 x g for 70 min at 4°C using a Beckman ultracentrifuge and SW55Ti rotor. The pellet was washed in 4.5 ml of PBS and ultracentrifuged again at 134000 x g for 70 min at 4°C. The resulting EV preparation was dissolved in PBS and either used immediately or stored at −80°C.

Quantification of EVs

EV preparations were analysed for protein content using the BCA Protein Assay Reagent Kit (Thermo Fisher Scientific).

The size and concentration of EVs were determined by Nanoparticle Tracking Analysis (NTA) using a Nanosight NS300 device (Malvern Instruments, United Kingdom). We tested different sample dilutions (1:50 to 1:2000, in PBS) whereby particle concentration was within the optimal range of detection (5×10^7 - 1×10^9 particles/ml). All camera settings were set at the beginning of the session and kept fixed during all acquisitions in a given experiment: camera level, 7-9; camera gain, 10-12; detection threshold, 2-4. For each sample, at least three videos of 60 sec for at least one EV dilution were taken and analysed using the NTA software 3.0 with default settings.

Transmission electron microscopy (TEM) of purified EVs

Purified EVs (5 µg in 15 µl of PBS) were applied to carbon-coated 400 mesh grids (Electron Microscopy Sciences) for 5 min, then washed with PBS and stained with 2% uranyl acetate for 30 sec, as described

previously [62]. Images were obtained using a transmission electron microscope device (Tecnai Spirit, FEI Company).

Sucrose gradient fractionation of EVs

Purified EVs were subjected to continuous sucrose gradient fractionation using established procedures [31,63]. Briefly, twelve stock solutions with decreasing sucrose concentration were layered on top of purified EVs (800 µg, in 100 µl PBS) in a total volume of 12 ml, followed by ultracentrifugation at 100000 x g for 16h at 4°C with a Beckman ultracentrifuge and a SW40Ti rotor. Six fractions of 2 ml each were then collected and transferred to new tubes; the density of each sucrose fraction was measured using a refractometer. Each fraction was washed with 10 ml of PBS and ultracentrifuged at 110000 x g for 70 min at 4°C as above. EVs were resuspended in 100 µl of PBS prior to subsequent analyses.

Quantification of EV-associated mCh fluorescence in cell culture media and mouse plasma

mCh fluorescence was measured in 100 µl of PBS containing purified EVs, or 100 µl of mouse plasma, using a spectrophotometer (TECAN infinite2000 plate-reader, TECAN). The following parameters were used: excitation wavelength, 586 nm; emission wavelength, 625 nm; number of reads, 4.

To degrade free (non-EV-associated) mCh protein, a proteinase K reaction was performed using 40% of plasma and 0.25 mg/ml proteinase K (Promega) in 1 mM guanidinium hydroxide (GuOH)/30mM Tris/5mM $CaCl_2$, for 2h at 55^{o}C.

Determination of PTX and DOX concentration in EVs

The content of PTX and DOX in purified EVs was assessed by measuring the fluorescence intensity of Oregon Green-488-conjugated PTX (Thermo Fisher Scientific) and the spontaneous fluorescence of DOX (Sigma), respectively, using a spectrophotometer (TECAN infinite2000 plate-reader). We measured several dilutions of the EVs in PBS, as well as equal amounts of drug-free EVs from DMSO-treated cells for background subtraction. The following parameters were utilized for measuring fluorescence of Oregon Green-488-conjugated PTX and DOX, respectively: excitation wavelengths, 495 and 470 nm; emission wavelengths, 525 and 585 nm; number of reads: 4 per EV dilution. Standard curves of Oregon Green-488-PTX and DOX were employed to extrapolate drug concentration in EVs from fluorescence intensity values.

EV pre-conditioning of mice

Cell- or tumour-derived EVs (15 µg in 100 µl of PBS) were centrifugated at 4600 x g for 1 min at 4^{o}C to remove sedimentable aggregates before intravenous injection into 6 to 8-week old, tumour-free mice (FVB/N, C57BL/6/*Rag1*$^{-/-}$, Balb/c, C57BL/6/*Ccr2*-KO or C57BL/6). Two EV doses were administered two days apart. For gene expression and FACS analyses, tumour-free mice were euthanized 2 days after the last EV dose. For experimental metastasis (lung colonization) studies, cancer cells were infused intravenously one day after the last EV administration and euthanized at the time points described below.

Lung colonization studies

4T1-mCh cells (5 x 10^{5}) were injected intravenously in 6-8 week-old, male or female *Rag1*$^{-/-}$ mice one day

after EV pre-conditioning. The mice were euthanized 3 weeks after cancer cell injection and lungs fixed, sectioned, and analysed for direct mCh fluorescence to quantify metastatic tumour burden.

4T1 cells (1 x 10^5) were injected intravenously in 6 week-old female Balb/c mice one day after EV pre-conditioning. The mice were euthanized 10 days after cancer cell injection and lungs fixed, sectioned, and stained with hematoxylin/eosin (H&E) to quantify metastatic tumour burden.

MMTV-PyMT tumour-derived cells (5 x 10^5) were injected intravenously into 6-7 week-old female FVB/n mice one day after EV pre-conditioning. The mice were euthanized three weeks after tumour cell injection and lungs fixed, sectioned, and stained with H&E to quantify metastatic tumour burden.

E0771-LG:FI cells (1x10^6) were intravenously injected into 6-8 week-old, male or female C57BL/6 or C57BL/6/*Ccr2*-KO mice one day after EV pre-conditioning. Bioluminescence was determined 10 days after cancer cell injection.

***In vivo* bioluminescence imaging**

C57BL/6 or *Ccr2*-KO mice were anesthetised with isofluorane (3-4 % induction, 1-2% maintenance) and administered 150 µg of luciferin (GoldBio) intraperitoneally per gram of body weight. Mice were imaged under Photon Imager Optima (Biospace Lab) for 15 min until the bioluminescence signal reached a plateau. Imaging was done 30 min and 10 days after E0771-LG:FI cell injection. Photon counts (photon/second/cm2/sr) in the lung area were analysed using the M3 Vision software (Biospace Lab).

Analysis of pulmonary metastasis in mice

To analyse lungs for the presence of mCh-negative tumour nodules, formalin or paraformaldehyde-fixed lungs were sectioned into 5- or 8 µm-thick sections, respectively, at 100 µm intervals. Three to four large lung sections were stained with H&E. Sections were scanned with an Olympus slide scanner (VS120-L100) endowed with a 10x objective and fully automated scanning capabilities. Tumour nodules (>10-20 cancer cells) were counted and their area measured using the OlyVIA (Olympus) and ImageJ softwares, respectively. The number and mean area of the metastatic nodules were calculated by averaging data from individual sections.

To analyse lungs for the presence of mCh^+ tumour nodules or disseminated cancer cells, paraformaldehyde-fixed lungs were sectioned into 8 µm-thick sections at 100 µm intervals. Four large sections were counterstained with DAPI and scanned with an Olympus slide scanner (VS120-L100) to acquire both mCh and DAPI fluorescence. Images were analysed using the ImageJ software and the VSI Biop tool. The total metastatic area was calculated by normalizing the mCh^+ area to the total lung ($DAPI^+$) area and by averaging data from individual sections. In some experiments, mCh^+ cancer cells were also quantified by FACS analysis of homogenised lung tissue.

Zebrafish studies

The studies involving zebrafish (*Danio rerio*) were compliant with all relevant ethical regulations regarding animal research. Zebrafish were maintained according to standard protocols. All tumour studies were authorised by the UK Home Office under licence 40/3690 and performed at the zebrafish facility of the University of Sheffield, United Kingdom. The transgenic zebrafish line *fms*:UNM [64] was crossed with the

Tg(tie2:GFP) line [65] to obtain the double transgenic *fms*:UNM; Tg(tie2:GFP) line, which enables the direct visualization of blood and lymphatic vessels.

Zebrafish embryos were maintained in E3 medium at 28°C. Before injection of EVs (or free drug) and cancer cells, 56h post-fertilization embryos were anesthetized by immersion in 0.04 mg/ml of tricaine (MS222; Sigma) and immobilized in 1% low melting point agarose (Sigma). Each embryo received 200-300 CFP^+ MDA-MB-435 cells together with purified EVs (0.326 µg/ml) or drugs (PTX or CREMO; 100 µM) in 4 nl of saline, via the duct of Cuvier with a microinjector (World Precision Instruments, United Kingdom).

The embryos were analysed 18 h post-injection. After anaesthesia/immobilization, we used a spinning disc confocal microscope (Olympus IX81, PerkinElmer, UK) to image the tail of the zebrafish and capture Z-stacks at 3 µm increments. The full tail of the embryo was covered by two images at 10x magnification. Image acquisition and processing were performed with Volocity 6.3 software (Improvision, Coventry, United Kingdom). Cancer cell aggregates were visualized by capturing the CFP fluorescence of the cells, and the total metastatic volume was calculated from the XYZ analysis of CFP fluorescence in each of the tumour Z-stacks.

Preparation of tumours, lungs and livers for FACS analysis and cell sorting

Before sacrifice, deeply anaesthetised mice were perfused with PBS to remove intravascular blood cells. Tumours, lungs and livers were then harvested, washed extensively in PBS, and then minced before digestion with collagenase IV (0.2 mg/ml), dispase (2 mg/ml) and DNase I (0.002 mg/ml) in IMDM medium for 20 min at 37°C. The cell suspensions were filtered using a cell strainer (70 µm) and washed in PBS containing 2 mM EDTA and 2% FBS. Red blood cells were lysed using a Red blood cell Lysis buffer (Sigma).

Cell suspensions were incubated with rat anti-mouse FcγIII/II receptor (CD16/CD32) blocking antibodies (4 µg/ml) for 15 min at 4°C prior to extracellular staining with conjugated antibodies (**Supplementary Table 4**) for 20 min at 4°C. Before analysis, cells were resuspended in DAPI-containing buffer to identify non-viable cells. All samples were analysed using an LSRII apparatus (BD Biosciences). Compensation was performed using fluorescence-minus-one (FMO) controls.

To sort cells, we used a FACS Aria II apparatus (BD Biosciences). Each cell population was isolated from a single organ/mouse. Typically, $2x10^3$ to $2x10^5$ cells were obtained from each sorting session and all populations were verified by performing post-sorting analysis. Cell types were identified using the following combinations of cell markers:

Endothelial cells (ECs): $CD45^-CD31^+$

Ly6C$^+$ classical monocytes: $CD45^+CD11b^+Ly6C^+Ly6G^-F4/80^+$

Ly6C^{low} monocytes: $CD45^+CD11b^+Ly6C^{low}Ly6G^-F4/80^-$

Monocytes/macrophages: $CD45^+CD11b^+Gr1^-$ or $CD45^+CD11b^+Ly6G^-Ly6C^{low}$

Alveolar lung macrophages: $CD45^+CD11c^+SiglecF^+F4/80^+$

Non-alveolar lung macrophages: $CD45^+CD11c^-SiglecF^-CD11b^+Ly6G^-Ly6C^{low}F4/80^+$

Neutrophils: $CD45^+CD11b^+Ly6G^+$

Disseminated cancer cells: $CD45^-CD31^-mCh^+$

Quantification of circulating cancer cells by FACS

Blood was collected by cardiac puncture of deeply anesthetised mice and collected in EDTA-containing tubes. To enumerate circulating cancer cells, we used 250 µl of erythrocyte-depleted blood. The cell suspension was processed as described above, and circulating cancer cells identified as $CD45^{-}mCh^{+}HER2^{+}$ cells using an LSRII apparatus.

Immunofluorescence staining of tumour and organ sections

Tumours and organs were fixed in 4% paraformaldehyde for 24h at 4°C, equilibrated in sucrose solutions for 24h, and then embedded in O.C.T compound (Cryomatrix, Thermo Fisher Scientific) on dry ice with iso-pentane (VWR Chemicals) before storage at -80°C. Tissue sections of 8 µm were obtained using a Leica cryostat CM1950 (Leica Biosystems). Before staining, the sections were rehydrated and then incubated with blocking solution (1% BSA, 10% FBS, 0.3% Triton X-100, and rat anti-mouse FcγII/III receptor 1:100, in PBS) for 1h at room temperature. The sections were incubated overnight at 4°C in 100-200 µl of blocking solution containing the primary antibodies listed in **Supplementary Table 4**. Non-conjugated antibodies were revealed with secondary antibodies. After staining, nuclei were labeled with DAPI (1 µg/ml) and sections mounted in Dako Fluorescence Mounting Medium, covered with cover glass (Heathrow Scientific), and stored at 4°C.

Immunofluorescence staining of cultured cells

Cells were seeded on glass chamber slides (Lab-Tek) or glass coverslips (Electron Microscopy Sciences) coated with 50 µg/ml poly-L-lysine (Sigma). After 16-24h, the cells were treated with drugs or EVs for an additional 24h. At the time of analysis, the cells were washed with PBS, fixed with 4% paraformaldehyde for 20 min, permeabilised with a solution containing 0.1% Triton X-100 in PBS for 10 min, and blocked with 1% BSA in PBS for 1h at room temperature. Primary antibodies (**Supplementary Table 4**) were then applied overnight at 4°C. In some experiments, Alexa Fluor-488 Phalloidin (Life Technologies, 1:40) was added for labelling the actin cytoskeleton. Slides were washed and secondary antibodies applied for 1h in blocking solution at the final concentration of 1:200. After washing, cell nuclei were labelled with DAPI (1 µg/ml) or DRAQ5 (20 µM, Thermo Fisher Scientific) and the slides mounted.

Duolink staining

bEnd.3 cells were seeded on poly-L-lysine-coated glass coverslips in a 48-well plate and incubated for 24h with PBS, CREMO- or PTX-EVs (50 µg/ml) from 4T1 cells. Cells were then washed with PBS and fixed with 4% paraformaldehyde for 20 min. After several washes with PBS, cells were permeabilised with 0.3% Triton for 20 min. The Duolink PLA technology (Sigma) was then applied to examine physical proximity between ANXA6 and p65. Specifically, the Red Starter Kit Mouse/Rabbit was used according to the manufacturer's instructions. The primary rabbit anti-ANXA6 (Life Technologies, 720161) and mouse anti-p65 (Santa Cruz, clone F-6, sc-8008) antibodies were incubated overnight at 1:400 and 1:150, respectively, together with Alexa Fluor-488 Phalloidin (Life Technologies, 1:40) for labelling the actin cytoskeleton.

Image acquisition by confocal microscopy

In order to image immunostained tissue sections and cultured cells, we used a Zeiss LSM700 confocal microscope coupled to a high sensitivity Axiocam MRm (B/W) camera. Fluorescent signals from individual fluorophores were acquired sequentially from single optical sections, analysed and pseudocoloured using the ZEN software (Zeiss) or ImageJ.

Subcellular localization of mCh by immunofluorescence staining and confocal microscopy

To determine the subcellular localization of mCh in 4T1-mCh cultures exposed to drugs, confocal images were analysed using the ImageJ software. For each cell, the lining of the plasma membrane (+/- 0.5 µm) was determined manually by visualizing beta-tubulin immunostaining and saved as a region of interest (ROI), while the lining of the nucleus was determined according to DAPI staining by applying a Yen threshold with the Analyze particle tool of ImageJ. The cytoplasmic area was defined as the area between the plasma membrane and the nucleus. mCh signal intensity was calculated in both plasma membrane and cytoplasm compartments, and expressed as a ratio.

Quantification of mCh and ANXA6 transfer to ECs

To study mCh transfer, bEnd.3 cells were seeded in 24-well plates either directly on the plastic (for FACS and Western blotting) or on poly-L-lysine-coated glass coverslips (for immunofluorescence staining). Cells were then treated with purified EVs (1-200 µg/ml of total protein) or medium conditioned by cultured cancer cells (CM). Before use, CM was centrifuged at 500 x g for 5 min; 2000 x g for 5 min; and 4600 x g for 20xmin, at 4°C to remove dead cells, debris and large vesicles. bEnd.3 cells were then allowed to grow for additional 24h before analysis. Before analysis, the cells were extensively washed with PBS and treated with trypsin/EDTA to detach them (FACS), or lysed with RIPA buffer, or fixed with paraformaldehyde (immunofluorescence staining).

Chemicals and cytokines

Cas-BIND Pro Pan Caspase Pro-VAD-FMK (Verget Bioscience) or control DMSO were added to 40-50% confluent cells at a final concentration of 10 µM in EV-depleted medium. After 2h, PTX (100 ng/ml) or CREMO were added for another 72h. The cell permeant chelator BAPTA-AM (Life Technologies) or control DMSO were added to 40-50% confluent cells to a final concentration of 3 µM in EV-depleted medium. After 2h, PBS, PTX (100 ng/ml), DOX (200 ng/ml) or the appropriate vehicle were applied for another 48h. Recombinant human TNFα was purchased from Peprotech and used at 20 ng/ml in complete growth medium.

Cell viability and apoptosis assays

Cell viability was assessed by a WST-1 assay (Roche) according to the manufacturer's instructions. Briefly, 5000 cells were seeded in 96-well plates and treated with drugs as described above. After 72h, 10 µl of WST-1 reagent was added to each well and absorbance at 450 nm was measured using a TECAN plate-reader (TECAN).

Cell apoptosis was assessed by FACS analysis of biotin-conjugated AnnexinV (BD Biosciences) and 7AAD (Sigma), according to the manufacturer's instructions. Briefly, 200000 cells were seeded in 6-well

plates and treated with drugs. After 48h, the cells were trypsinized and transferred to a tube along with the conditioned medium. Cells were centrifuged at 2000 rpm, washed with ice-cold PBS, and resuspended in 1x binding buffer at a concentration of 10^6 cells/ml. The cell suspension was then stained with biotin-conjugated AnnexinV for 15 min at room temperature, followed by streptavidin-eFluor 450 (eBioscience; 1:100) for 15 min on ice. After washing, cells were resuspended in 7AAD (1:200) and immediately analysed by FACS.

Gene expression analyses by quantitative polymerase chain reaction (qPCR)

Small tissue fragments were obtained from the lungs of perfused tumour-free or bearing mice, washed in PBS, frozen on dry ice, and stored at –80°C. Total RNA was purified using miRNeasy Mini kit guidelines (Qiagen). RNA was quantified with a NanoDrop ND-2000 and retrotranscribed using SuperScript®Vilo cDNA synthesis kit (Invitrogen).

All qPCR reactions were performed using the following TaqMan gene assays: *Hprt* Mm 01545399-m1, *B2m* Mm 00437762_m1, *Gapdh* Mm99999915_g1 *Angpt2* Mm00545822_m1, *Csf1* Mm00432686_m1, *Il6* Mm00446190_m1, *Cxcl12* Mm 00445553-m1, *Ccr2* Mm04207877_m1, and *Ccl2* Mm00441242, all from Applied Biosystems/Life Technologies. Each assay was performed in three technical replicates using 10 ng of total cDNA per reaction and 2x TaqMAN Universal master mix (Life Technologies). qPCR reactions were performed for 40 cycles in standard mode using an ABI7900HT apparatus (Applied Biosystems). Raw data were extracted and evaluated using the SDS software v2.4. For the analysis of the results, we calculated the average of the median threshold cycle (C_t) of one or two reference genes (*Hprt, Gapdh* and/or *B2m*) for each sample (reference C_t), as described previously [66].

Western blotting

Cells or purified EVs were lysed in ice-cold RIPA buffer containing Halt protease and phosphatase inhibitors (Thermo Fisher Scientific). Conditioned medium (CM) was concentrated using Vivaspin® 20 columns (5000K MW cutoff, Sartorius). Protein concentration was determined by BCA Protein Assay Reagent Kit (Thermo Fisher Scientific). Proteins were denatured at 95°C for 5 minutes with 6x Laemmli buffer (Bioworld), or at 90°C for 10 min with LDS Sample buffer 4x and Reducing agent 10x (both from Life Technologies). Unless stated otherwise, matched protein amounts for each sample were analysed in each experiment.

Proteins (10 to 20 µg) were separated by 12% or 4-12% (gradient) SDS-PAGE (Life Technologies) and blotted onto PVDF membranes (Amersham Hybond 0.45 µm, GE Healthcare). Membranes were blocked with 5% milk in TBS-T for 24h, incubated with primary antibodies (**Supplementary Table 4**) for 12 h at 4°C, and then with HRP-conjugated secondary antibodies for 1h at room temperature. Proteins of interest were visualized using ECL Western Blotting substrate (Pierce, Rockford, IL, USA) and a Fusion FX7 device (Peqlab). In some experiments, PVDF membranes were instead blocked with Odyssey Blocking Buffer (LI-COR Biosciences), incubated with primary antibodies for 12 h at 4°C, followed by IRDye 800CW or 680RD-conjugated secondary antibodies (LI-COR Biosciences) in 0.1% Tween and 0.01% SDS for 1h at room temperature. Blots were imaged on the LI-COR Odyssey scanner.

ELISA

After dissection, lungs were immediately frozen on dry ice and stored at -80°C. For protein extraction, lungs were washed with ice-cold PBS and minced into small fragments before mechanical homogenization in PBS containing Halt phosphatase and protease inhibitors (Thermo Fisher Scientific). After three freeze-thaw cycles to break cellular membranes, homogenates were centrifuged at 13000 rpm for 15 min at 4°C. To measure CCL2, we used the Quantikine Mouse/Rat CCL2/MCP-1 Immunoassay from R&D (MJE00) and 50 mg of total protein for each reaction. ELISA was performed according to the manufacturer's instructions. Absorbance was measured using a TECAN Safire2 plate-reader (TECAN).

To examine if ANXA6 localizes on the EV surface, we used a homemade ELISA and a polyclonal anti-ANXA6 antibody (720161, Thermo Fisher Scientific). Antibodies against the endoplasmic reticulum protein GP96 (clone 9G10, Enzo) or the extracellular domain of CD81 (clone B-11, Santa Cruz) were used as negative and positive control for staining the outer EV surface, respectively. The antibodies were diluted (5 µg/ml) in ELISA coating solution (Thermo Fisher Scientific) and used for coating a Nunc MaxiSorb 96-well plate (Thermo Fisher Scientific). The plate was then blocked with ELISA blocking solution (Thermo Fisher Scientific) and washed (two washes with PBS with 0.04% Tween, followed by two with PBS only) before adding the EVs (150 µg/ml, in PBS) for an overnight incubation at 4°C. Acquisition of EV-associated mCh fluorescence, before and after four washes with PBS to remove unadsorbed EVs, used a TECAN Safire2 plate-reader. A final acquisition was performed after the lysis of the EVs with 0.3% Triton in PBS for 2h at 4°C and three PBS washes.

EDTA treatment of EVs

To examine the localization of ANXA6 in EVs, EVs were treated with PBS or EDTA in PBS (1 mM) for 30 min at 37°C. After washing three times in PBS, the EVs were loaded onto Vivaspin® 500 columns (300000 MW cutoff, Sartorius) and centrifuged at 4000 x g for 15 min to retain EVs and discharge free macromolecules, before Western blotting analysis.

Late endosome enrichment

Cells were treated with drugs for 24h. After cell homogenization with a 25-gauge needle, we enriched late endosomes by continuous density gradient centrifugation [67]. The 25%/HB interface, enriched in late endosomes, and the 35%/40.6% interface, enriched in heavier membranes (e.g., endoplasmic reticulum and mitochondria), were collected and concentrated by ultracentrifugation (100000 x g for 1h) using a Beckman ultracentrifuge. The 40.6% fraction enriched in cytosolic proteins was also collected to concentrate proteins with Vivaspin® 20 columns (3000K MW cutoff, Sartorius).

NF-kB reporter assay

Cells were transduced with the NF-kB reporter LV and treated with 10 µg/ml EVs several weeks after transduction. Two days post-EV treatment, the cells were trypsinized, washed in EDTA and analysed by FACS. To quantitate NF-kB activity, we calculated the fluorescence intensity of both GFP and mCh after subtracting the background fluorescence of untransduced cells. In studies involving PTX-EVs, NF-kB activity was determined as the ratio between mCh and GFP fluorescence. In studies involving DOX-EVs, NF-kB activity was determined from GFP fluorescence, as DOX is fluorescent in the red channel.

Liquid chromatography-tandem mass spectrometry (LC-MS/MS)

EVs (17 µg) of PTX- or CREMO-treated 4T1 cells were directly analysed by LC-MS/MS. EV-derived proteins of MDA-MB-231 cells (1 µg) or human plasma (1 µg) were first resolved on a denaturing 4-12% polyacrylamide gradient gel. Gel slices were excised in the area predicted to contain ANXA6 (ranging from 60 to 85 kDa) to elute proteins for LC-MS/MS.

To perform LC-MS/MS, we applied a previously published procedure [68]. Briefly, peptides were desalted using StageTips, dried in a vacuum concentrator, and separated by reverse phase chromatography using a Dionex Ultimate 3000 RSLC nano UPLC system connected in-line with an Orbitrap Elite (Thermo Fisher Scientific). Database search was performed using Mascot 2.5 (Matrix Science) and SEQUEST in Proteome Discoverer v.1.4. against a murine or human Uniprot protein database. Data were further processed and inspected in ScaffoldTM 4.8.4 (Proteome Software); quantitative values normalized to total spectra were used to compare the proteomic profiles.

Plasma isolation from breast cancer patients

Using an IRB-approved sample collection protocol at the Massachusetts General Hospital Cancer Center, subjects were consented for serial venous blood collections. The study was compliant with all relevant ethical regulations regarding research involving human participants. Plasma samples were obtained from six women diagnosed with invasive breast cancer with histopathologically confirmed tumour stage ranging from IA to IIIA; immunohistochemical subtyping and lymph node status of each patient are reported in **Supplementary Table 2**. All subjects had 20 ml of blood collected into Streck tubes prior to initiation of neoadjuvant chemotherapy, which consisted of four cycles of every two week dose-dense DOX at 60 mg/m2 and cyclophosphamide at 600 mg/m^2 (AC), followed by four cycles of every two week PTX at 175 mg/m^2. A second 10 ml blood sample was collected prior to starting PTX (on the day of the first PTX infusion), and a third 10 ml blood sample on the last or second-to-last cycle of PTX.

All blood samples were centrifuged at 1600 x g at room temperature for 10 min. The supernatant (plasma) was then transferred to one fresh 10 ml centrifuge tube without disturbing the cellular layer, and centrifuged at 3000 x g at room temperature for 10 min. The supernatant from the second centrifugation was stored into 2 ml pre-labelled cryogenic vials at -70°C. Before EV isolation, plasma was centrifuged at 10000 x g for 20 min at 4°C; one ml of plasma was processed for EV isolation.

Statistics and reproducibility

Information on the study outline, sample size and statistical analysis is presented in the main text, figures, and figure legends. Studies involving independent cohorts of mice were typically performed once, with the exceptions stated in the figure legends. Each study was designed to use the minimum number of mice required to obtain informative results (i.e., quantitative data suited to statistical analysis) and sufficient material for further studies. No specific statistical tests were used to predetermine the sample size.

The investigators were not blinded when assessing the results or analysing data. On rare occasions, outliers at end-point were excluded by using the ROUT method (GraphPad Prism) to identify outliers. In rare cases, selected samples were lost or excluded from specific analyses because of technical flaws during

sample collection, processing or data acquisition.

The number of biological (non-technical) replicates for each experiment is indicated in the figure legends. All experiments were repeated independently with similar results. When less than three biological replicates were available, statistics were not computed. Data are shown as mean values ± standard error of the mean (s.e.m.) for most analyses, with the exception of *in vitro* studies with a sample size of n=3, in which mean values ± standard deviation (s.d.) are reported. In experiments involving animals, each dot in the chart represents one mouse or zebrafish embryo. Source data for all experiments are provided in **Supplementary Table 5**.

Statistical analysis of the data was performed using the GraphPad Prism software. Statistical analysis of differentially expressed proteins in the LC-MS/MS 4T1-EV study was performed using an unpaired two-tailed t-test implemented in R; *P* values were adjusted after correcting for false discovery rate using a Benjamini-Hochberg method. Statistical analysis of experiments involving more than two experimental groups used one-way ANOVA with Tukey's correction for multiple comparisons, unless indicated otherwise. When the influence of two nominal variables on one measurement variable was examined, a two-way ANOVA followed by Tukey's or Sidak's correction was applied. Experiments involving two experimental groups were analysed by unpaired two-tailed student's *t*-test with 95% confidence interval, unless indicated otherwise.

Statistical significance of the data is summarized as follows: $*P < 0.05$, $**P < 0.01$, $***P < 0.001$, $****P < 0.0001$. Differences among experimental groups were considered significant at *P* values of less than 0.05. Exact *P* values are provided in all instances, except when $P > 0.05$ or $P < 0.0001$.

Reporting summary

Further information on experimental design is available in the Nature Research Reporting Summary linked to this paper.

Data availability

Uncropped and replicate Western blots not shown in the figures are provided as **Supplementary Figure 9**.

4T1-EV data have been submitted to the EV-TRACK knowledgebase (EV-TRACK ID: EV180041) (Ref. 69). The mass spectrometry proteomics data have been deposited to the ProteomeXchange Consortium via the PRIDE partner repository [70] with the following dataset identifiers: PXD010362 (accession) and 10.6019/PXD010362 (DOI) for the 4T1 EV data; and PXD010292 (accession) and 10.6019/PXD010292 (DOI) for the human EV data.

Source data for all graphical representations are provided as **Supplementary Table 3** and **Supplementary Table 5**. All other data supporting the findings of this study are available from the corresponding authors on request.

References

58 Kitamura, T. *et al.* Monocytes Differentiate to Immune Suppressive Precursors of Metastasis-Associated Macrophages in Mouse Models of Metastatic Breast Cancer. *Front Immunol.* **8**,

2004 (2017).
59 Xu, J. Preparation, culture, and immortalization of mouse embryonic fibroblasts. *Curr Protoc Mol Biol* **Chapter 28**, Unit 28 21, doi:10.1002/0471142727.mb2801s70 (2005).
60 Squadrito, M. L. *et al.* Endogenous RNAs modulate microRNA sorting to exosomes and transfer to acceptor cells. *Cell Rep.* **8**, 1432-1446 (2014).
61 De Palma, M. & Naldini, L. Transduction of a gene expression cassette using advanced generation lentiviral vectors. *Methods Enzymol* **346**, 514-529 (2002).
62 Cianciaruso, C. *et al.* Primary Human and Rat beta-Cells Release the Intracellular Autoantigens GAD65, IA-2, and Proinsulin in Exosomes Together With Cytokine-Induced Enhancers of Immunity. *Diabetes* **66**, 460-473 (2017).
63 Chiou, N.-T. & Ansel, M.K. Improved exosome isolation by sucrose gradient fractionation of ultracentrifuged crude exosome pellets. *Protocol Exchange* DOI:10.1038/protex.2016.057(2016).
64 Gray, C. *et al.* Simultaneous intravital imaging of macrophage and neutrophil behaviour during inflammation using a novel transgenic zebrafish. *Thromb Haemost.* **105**, 811-819 (2011).
65 Motoike, T. *et al.* Universal GFP reporter for the study of vascular development. *Genesis* **28**, 75-81 (2000).
66 Keklikoglou, I. *et al.* Periostin Limits Tumor Response to VEGFA Inhibition. *Cell Rep.* **22**, 2530-2540 (2018).
67 de Araujo, M. E., Lamberti, G. & Huber, L. A. Isolation of Early and Late Endosomes by Density Gradient Centrifugation. *Cold Spring Harb Protoc* **2015**, 1013-10164 (2015).
68 Chopra, T. *et al.* Quantitative mass spectrometry reveals plasticity of metabolic networks in Mycobacterium smegmatis. *Mol Cell Proteomics* **13**, 3014-3028 (2014).
69. Consortium, E.-T. *et al.* EV-TRACK: transparent reporting and centralizing knowledge in extracellular vesicle research. *Nat Methods* **14**, 228-232 (2017).
70 Vizcaino, J. A. *et al.* 2016 update of the PRIDE database and its related tools. *Nucleic Acids Res* **44**, 11033 (2016).

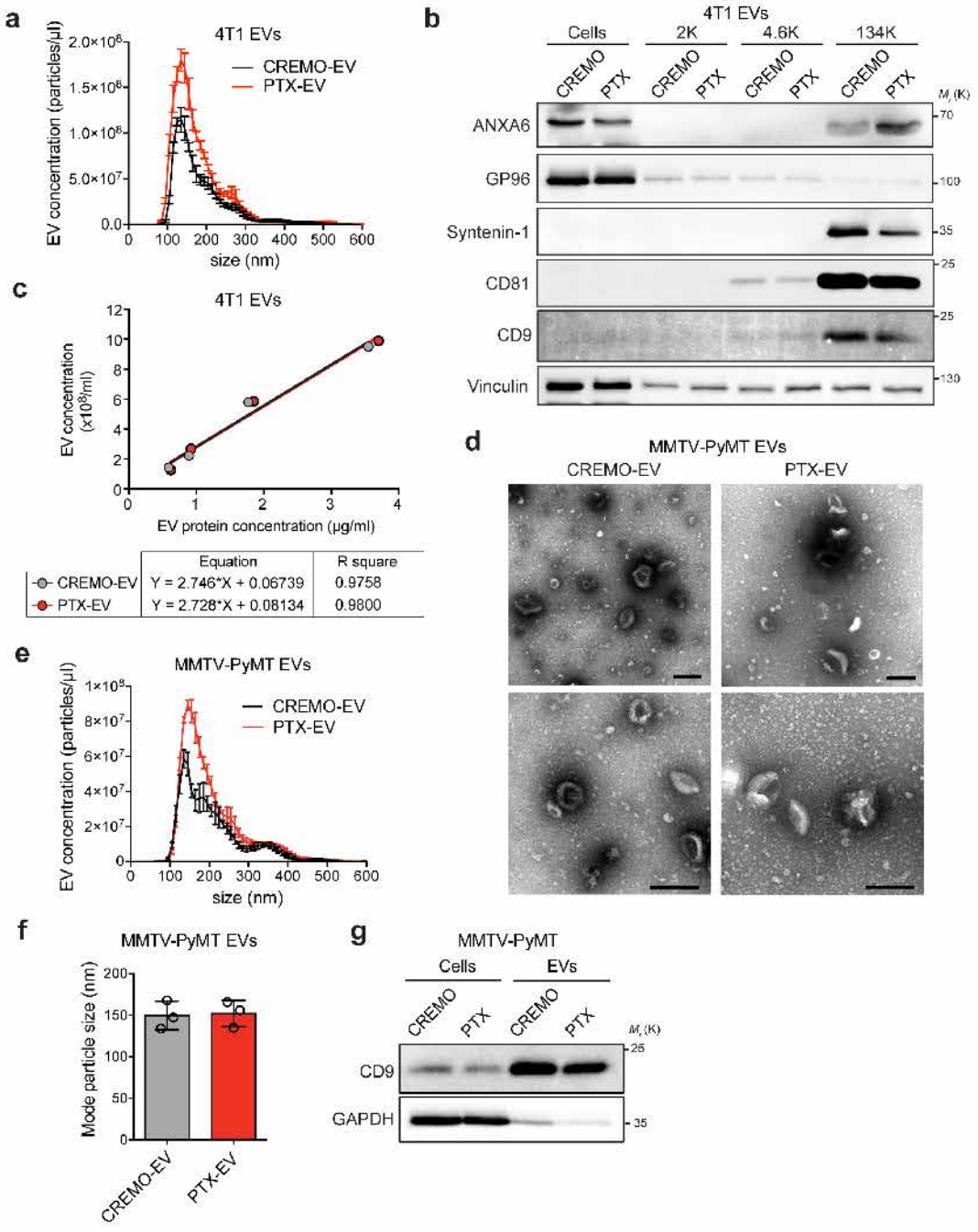

Supplementary Figure 1

PTX does not alter the physical features of mammary tumour-derived EVs

(a) Concentration (mean ± s.e.m.; n=5 acquisitions of one sample/condition) and size distribution of EVs isolated from medium conditioned by CREMO- or PTX-treated 4T1 cells, determined by NTA. **(b)** Western blotting analysis of the indicated proteins in material recovered after low-speed (2,000 x g, 2K), medium-speed (4,600 x g, 4.6K) or high-speed (134,000 x g, 134K) centrifugation of medium conditioned by 4T1 cells treated as indicated. The experiment was performed once, but additional data on EVs isolated after high-speed centrifugation are also shown in Fig. 3d-f, h and Fig. 4c. **(c)** Correlation between EV protein content and EV concentration, measured by BCA and NTA, respectively, in EVs isolated from medium conditioned by 4T1 cells treated as indicated. Four serial dilutions and three technical replicates of one sample/condition were measured; the mean of technical replicates is shown. A simple linear regression function was used to determine the relationship between the two parameters. The amount of EVs contained in each

EV dose administered to mice (15 µg) was determined by extrapolation of the data. **(d)** Representative TEM images of EVs isolated *ex vivo* from MMTV-PyMT tumours that had been treated *in vivo* with either CREMO or PTX (see Fig. 2d). Scale bars, 200 nm. The experiment was performed once. **(e)** Concentration (mean ± s.e.m.; n=5 acquisitions of one sample/condition) and size distribution of MMTV-PyMT tumour-derived EVs obtained as in (d), determined by NTA. **(f)** Mode size (mean values ± s.d.; n=3 independent EV preparations) of MMTV-PyMT tumour-derived EVs obtained as in (d), determined by NTA. **(g)** Western blotting analysis of CD9 and GAPDH in MMTV-PyMT tumour-derived cells and their EVs. The experiment was performed once.
Source data are shown in **Supplementary Table 5** and unprocessed blots in **Supplementary Fig. 9**.

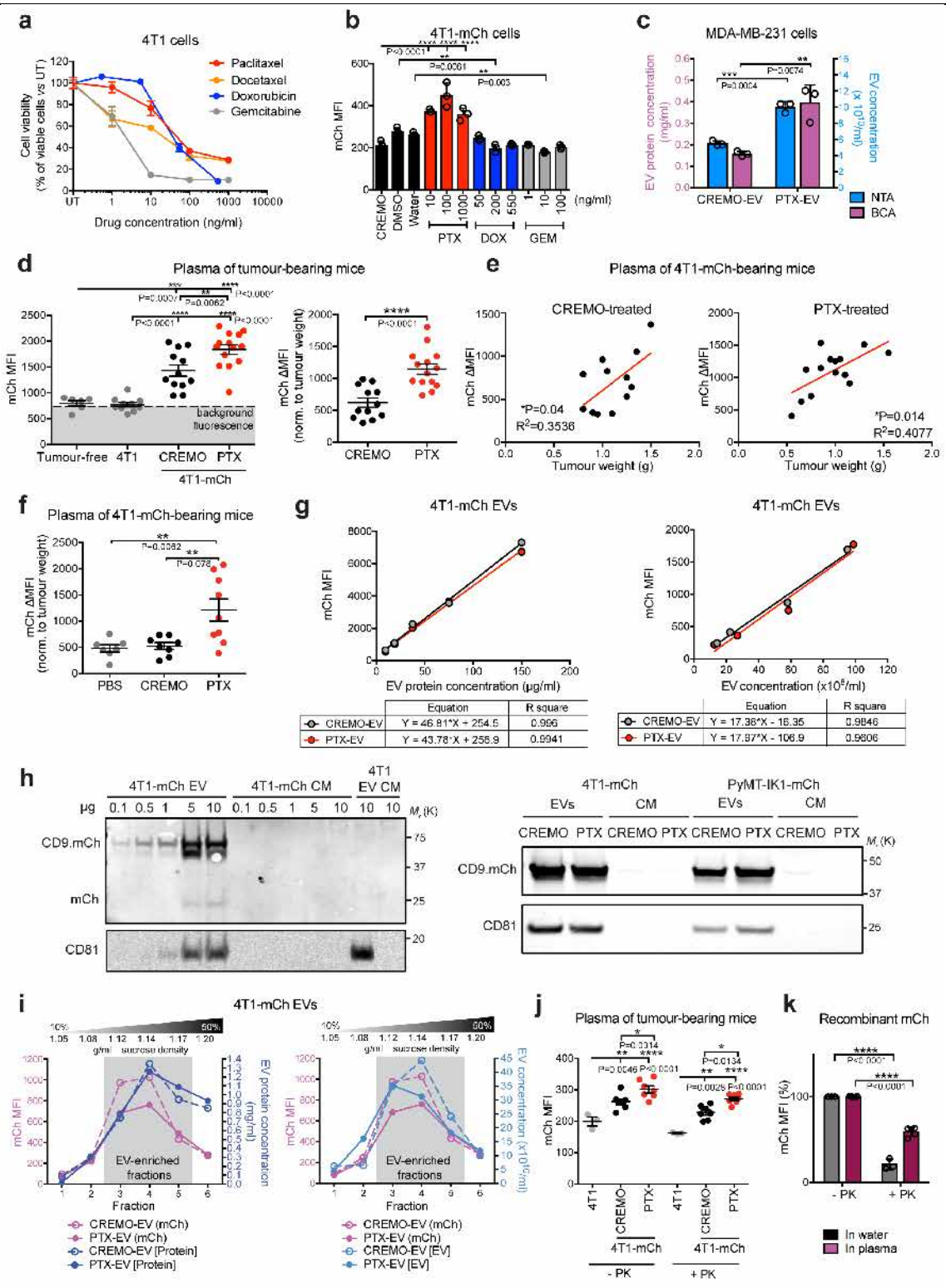

Supplementary Figure 2

PTX enhances EV release from cancer cells *in vitro* and in tumour-bearing mice

(a) WST-1 assay-based viability of 4T1 cancer cells (mean ± s.d.; n=6 independent cell cultures/condition) relative to untreated cells (UT). **(b)** mCh mean fluorescence intensity (MFI; mean ± s.e.m.; n=3 independent cell cultures/condition) in medium conditioned by

4T1-mCh cells treated for 72h as indicated. Statistical analysis by one-way ANOVA with Tukey's multiple comparison test. **(c)** Protein content by BCA (left y axis) and concentration by NTA (right y axis) in EVs (mean ± s.d.; n=3 independent cell cultures/condition) from MDA-MB-231 cells treated for 72h with CREMO or PTX. Statistical analysis by unpaired two-tailed Student's t-test. **(d)** Absolute mCh MFI (mean ± s.e.m.) in plasma of tumour-free (n=6), 4T1 tumour-bearing (n=10), and 4T1-mCh tumour-bearing *Rag1*$^{-/-}$ mice treated with CREMO (n=12) or PTX (n=14); two independent experiments combined (left panel). Statistical analysis as in (b). Right panel shows data after subtracting background fluorescence (ΔMFI; mean ± s.e.m.) and normalizing the results to tumour weight. Statistical analysis as in (c). **(e)** Correlation between tumour weight and mCh ΔMFI in plasma of mice shown in (d), right panel. The Pearson correlation coefficient (r) is indicated. **(f)** mCh ΔMFI (mean ± s.e.m.) in plasma of 4T1-mCh/HER2 tumour-bearing *Rag1*$^{-/-}$ mice (PBS, n=7; PTX, n=9; CREMO, n=8). Statistical analysis as in (b). **(g)** Correlation between mCh MFI and protein concentration by BCA (left) or particle concentration by NTA (right) in EVs from medium conditioned by 4T1-mCh cells. Five (left) or four (right) serial dilutions and three technical replicates of one sample/condition were measured; the mean of technical replicates is shown. A simple linear regression function was used to extrapolate relationship between the two variables. **(h)** Western blotting analysis of the indicated proteins in EVs or EV-depleted, concentrated conditioned medium (CM) from 4T1, 4T1-mCh or PyMT-IK1-mCh cells. EVs and CM were recovered after high-speed (134,000 x g) centrifugation. Each experiment was performed once. **(i)** mCh MFI and protein concentration by BCA (left) or particle concentration by NTA (right) in EVs isolated from medium conditioned by 4T1-mCh cells. Six EV fractions were obtained by sucrose fractionation of purified EVs. Three technical replicates of each EV fraction/condition were measured; the mean of technical replicates is shown. **(j)** mCh MFI (mean ± s.e.m.) in plasma of 4T1 (n=3) or 4T1-mCh (n=7) tumour-bearing *Rag1*$^{-/-}$ mice. Plasma was incubated with or without proteinase K (PK). Statistical analysis as in (b). **(k)** mCh MFI (mean ± s.e.m.) of recombinant mCh incubated with or without PK in either water (n=3 independent experiments/condition) or mouse plasma (n=4). Data show percentage values over untreated (-PK) samples. Statistical analysis by two-way ANOVA with Sidak's multiple comparison test.
Source data are shown in **Supplementary Table 5** and unprocessed blots in **Supplementary Fig. 9**.

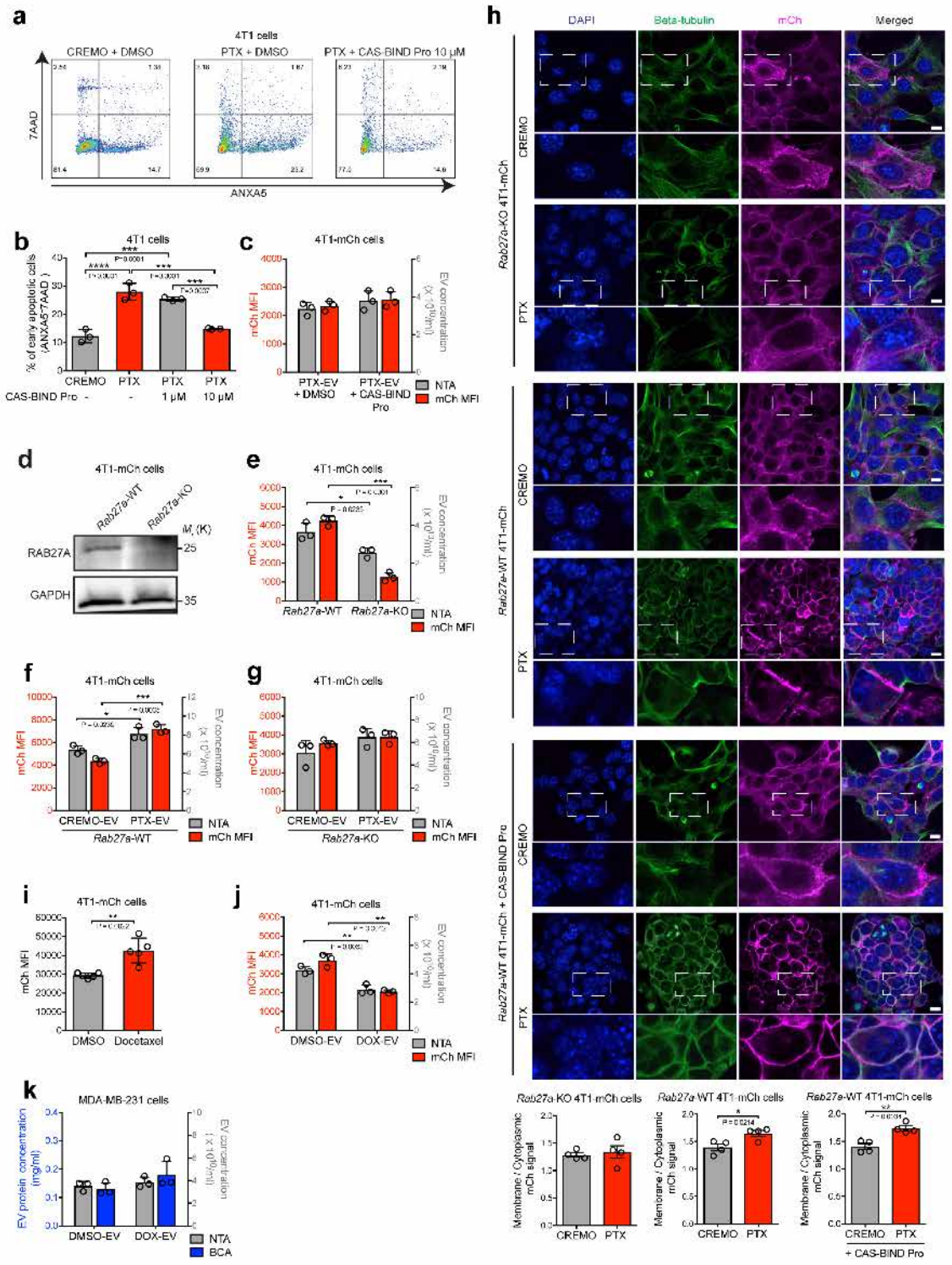

Supplementary Figure 3

PTX increases cancer cell-derived EV release in a RAB27A-dependent and apoptosis-independent manner

(a, b) FACS of 4T1 cells treated for 48h with CREMO or PTX (n=3 independent cell cultures/condition) in the presence of the pan-caspase inhibitor CAS-BIND Pro or DMSO (vehicle). Panel (a) shows representative FACS dot plots of cells stained for ANXA5 and 7AAD to identify early apoptotic ($ANXA5^{+}7AAD^{-}$) cells. Panel (b) shows quantitative data (mean ± s.d.). Statistical analysis by one-way

ANOVA with Tukey's multiple comparison test. **(c)** mCh MFI (left y axis) and concentration by NTA (right y axis) of EVs (mean ± s.d.; n=3 independent cell cultures/condition) from 4T1-mCh cells treated for 72h with PTX in the presence of CAS-BIND Pro or DMSO (vehicle). Statistical analysis by unpaired two-tailed Student's t-test. **(d)** Western blotting analysis of RAB27A and GAPDH in *Rab27a*-KO or WT 4T1-mCh cells. The experiment was performed once. **(e-g)** mCh MFI (left y axis) and concentration by NTA (right y axis) of EVs (mean ± s.d.; n=3 independent cell cultures/condition) from *Rab27a*-KO or WT 4T1-mCh cells treated as indicated. Statistical analysis as in (c). **(h)** Subcellular localization of mCh in 4T1-mCh cells treated as indicated. Panels above show representative images of cells stained with anti-beta-tubulin antibody (green) and DAPI (blue); mCh signal (magenta) was acquired as direct fluorescence. Scale bars, 10 μm. Panels below show ratio between membrane and cytoplasm-associated mCh signal (mean ± s.e.m.; n=4 randomly selected image fields, each containing at least 120 cells, per condition). Statistical analysis as in (c). Note increased localization of mCh to plasma membranes after PTX in RAB27A-proficient cells. **(i)** mCh MFI (mean ± s.d.; n=5 independent cell cultures/condition) of EVs from 4T1-mCh cells treated for 72h as indicated. Statistical analysis as in (c). **(j)** mCh MFI (left y axis) and concentration by NTA (right y axis) of EVs (mean ± s.d.; n=3 independent cell cultures/condition) from 4T1-mCh cells treated for 72h as indicated. Statistical analysis as in (c). **(k)** Protein content by BCA (left y axis) and concentration by NTA (right y axis) in EVs (mean ± s.d.; n=3 independent cell cultures/condition) from MDA-MB-231 cells treated for 72h as indicated. Statistical analysis as in (c).
Source data are shown in **Supplementary Table 5** and unprocessed blots in **Supplementary Fig. 9**.

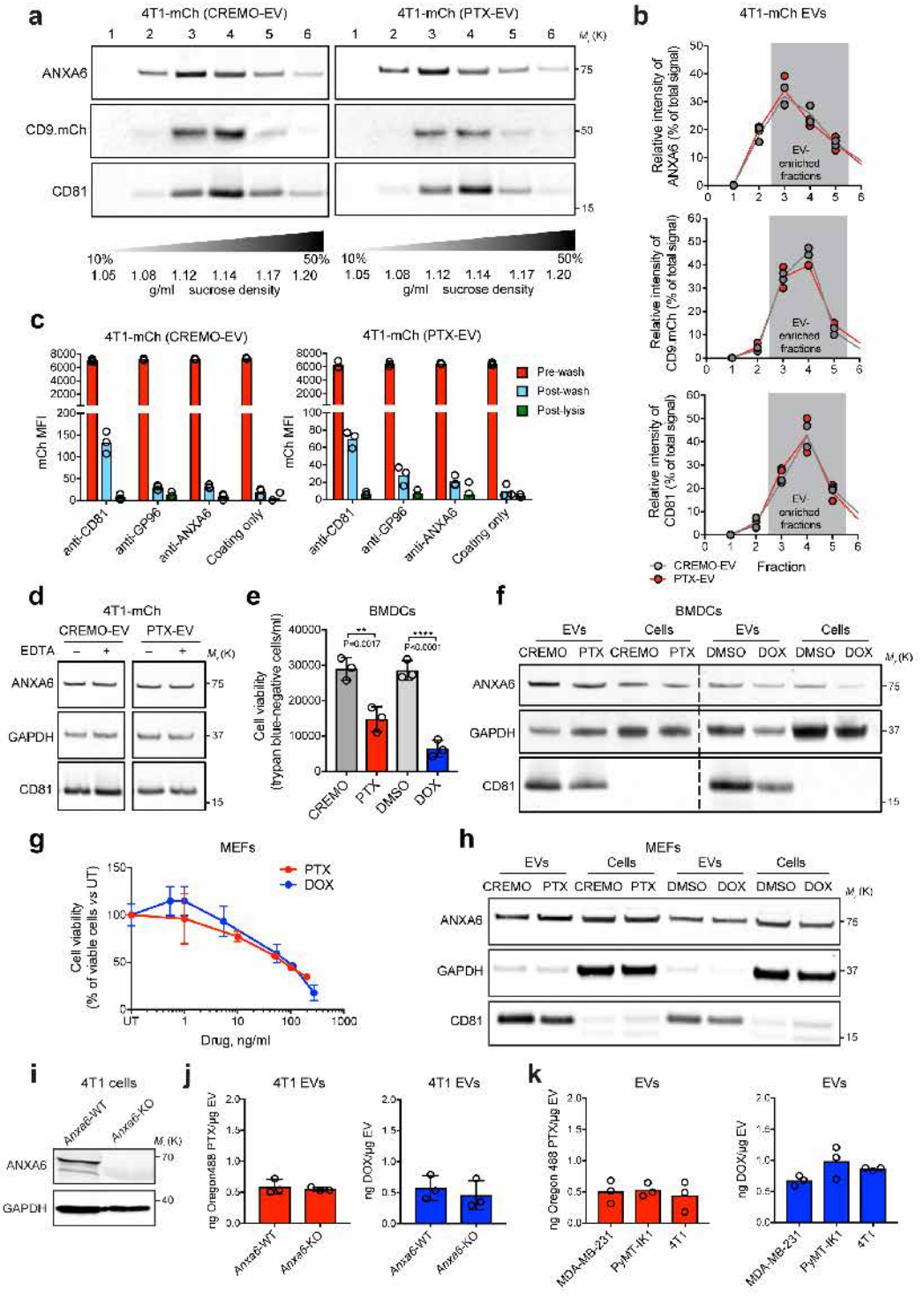

Supplementary Figure 4

PTX promotes loading of ANXA6 into *bona fide* cancer cell-derived EVs

(a) Western blot analysis of the indicated proteins in 4T1-mCh EVs after fractionation by sucrose density gradient centrifugation. Note the association of ANXA6 with EV fractions with a density ranging from 1.12 to 1.17 g/ml. One representative experiment is shown of two performed. **(b)** Protein band intensity (n=2 independent experiments, one of which is shown in (a) above) in the indicated EV fractions. For each protein, the relative signal intensity in each fraction is indicated as percentage of the total signal in all fractions. The

line connects mean values. **(c)** ELISA assay showing the binding of antibodies against CD81, GP96 or ANXA6 to CREMO-EVs and PTX-EVs. Note the limited binding of an anti-ANXA6 antibody to either EV preparation after washing, compared to the anti-CD81 antibody. Results show one EV sample per condition and the mean of three technical replicates. **(d)** Western blotting analysis of ANXA6, GAPDH and CD81 in CREMO-EV and PTX-EV incubated with EDTA or PBS. Note that EDTA did not reduce ANXA6 signal in EVs, indicating intra-vesicular localization. One representative experiment is shown of three performed. **(e)** Viability of primary mouse bone marrow dendritic cells (BMDCs; mean ± s.d.; n=3 independent cell cultures) treated as indicated for 72h. Statistical analysis by one-way ANOVA with Tukey's multiple comparison test. **(f**) Western blotting analysis of ANXA6, GAPDH and CD81 in CREMO-EV and PTX-EV isolated from BMDCs. One representative experiment is shown of two performed. **(g)** Viability of primary mouse embryonic fibroblasts (MEFs; mean ± s.d.; n=4 independent cell cultures) treated as indicated for 72h. **(h**) Western blotting analysis of ANXA6, GAPDH and CD81 in CREMO-EV and PTX-EV isolated from MEFs. The experiment was performed once. **(i)** Western blotting analysis of ANXA6 and GAPDH in *Anxa6*-WT (parental) and *Anxa6*-KO 4T1 cells. The experiment was performed once. **(j)** Quantification of Oregon Green 488 PTX (left) and autofluorescent DOX (right) in EVs (mean ± s.d.; n=3 independent cell cultures/condition) from *Anxa6*-WT or *Anxa6*-KO 4T1 cells. **(k)** Quantification of Oregon Green 488 PTX (left) and autofluorescent DOX (right) in EVs from MDA-MB-231, PyMT-IK1 and 4T1 cells. Data show mean values of three serial dilutions per sample.
Source data are shown in **Supplementary Table 5** and unprocessed blots in **Supplementary Fig. 9**.

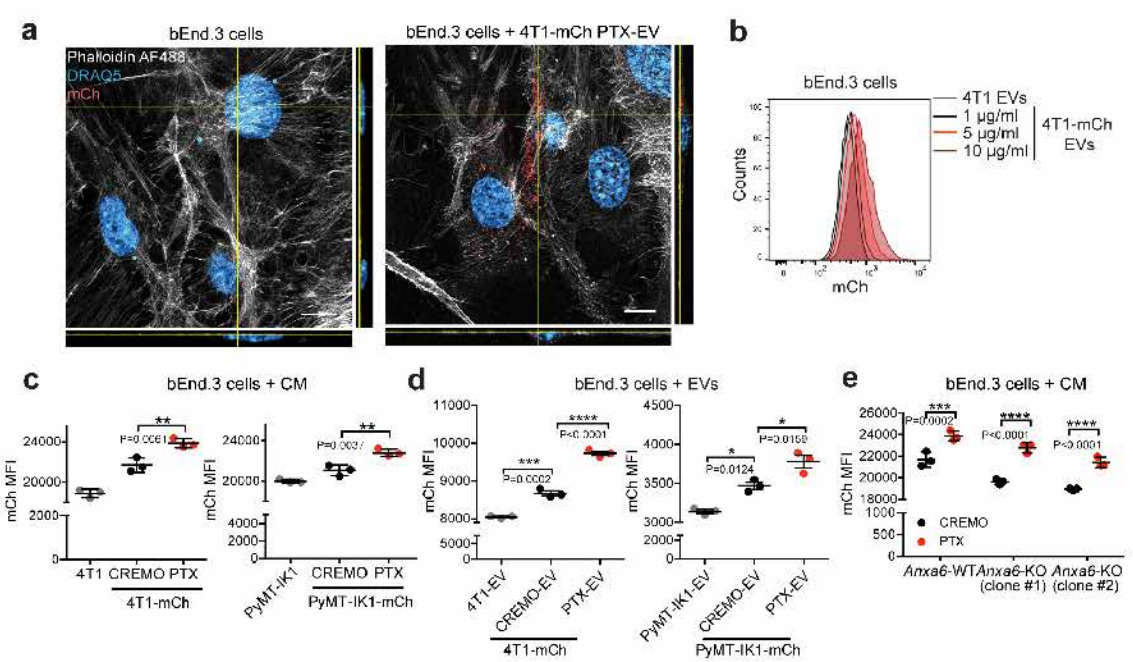

Supplementary Figure 5

EV transfer to ECs induces a drug-independent pro-inflammatory response

(a) Representative confocal images of bEnd.3 cells either untreated or incubated for 24h with PTX-EVs (50 µg/ml) from 4T1-mCh cells. Cells were stained with an anti-mCh antibody (red), AF488-conjugatd phalloidin (white) and DRAQ5 to reveal nuclei (cyan). Orthogonal projections from a z-stack acquisition are shown. Scale bars 10 µm. One image per condition is shown, representative of 3 independent experiments. **(b)** FACS analysis of bEnd.3 cells treated for 24h with increasing doses of EVs isolated from 4T1-mCh cells. One representative sample per condition is shown. **(c, d)** FACS analysis of mCh in bEnd.3 cells incubated with conditioned medium (CM; c) or purified mCh^+ EVs (d) from 4T1-mCh (left panels) or PyMT-IK1-mCh (right panels) cells treated as indicated. mCh-negative 4T1 and PyMT-IK1 cells were used as controls. Data show mCh MFI (mean ± s.d.; n=3 independent cell cultures/condition). Statistical analysis by one-way ANOVA with Tukey's multiple comparison test. **(e)** FACS analysis of mCh in bEnd.3 cells incubated with conditioned medium (CM) of *Anxa6*-WT or *Anxa6*-KO 4T1-mCh cells treated as indicated. Data show mCh MFI (mean ± s.d.; n=3 independent cell cultures/condition). Statistical analysis by two-way ANOVA with Sidak's multiple comparison test.
Source data are shown in **Supplementary Table 5**.

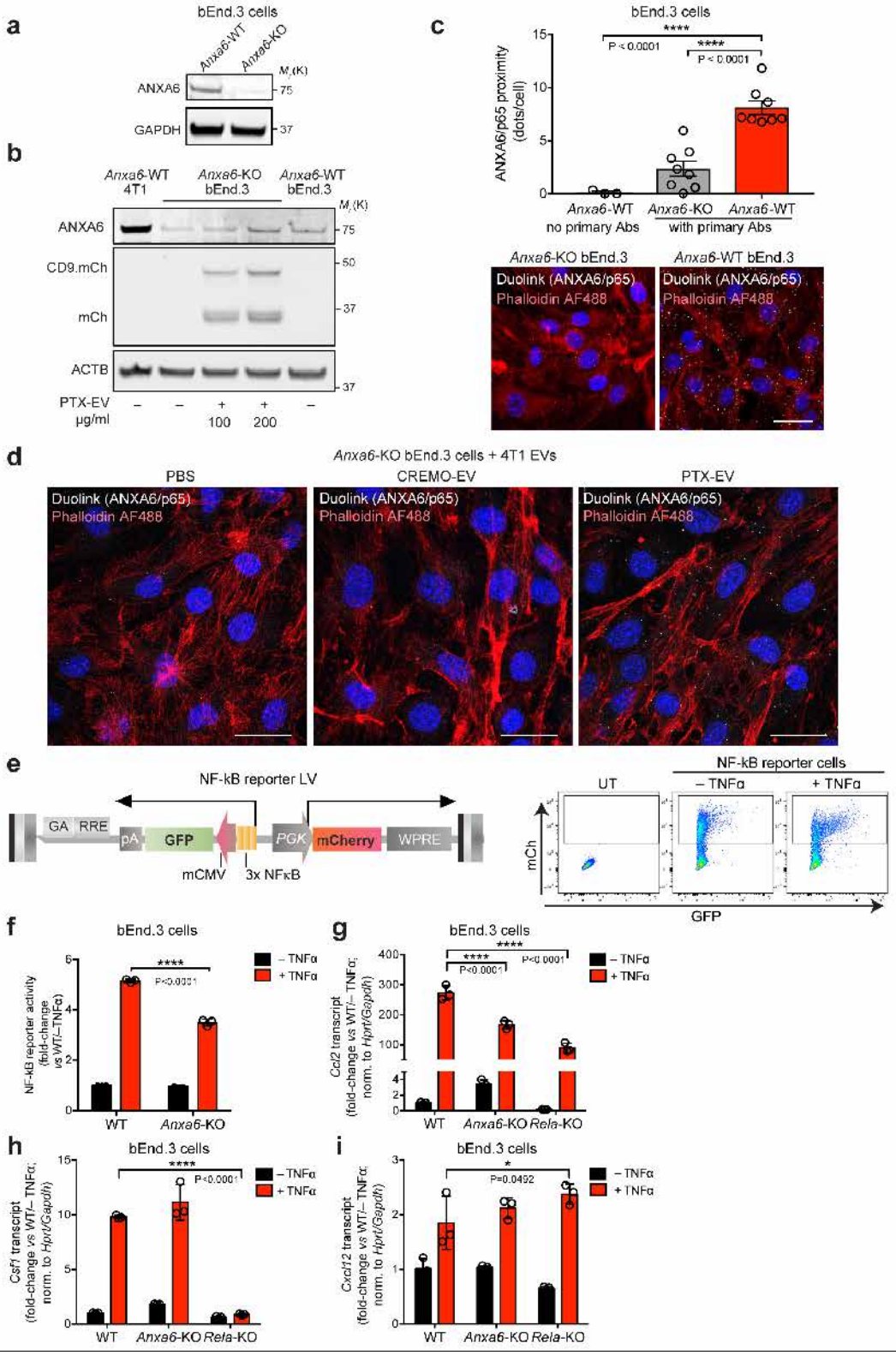

Supplementary Figure 6

ANXA6 induces NF-kB activation and *Ccl2* upregulation in bEnd.3 cells

(a) Western blotting analysis of ANXA6 and GAPDH in *Anxa6*-WT and KO bEnd.3 cells. The experiment was performed once. **(b)** Western blotting analysis of ANXA6, mCh and beta-actin (ACTB) in untreated *Anxa6*-WT 4T1 and bEnd.3 cells, as well as untreated or EV-treated *Anxa6*-KO bEnd.3 cells. One representative experiment of two performed; additional data are shown in Fig. 7d. **(c)** Duolink staining of bEnd.3 cells. Upper panel shows ANXA6/p65 proximity expressed as number of dots/cell (mean ± s.e.m.; n=8 randomly selected images with at least 12 cells each); unstained *Anxa6*-WT bEnd.3 cells (n=3 randomly selected images with at least 12 cells each) were used as negative control. Statistical analysis by one-way ANOVA with Tukey's multiple comparison test. Bottom panels show representative images; nuclei are stained with DAPI (blue), actin cytoskeleton with phalloidin (red). Scale bar, 30 µm. **(d)** Duolink staining of *Anxa6*-KO bEnd.3 cells treated as indicated. Images show ANXA6/p65 proximity (white dots); nuclei are stained with DAPI (blue), actin cytoskeleton with phalloidin (red). Scale bars, 30 µm. Results are representative of two independent experiments. **(e)** NF-kB activity in bEnd.3 cells. Left panel shows the NF-kB reporter lentiviral vector (LV). Note that red fluorescence of LV-encoded mCh is much stronger than the red fluorescence of EV-transferred mCh. Therefore, EV-derived mCh does not affect quantification of NF-kB reporter activity. Right panel shows representative FACS dot plots of bEnd.3 cells either untransduced (UT) or transduced with the NF-kB reporter LV before incubation with or without TNFα for 48h. Transduced (mCh^+) cells are gated and analysed for GFP expression. For quantitative data, see (f). **(f)** NF-kB activity determined by FACS analysis of transduced bEnd.3 cells incubated with or without TNFα for 24h. NF-kB activity is shown as GFP MFI in transduced (mCh^+) cells (mean ± s.d.; n=3 independent cell cultures/condition). Statistical analysis by two-way ANOVA with Tukey's multiple comparison test. **(g-i)** qPCR analysis of *Ccl2* (g), *Csf1* (h) and *Cxcl12* (i) in bEnd.3 cells incubated with or without TNFα for 5h (mean ± s.d.; n=3 independent cell cultures/condition). Statistical analysis as in (f). Source data are shown in **Supplementary Table 5** and unprocessed blots are shown in **Supplementary Fig. 9**.

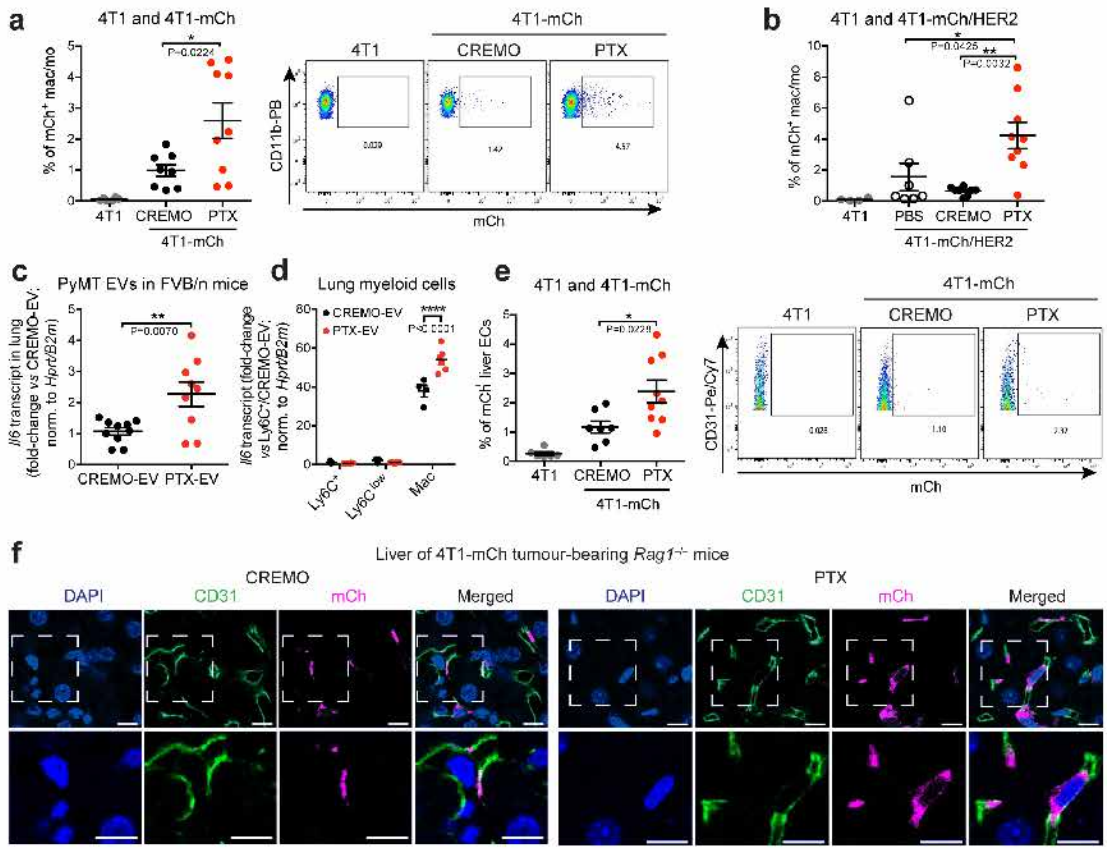

Supplementary Figure 7

Chemotherapy-elicited EVs display broad cellular tropism in tumour-bearing mice

(a) FACS analysis of $mCh^+CD45^+CD11b^+Ly6G^-$ macrophages/monocytes (mac/mono; mean ± s.e.m.; relative to viable lung-derived cells) in the lungs of 4T1 (n=6) or 4T1-mCh (CREMO, n=8; PTX, n=9) tumour-bearing *Rag1*$^{-/-}$ mice treated as indicated. Statistical analysis by one-way ANOVA with Tukey's multiple comparison test. The right panels show representative FACS dot plots. **(b)** FACS analysis of $mCh^+CD45^+CD11b^+Ly6G^-$ mac/mono (mean ± s.e.m.; relative to viable lung-derived cells) in the lungs of 4T1 (n=4) or 4T1-mCh/HER2 (PBS, n=7; CREMO, n=8; PTX, n=9) tumour-bearing *Rag1*$^{-/-}$ mice treated as indicated. Statistical analysis by one-way ANOVA with Tukey's multiple comparison test. **(c)** qPCR analysis of *Il6* in whole lung tissue (mean ± s.e.m.) of FVB/n mice that received either CREMO-EV (n=10) or PTX-EV (n=9). Statistical analysis by unpaired two-tailed Student's t-test. **(d)** qPCR analysis of *Il6* (mean ± s.e.m.) in FACS-sorted lung myeloid cells of FVB/n mice that received either CREMO-EV or PTX-EV (n=5 mice per group, except Mac/CREMO-EV where n=4). Statistical analysis by two-way ANOVA with Tukey's multiple comparison test. **(e)** FACS analysis of $mCh^+CD31^+CD45^-$ liver ECs (mean ± s.e.m.; relative to viable liver-derived cells) in the livers of 4T1 (n=6) or 4T1-mCh (CREMO, n=7; PTX, n=9) tumour-bearing *Rag1*$^{-/-}$ mice treated as indicated. Statistical analysis by one-way ANOVA with Tukey's multiple comparison test. The right panels show representative FACS dot plots. **(f)** Representative confocal immunofluorescence images of anti-CD31 EC (green) and anti-mCh (magenta) immunostaining of liver sections from 4T1-mCh tumour-bearing mice treated as in (e); nuclei are stained with DAPI (blue). Scale bars, 10 μm.

Source data are shown in **Supplementary Table 5**.

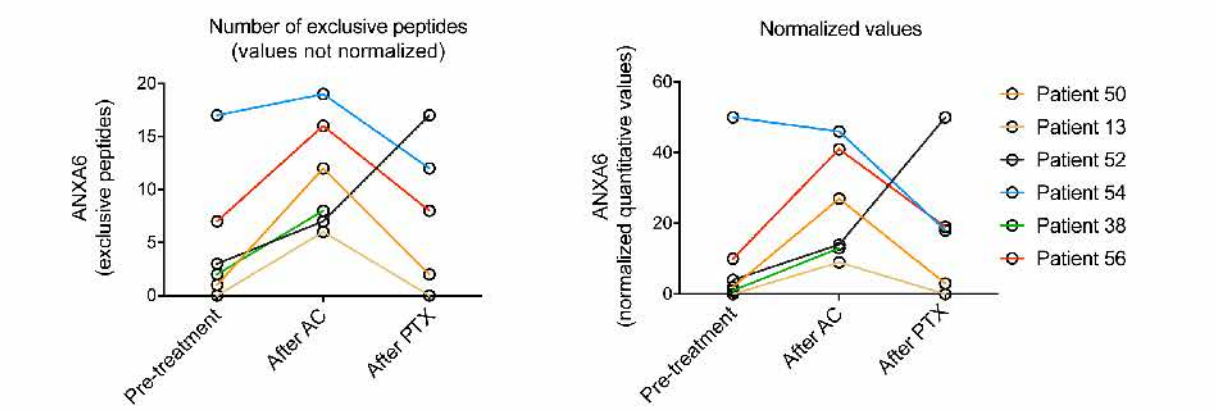

Supplementary Figure 8

ANXA6 is detected in circulating EVs of breast cancer patients undergoing neoadjuvant therapy

LC-MS/MS quantification of ANXA6 in EVs isolated from the plasma of six breast cancer patients before chemotherapy (pre-treatment), after AC (anthracycline (DOX)/cyclophosphamide) and after PTX. The data show the number of exclusive ANXA6 peptides (left) and the quantitative values after normalization to the total proteins identified in the same area of the gel (right).
Source data are shown in **Supplementary Table 3**.

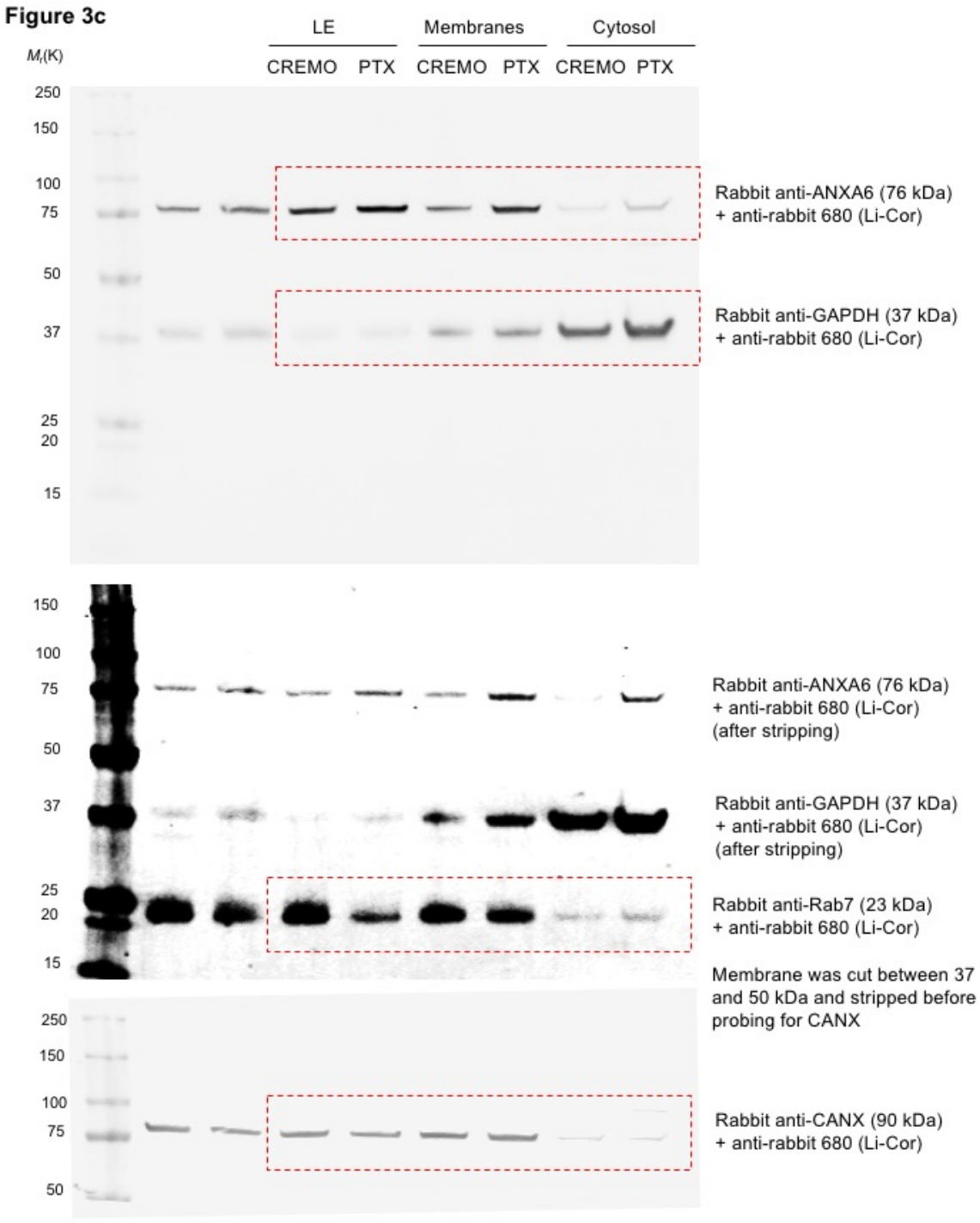

Supplementary Figure 9

Unprocessed blots

Unprocessed and uncropped blots for all Western blotting data reported in the main and supplementary figures of this study.

Figure 3d

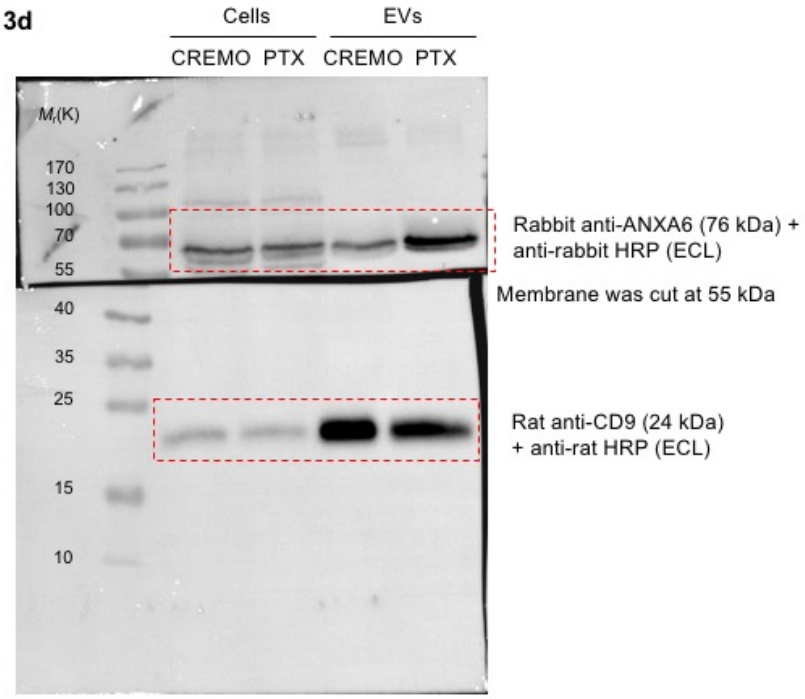

Figure 3e (top panels)

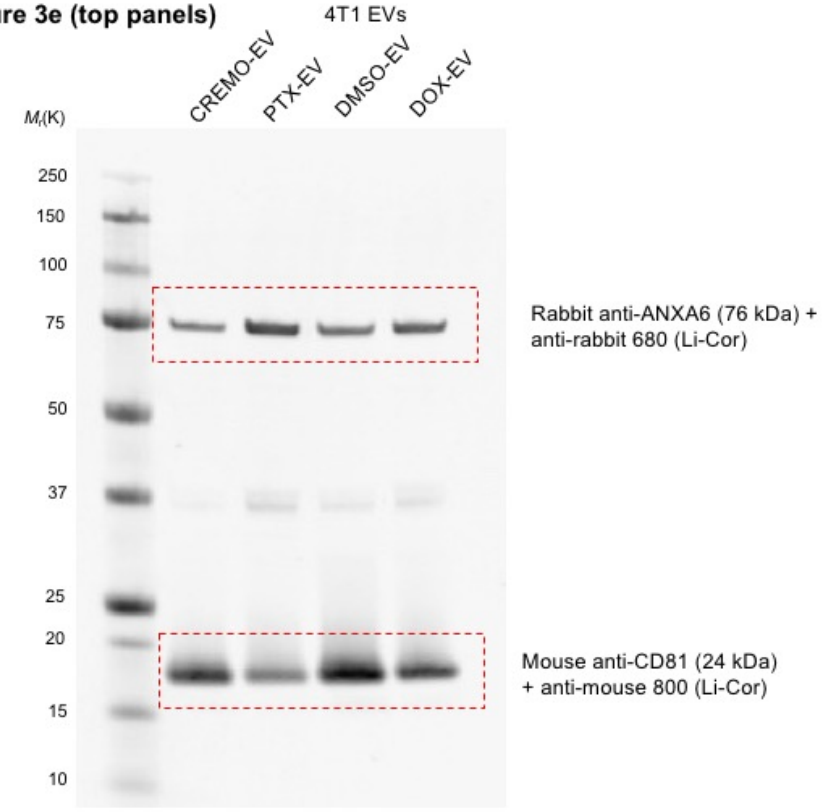

Supplementary Figure 9

Unprocessed blots (continued)

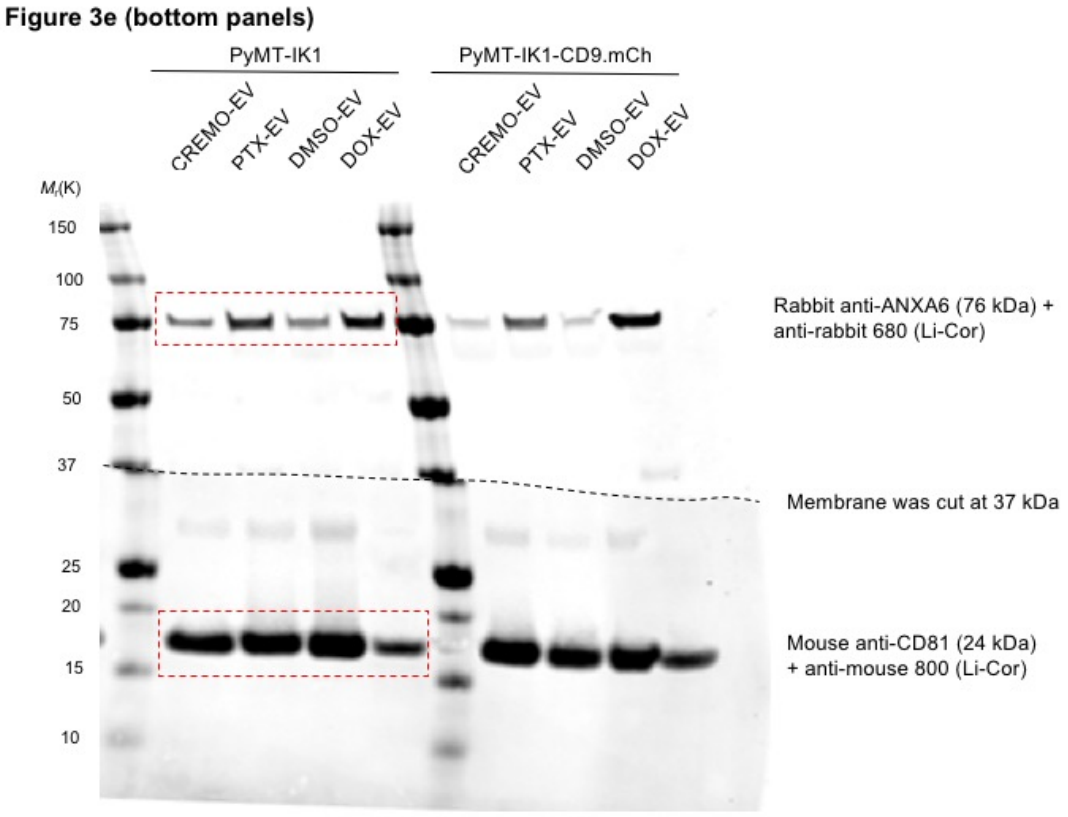

Supplementary Figure 9

Unprocessed blots (continued)

Figure 3f

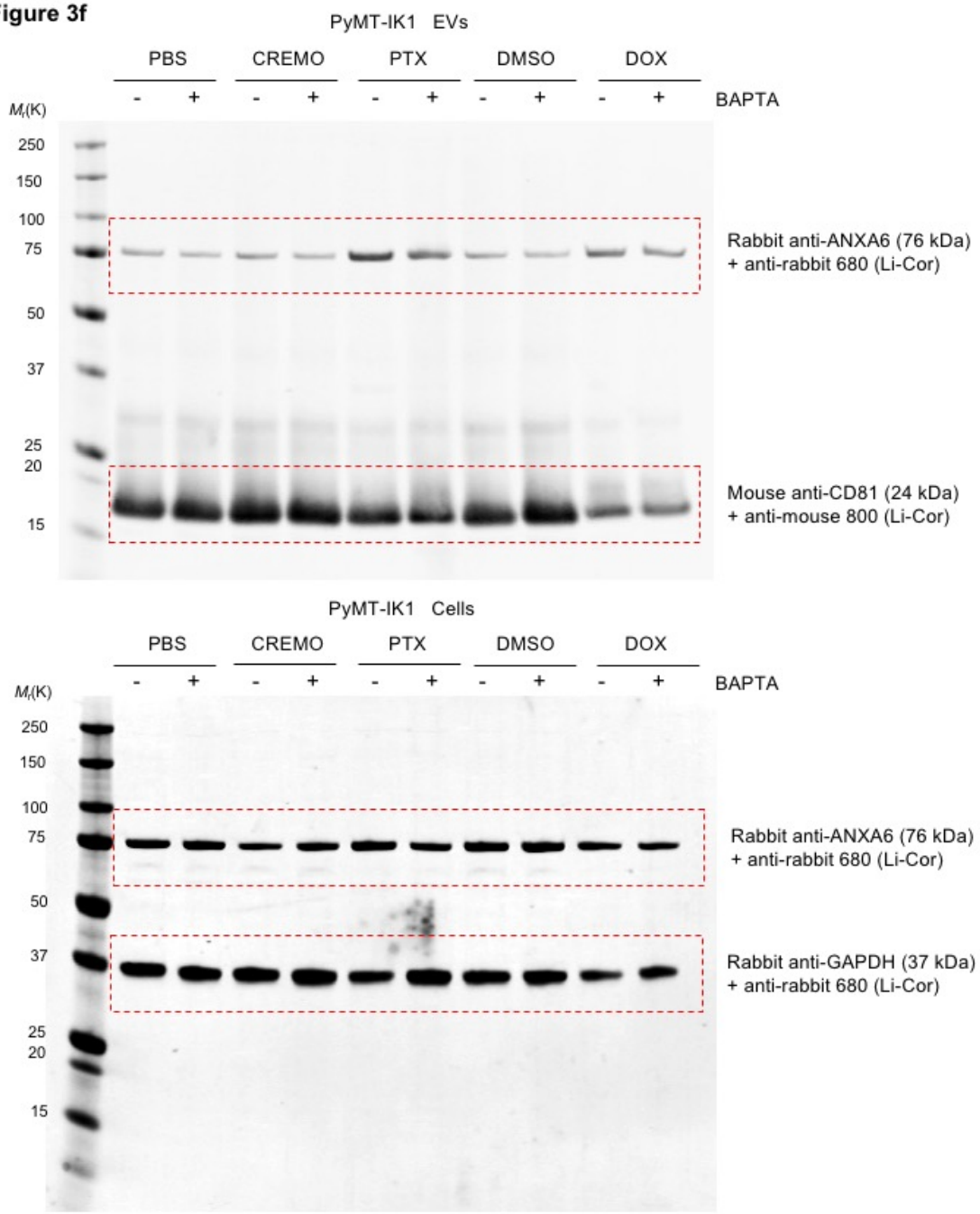

Supplementary Figure 9

Unprocessed blots (continued)

Repeat #2 associated to Fig. 3f (used for quantitative analysis, but not shown)

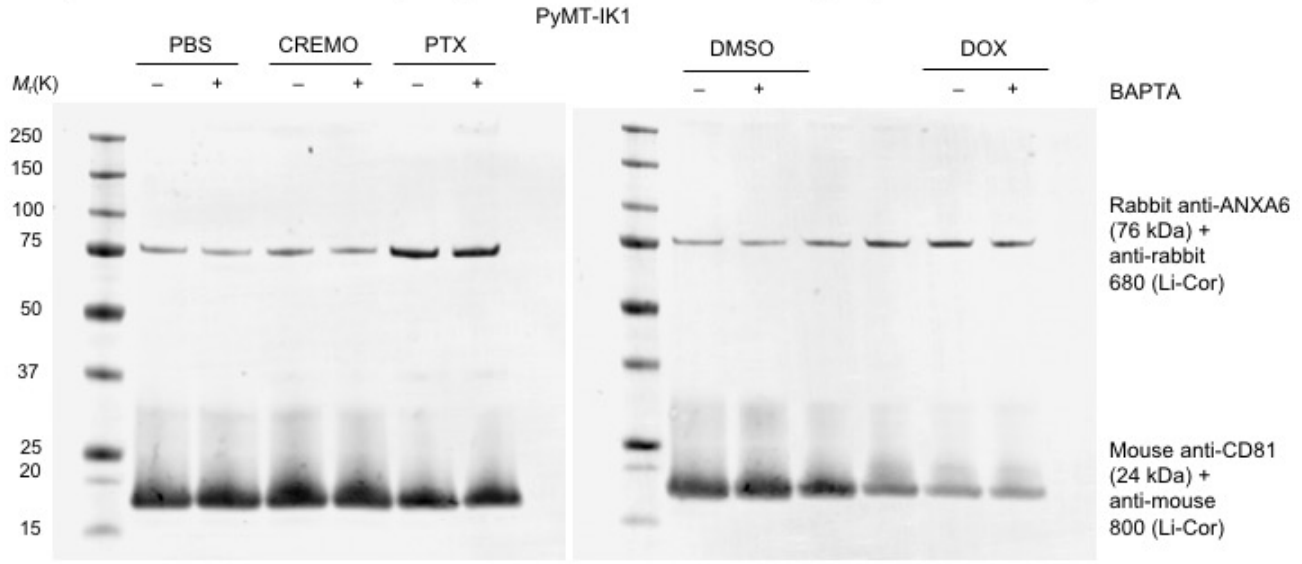

Repeat #3 associated to Fig. 3f (used for quantitative analysis, but not shown)

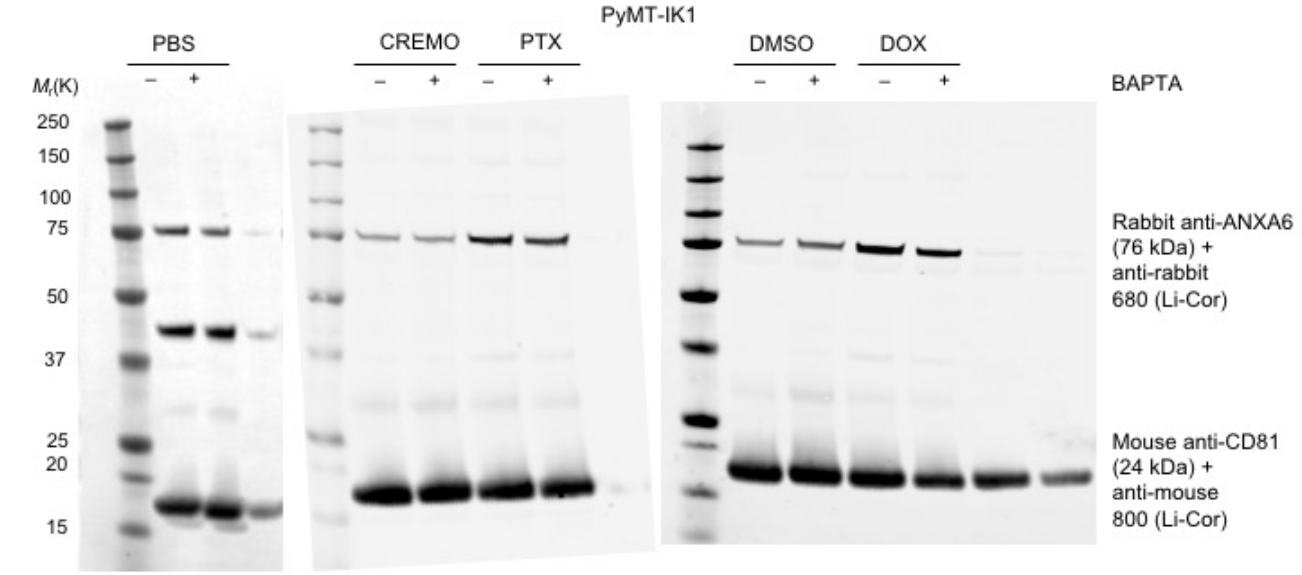

Supplementary Figure 9

Unprocessed blots (continued)

Figure 3h

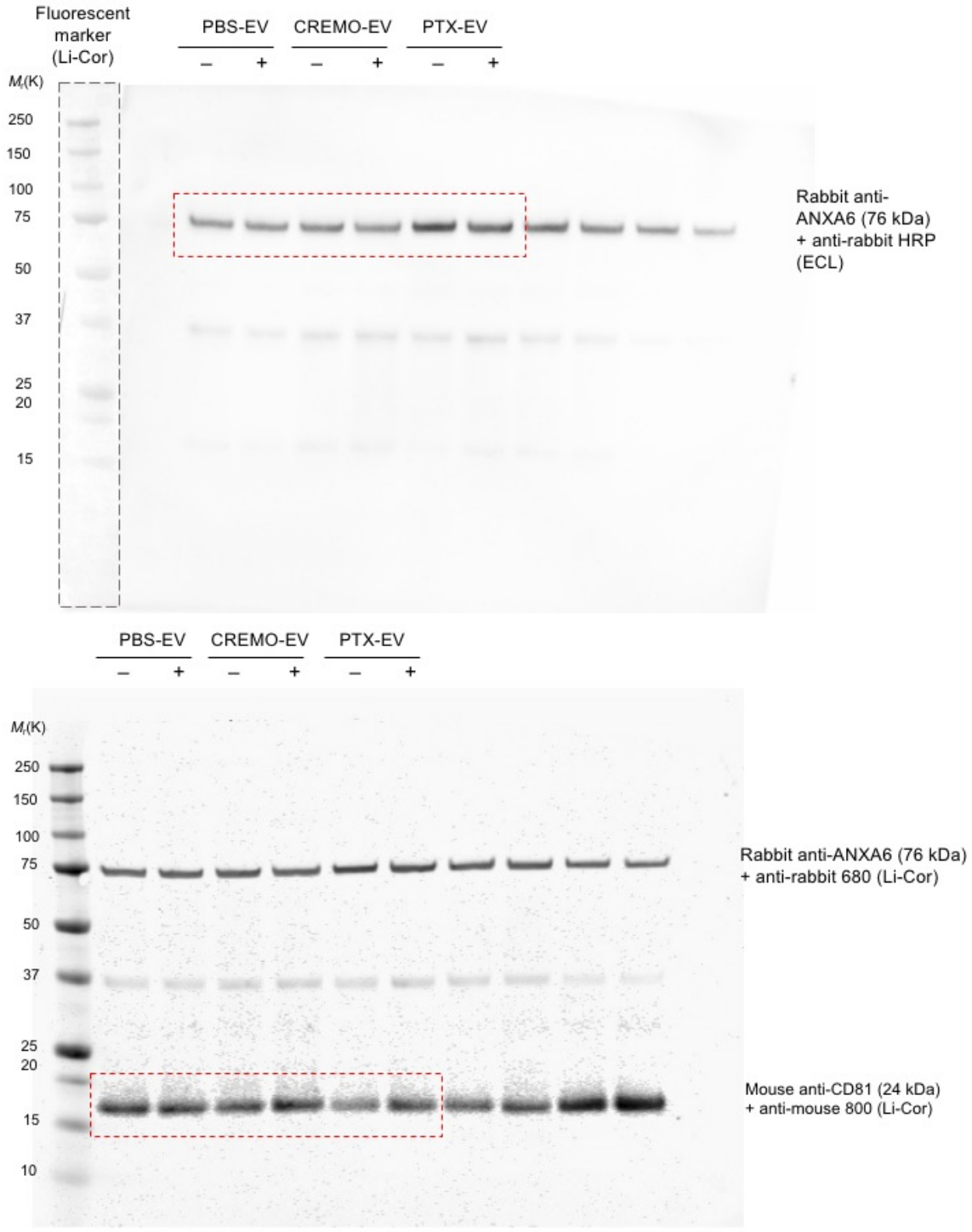

Supplementary Figure 9

Unprocessed blots (continued)

Repeat #2 associated to Fig. 3h (used for quantitative analysis, but not shown)

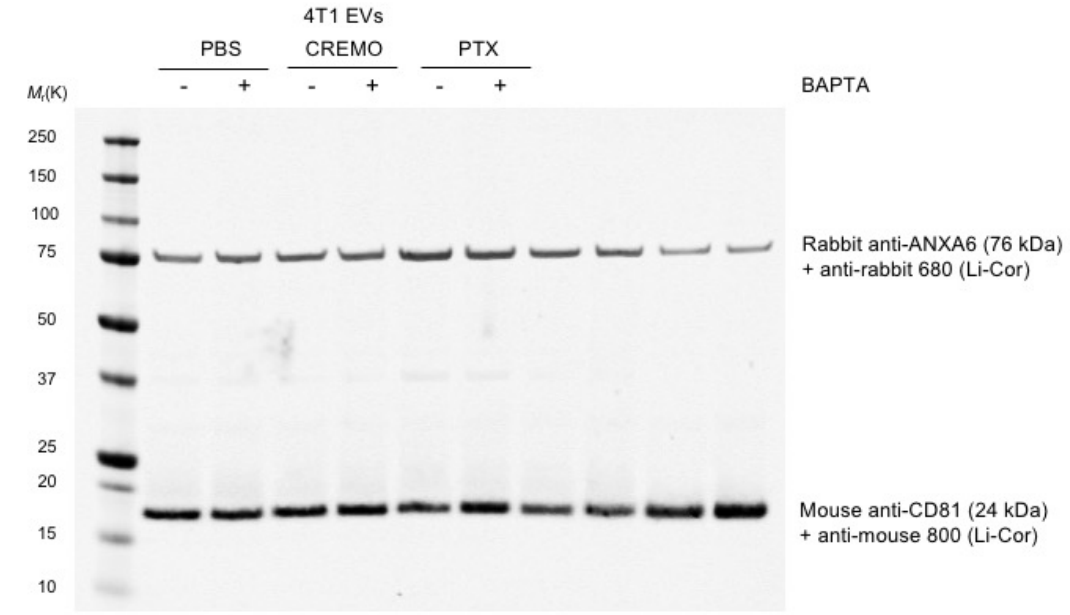

Repeat #3 associated to Fig. 3h (used for quantitative analysis, but not shown)

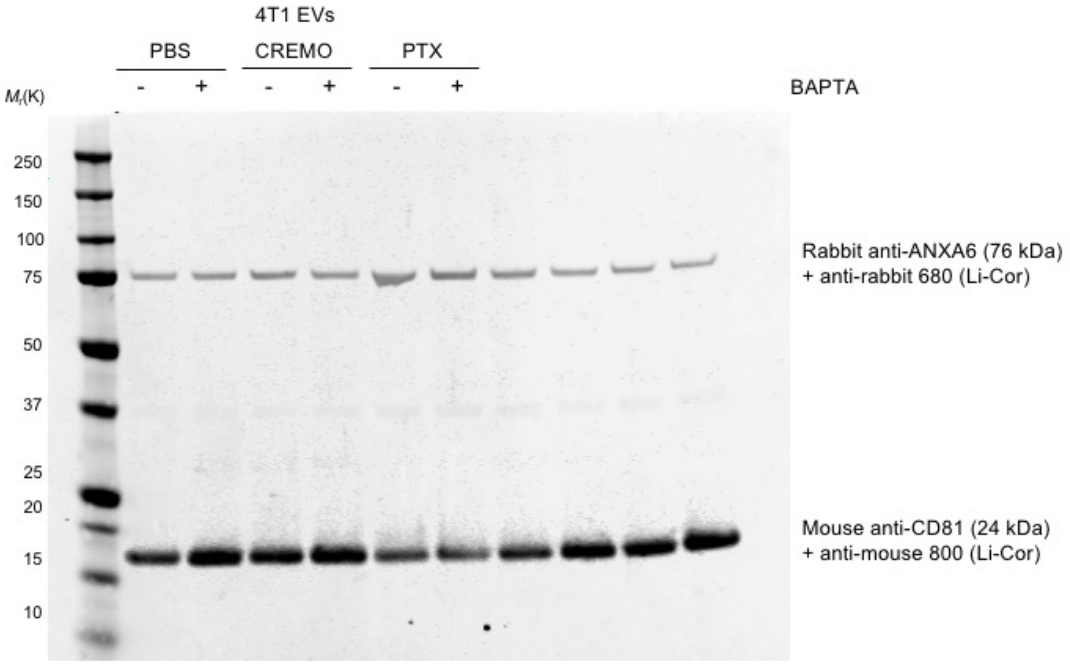

Supplementary Figure 9

Unprocessed blots (continued)

Figure 4b

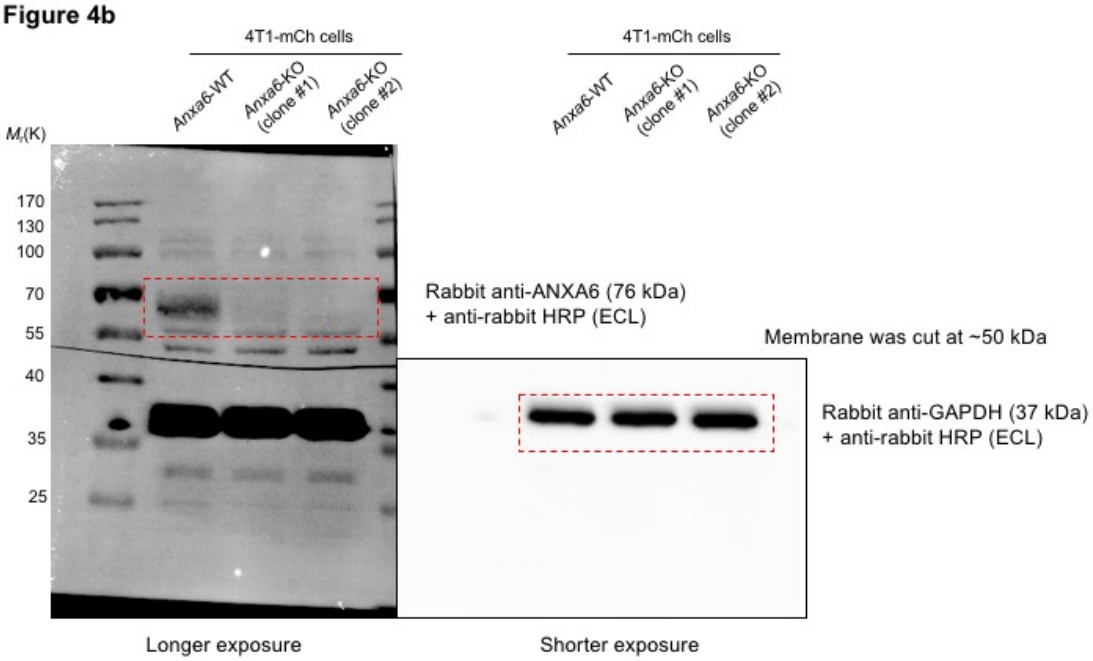

Figure 4c

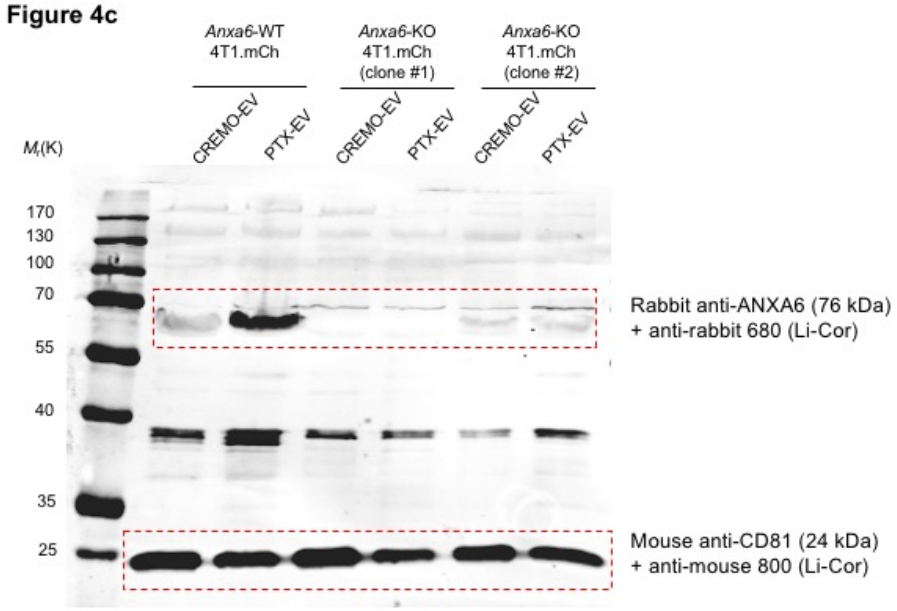

Supplementary Figure 9

Unprocessed blots (continued)

Figure 7d

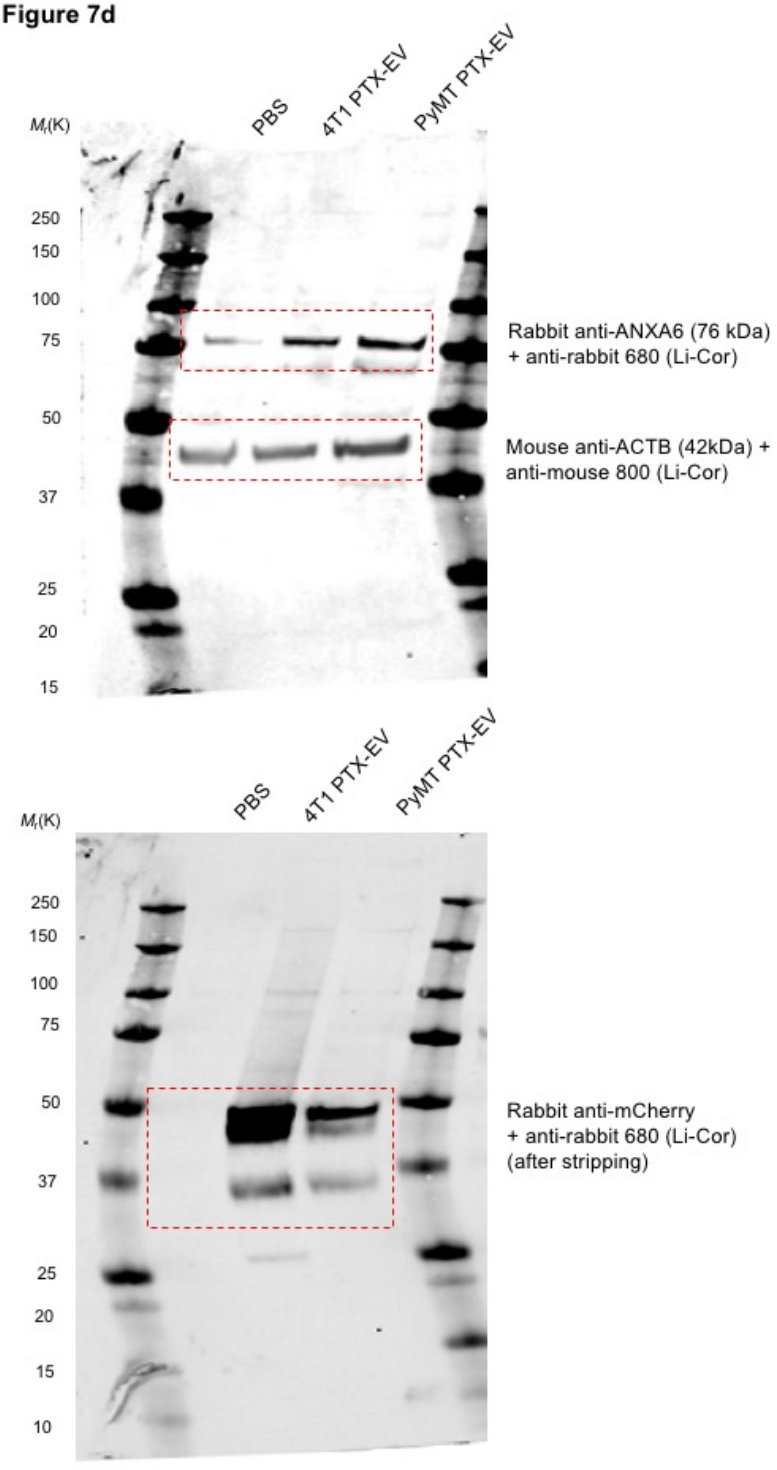

Supplementary Figure 9

Unprocessed blots (continued)

Figure 7f

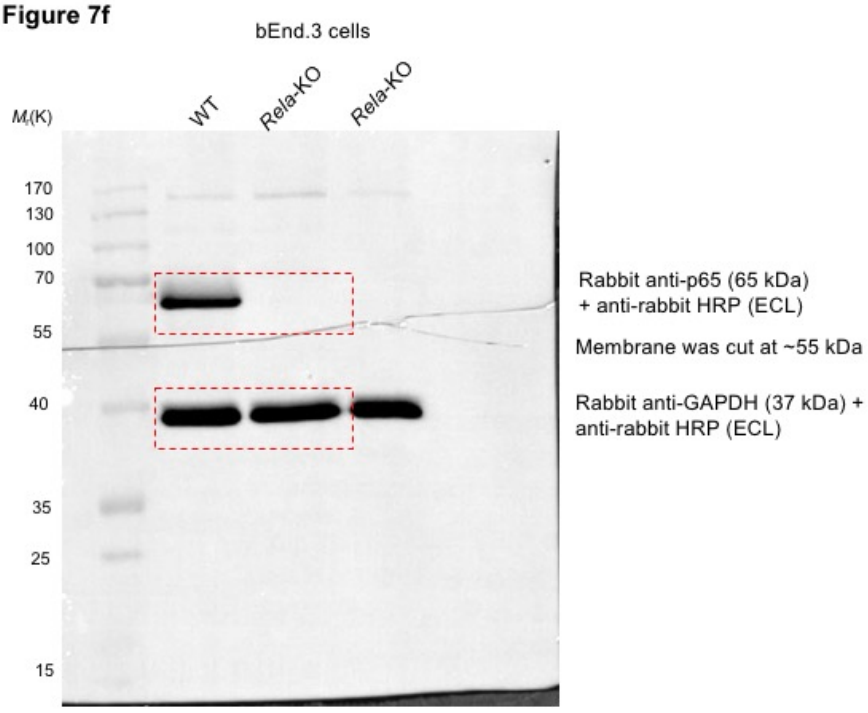

Figure 8a

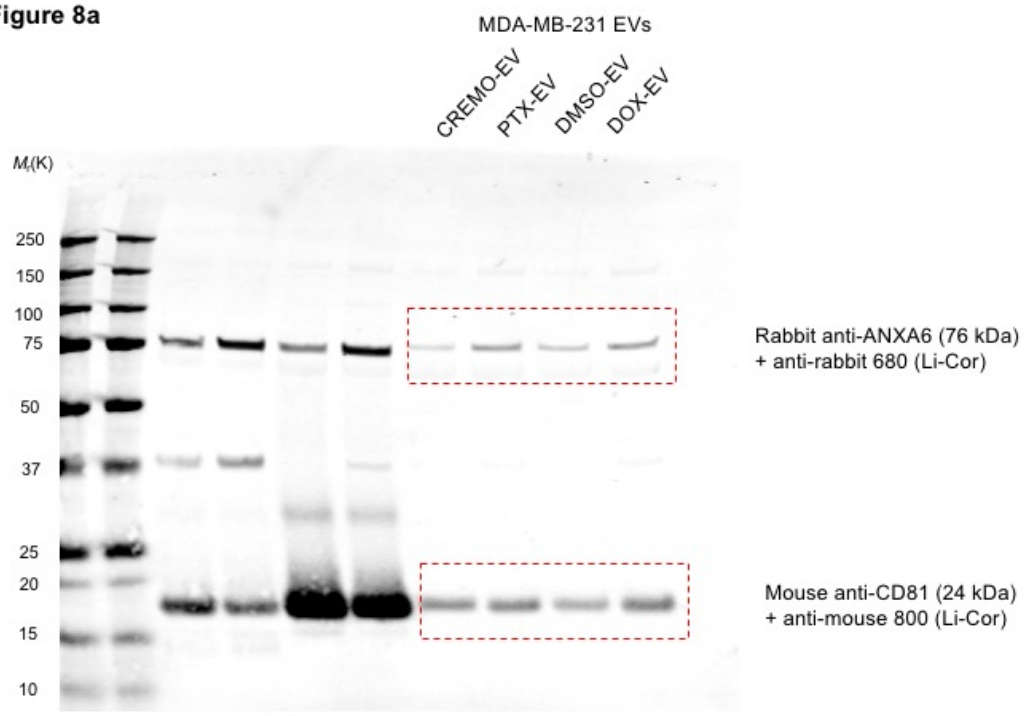

Supplementary Figure 9

Unprocessed blots (continued)

Repeat #2 associated to Figure 8a (not shown)

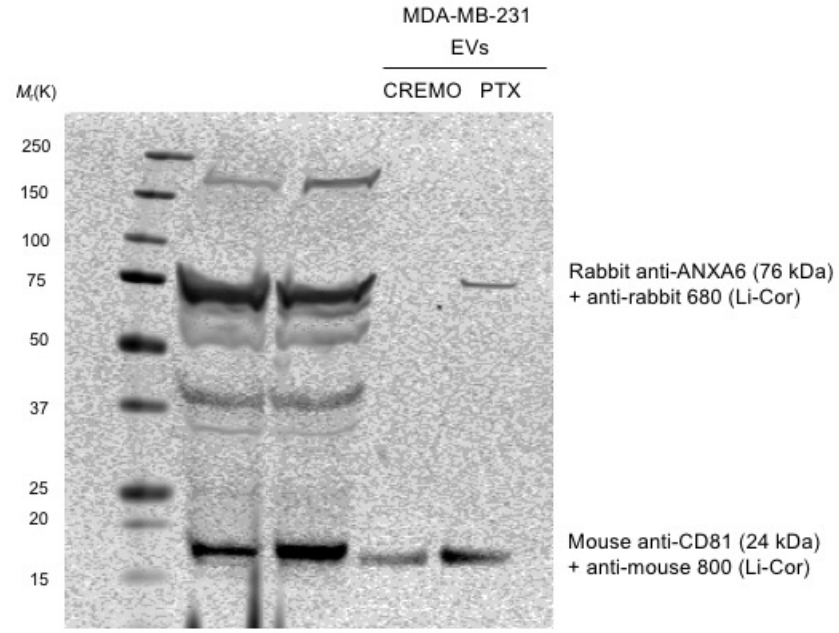

Repeat #3 associated to Figure 8a (not shown)

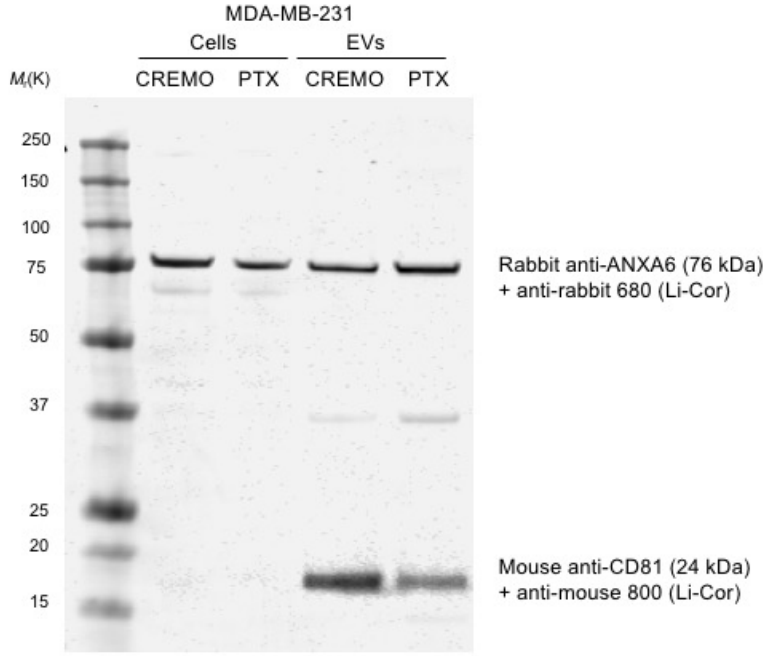

Supplementary Figure 9

Unprocessed blots (continued)

Figure 8d

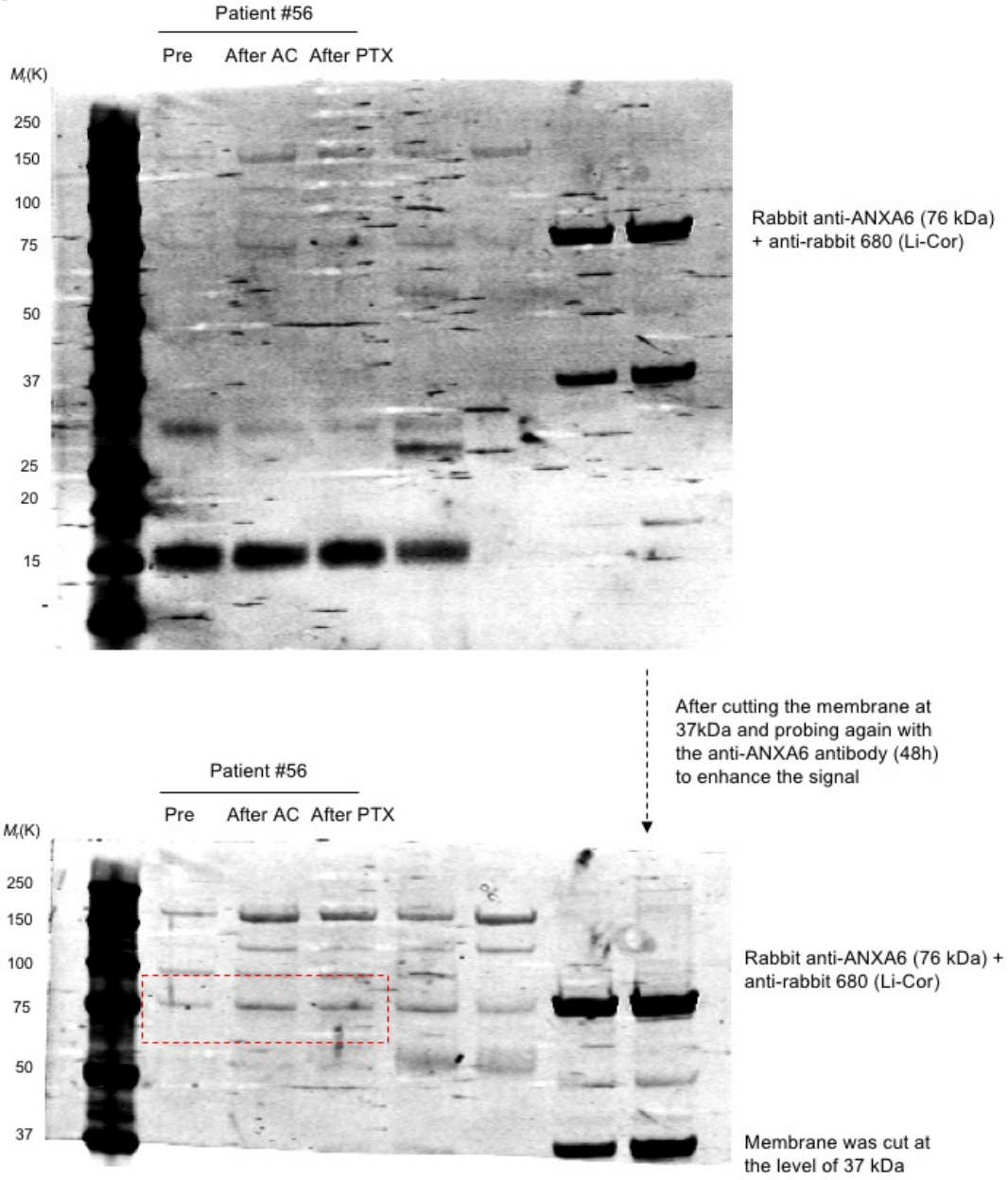

Supplementary Figure 9

Unprocessed blots (continued)

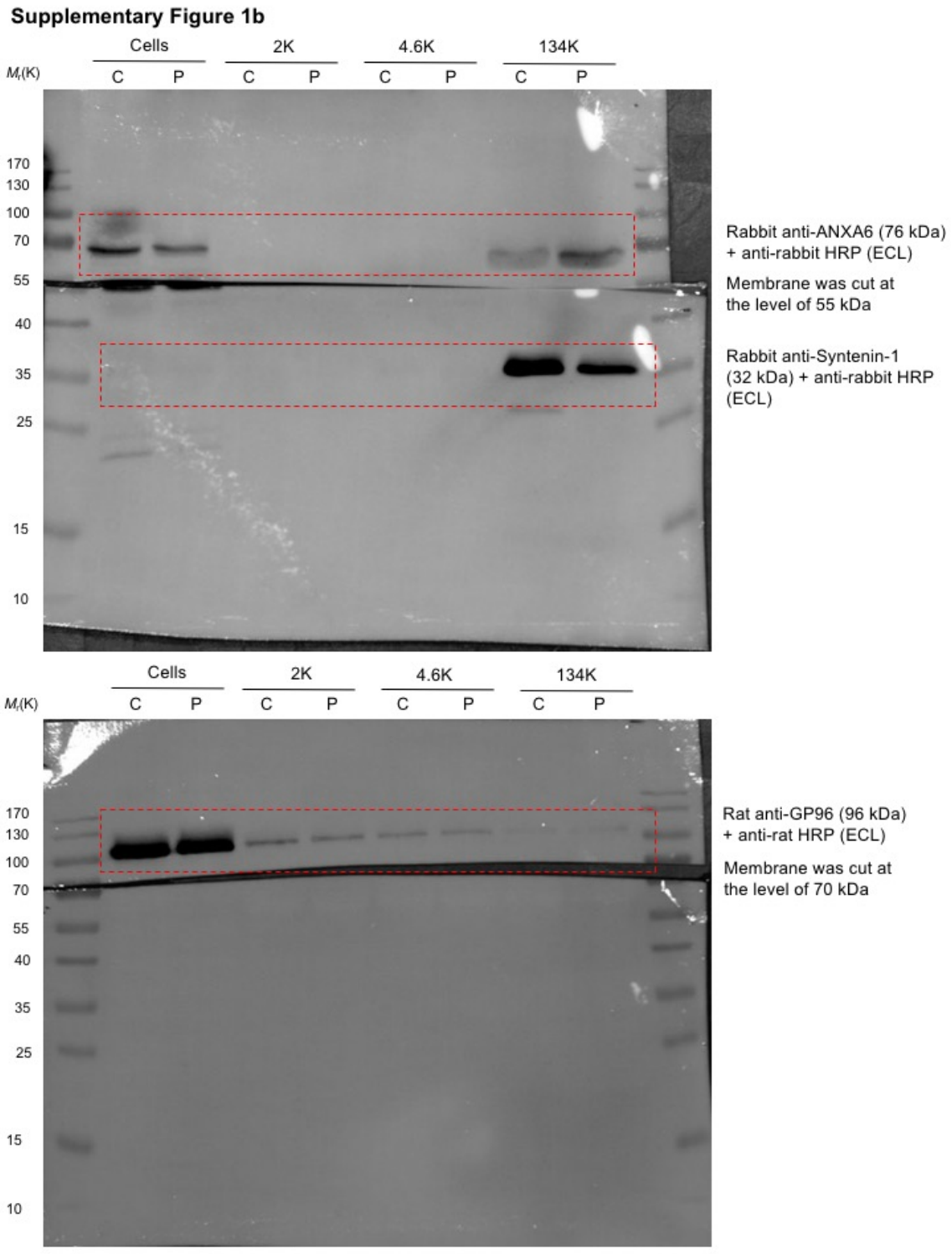

Supplementary Figure 9

Unprocessed blots (continued)

Supplementary Figure 1b

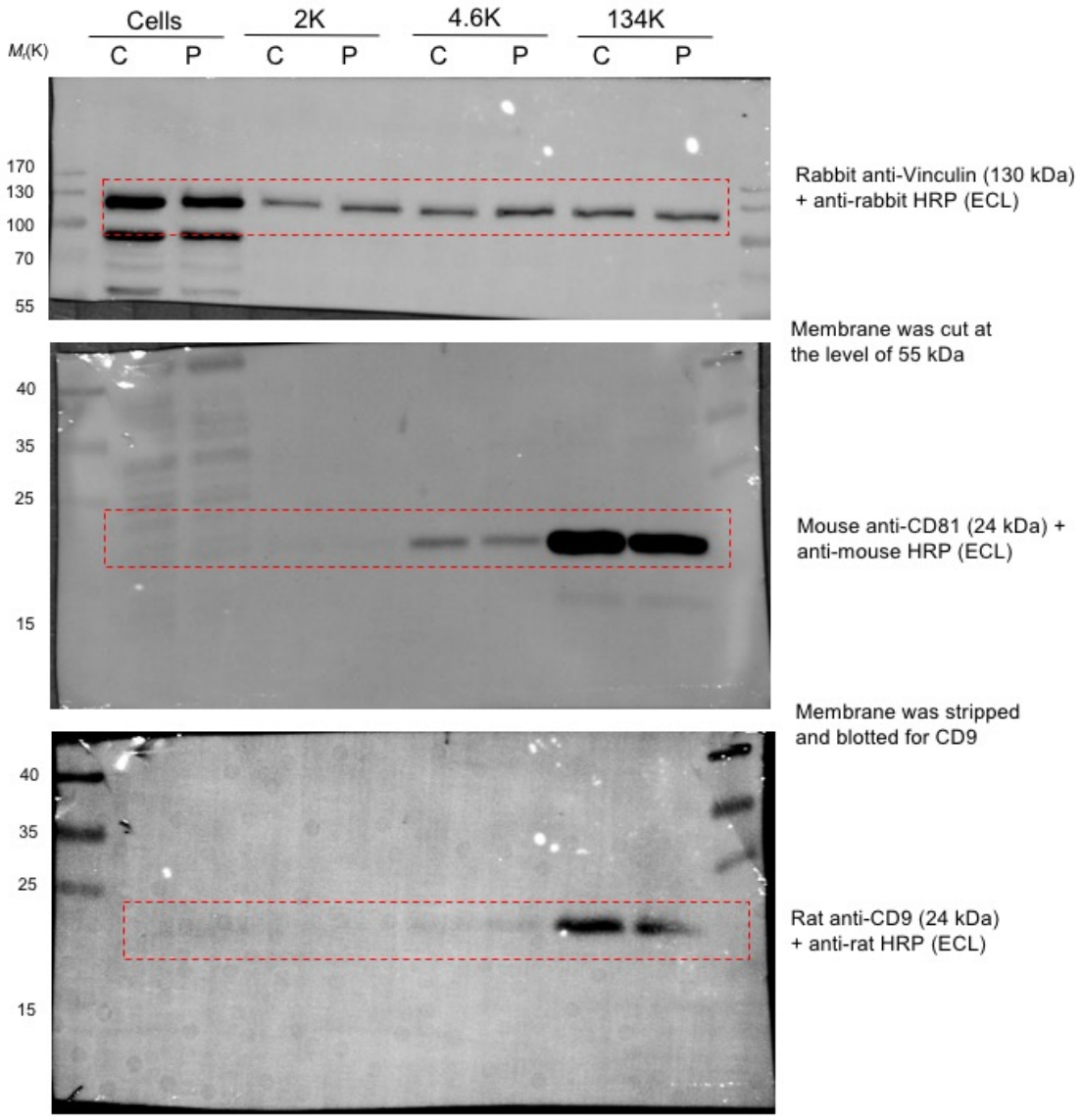

Supplementary Figure 9

Unprocessed blots (continued)

Supplementary Figure 1g

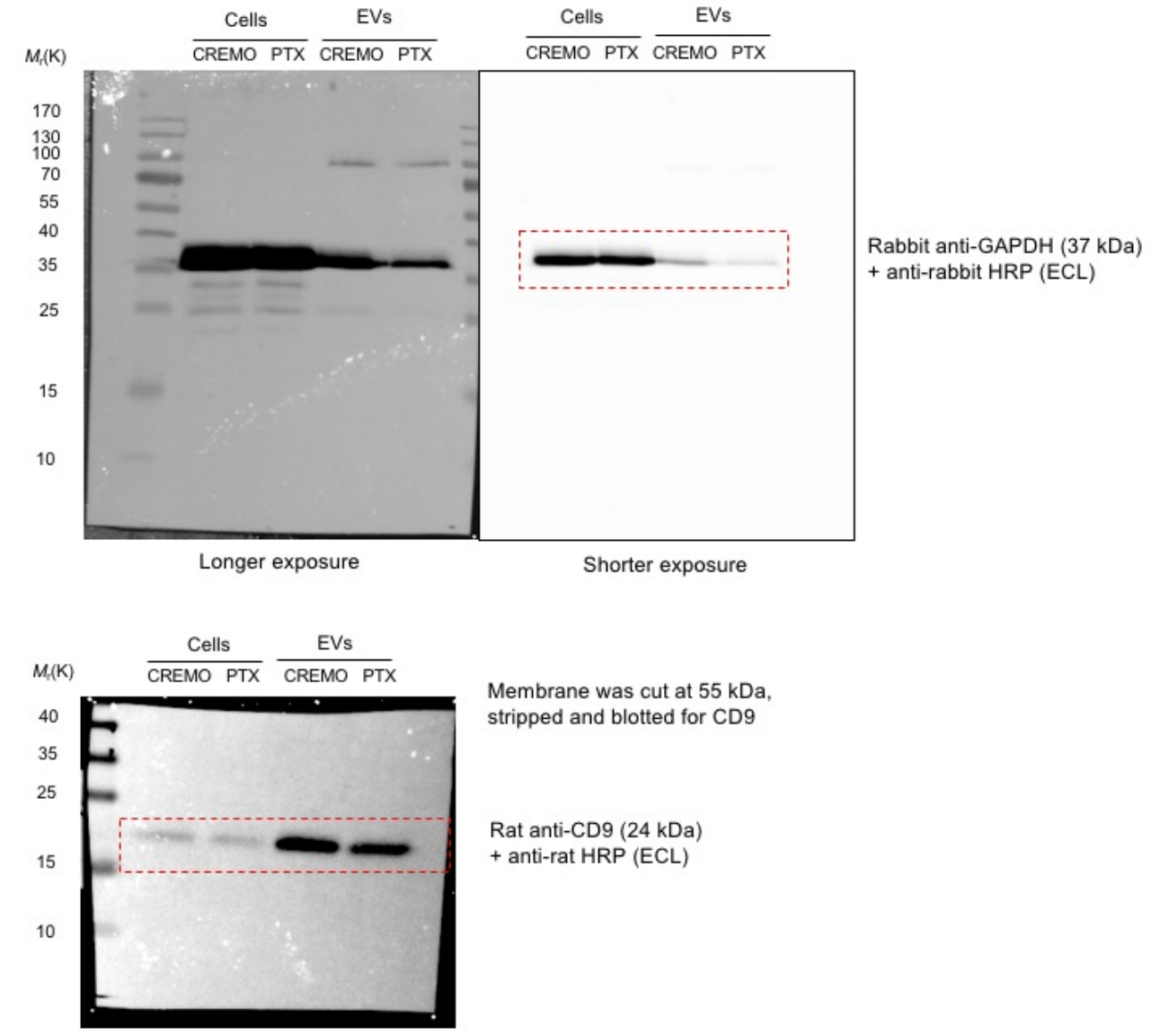

Supplementary Figure 9

Unprocessed blots (continued)

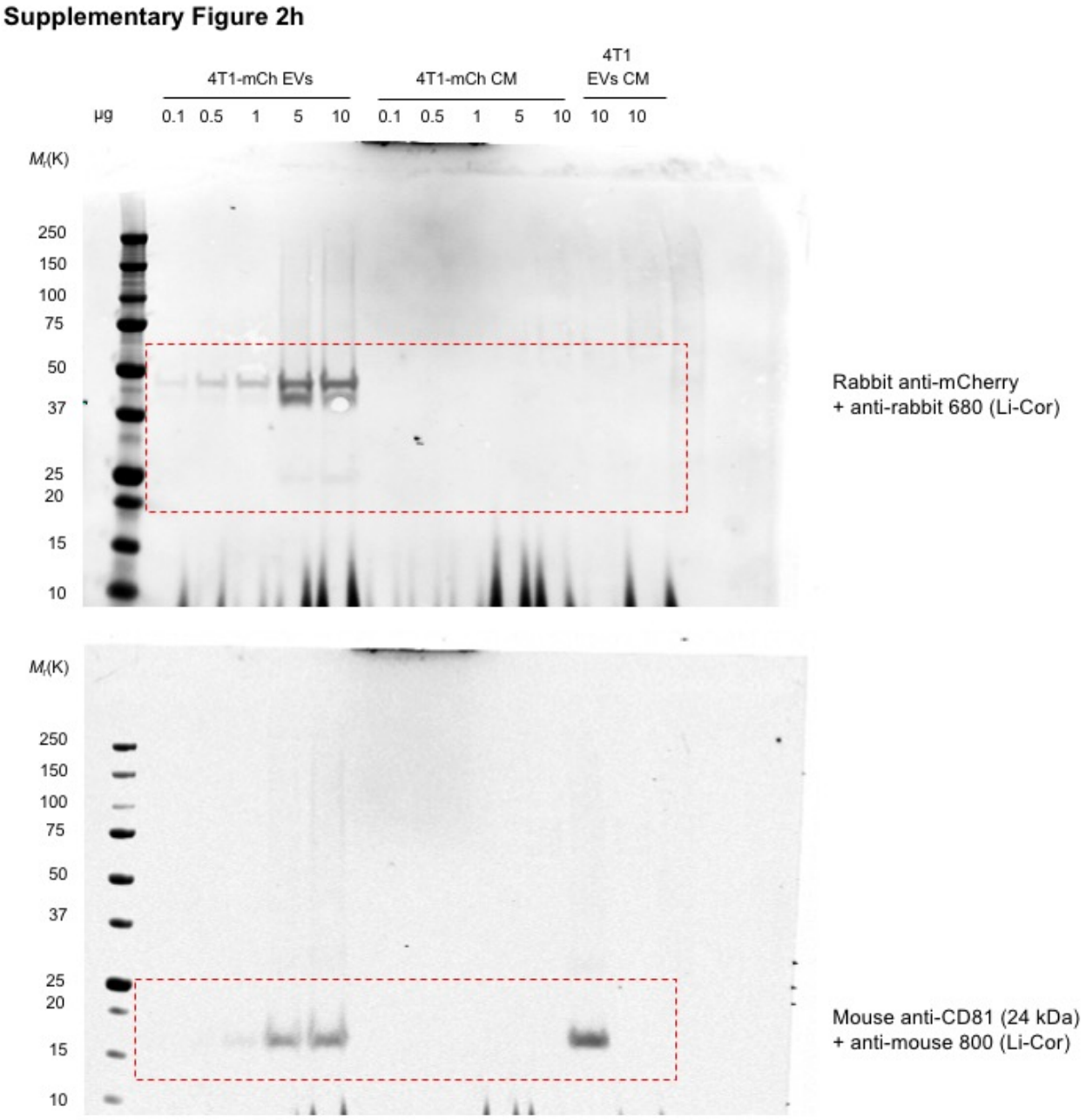

Supplementary Figure 9

Unprocessed blots (continued)

Supplementary Figure 2h

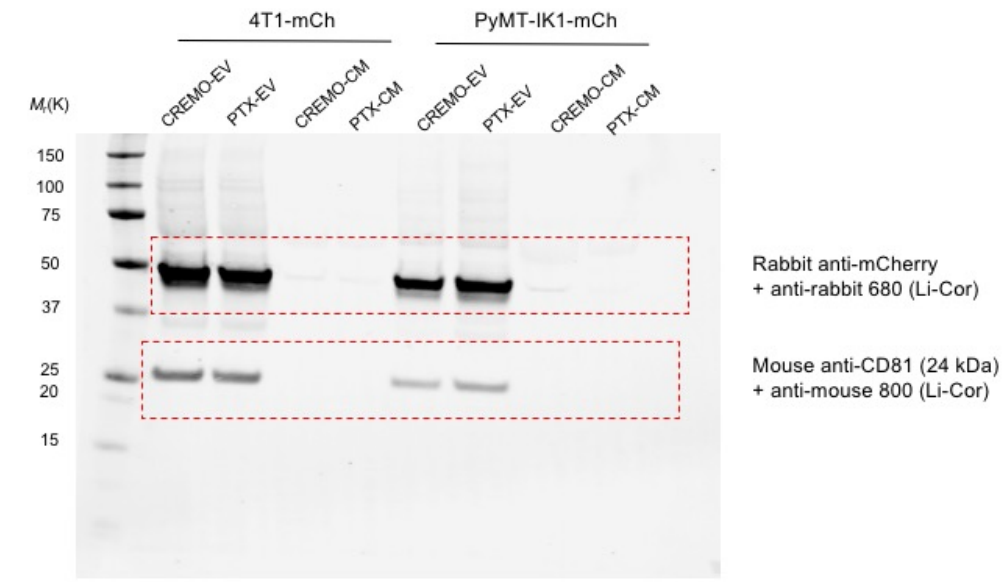

Supplementary Figure 3d

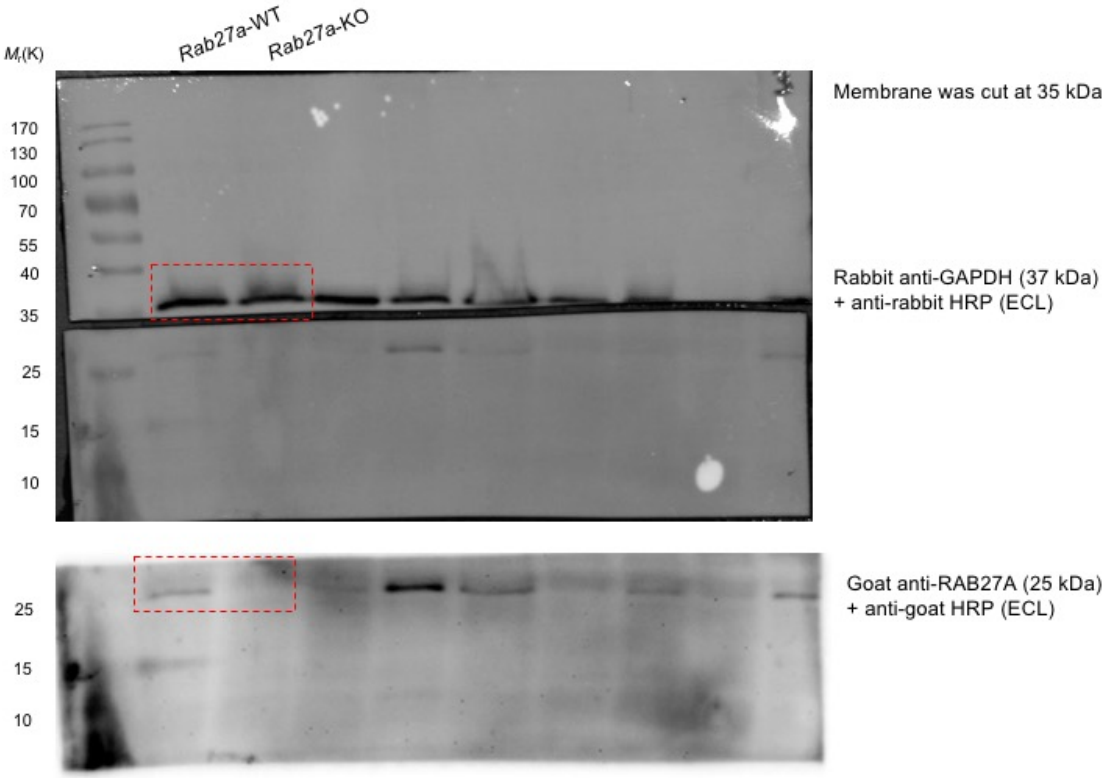

Supplementary Figure 9

Unprocessed blots (continued)

Supplementary Figure 4a

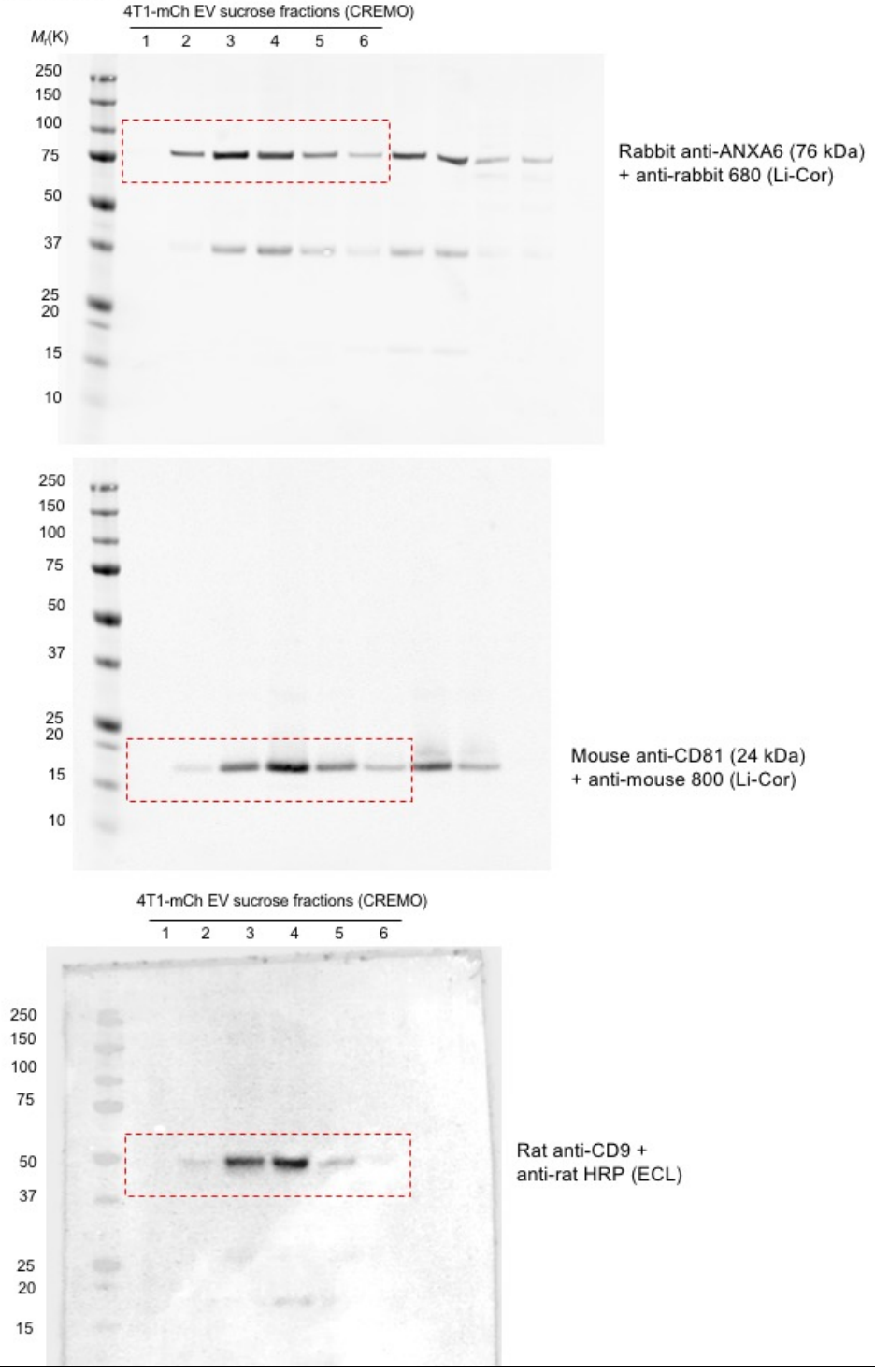

Supplementary Figure 9

Unprocessed blots (continued)

Supplementary Figure 4a

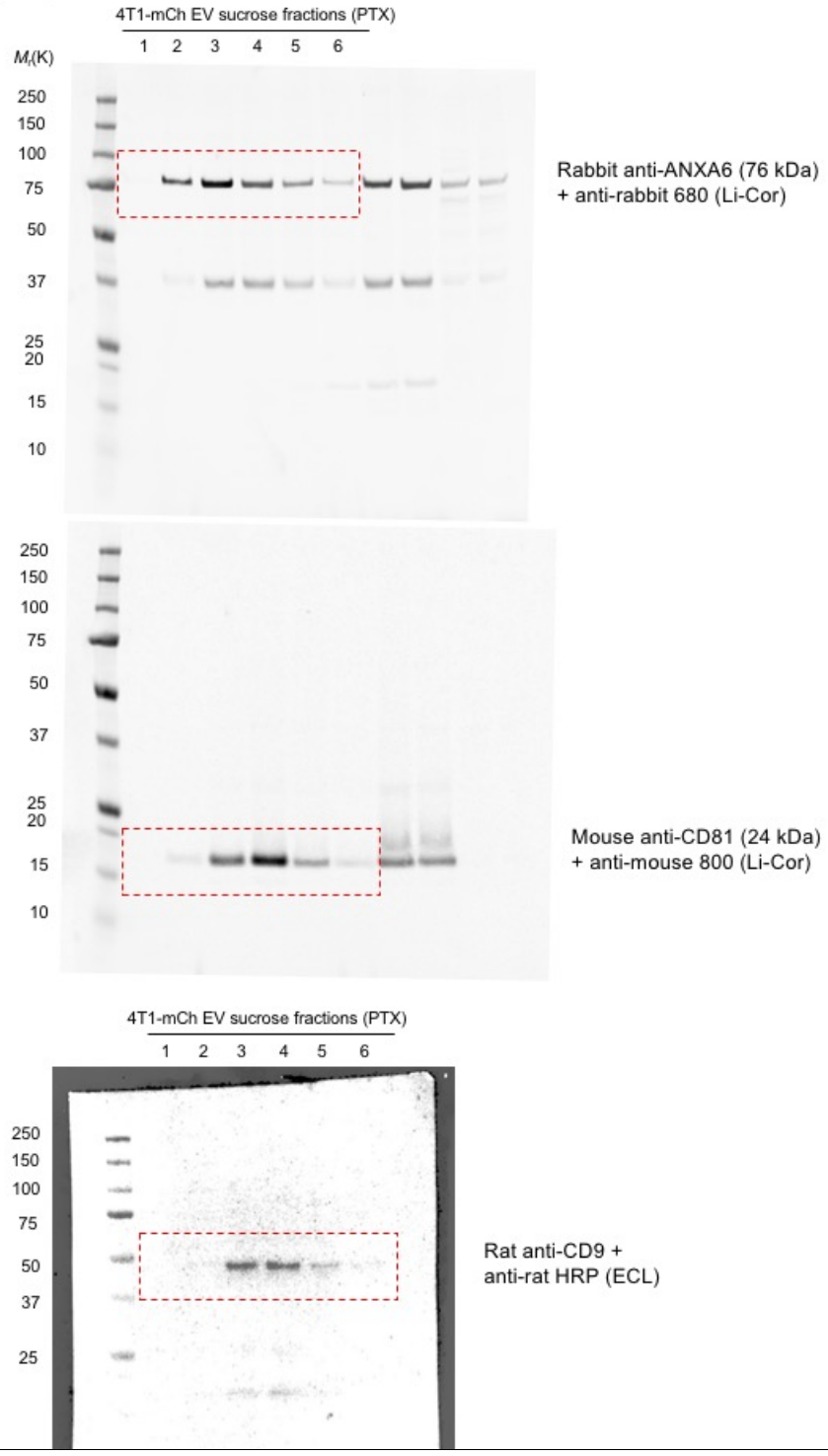

Supplementary Figure 9

Unprocessed blots (continued)

Repeat #2 associated to Supplementary Fig. 4a (used for quantitative analysis, but not shown)

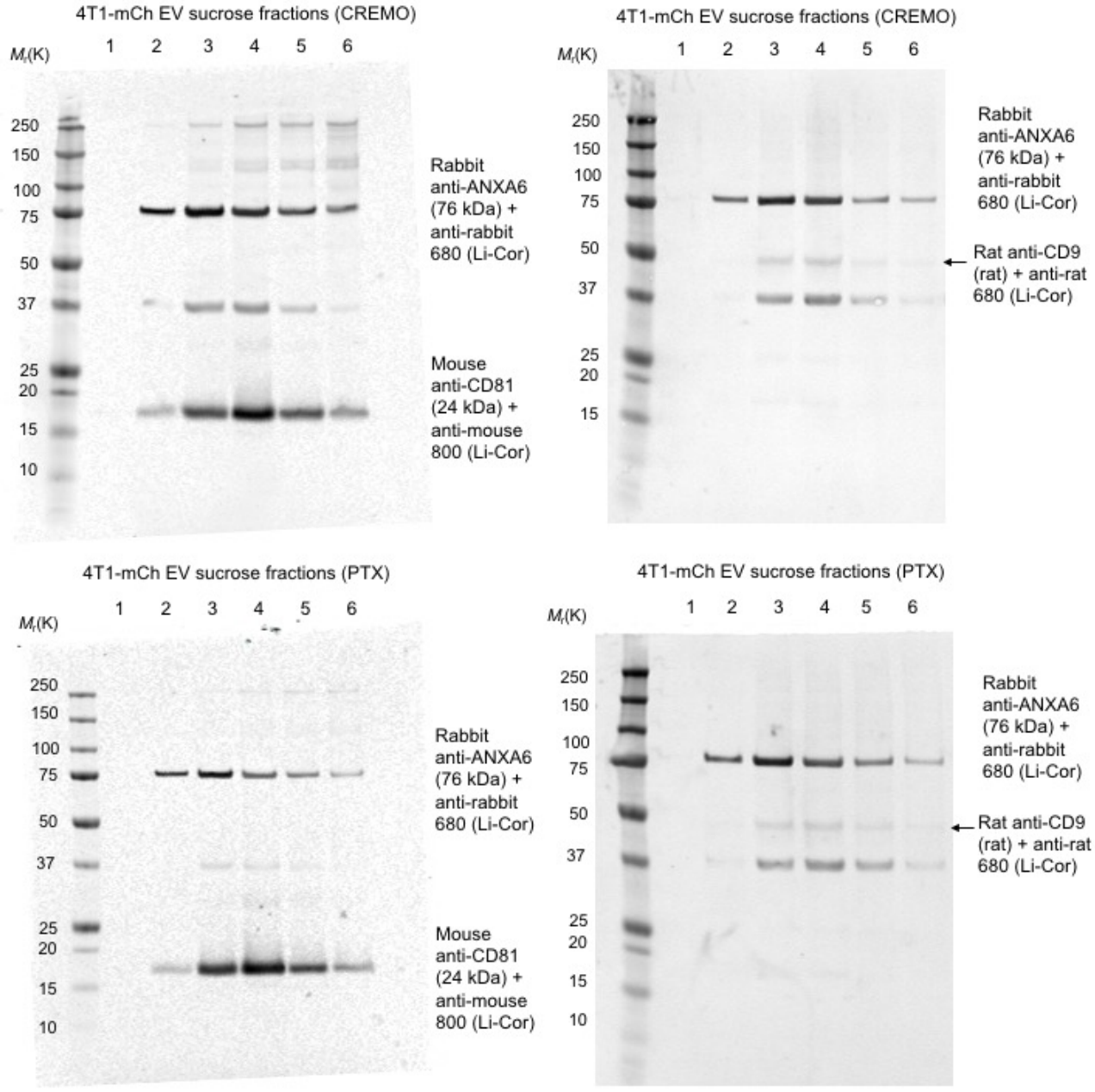

Supplementary Figure 9

Unprocessed blots (continued)

Supplementary Figure 4d

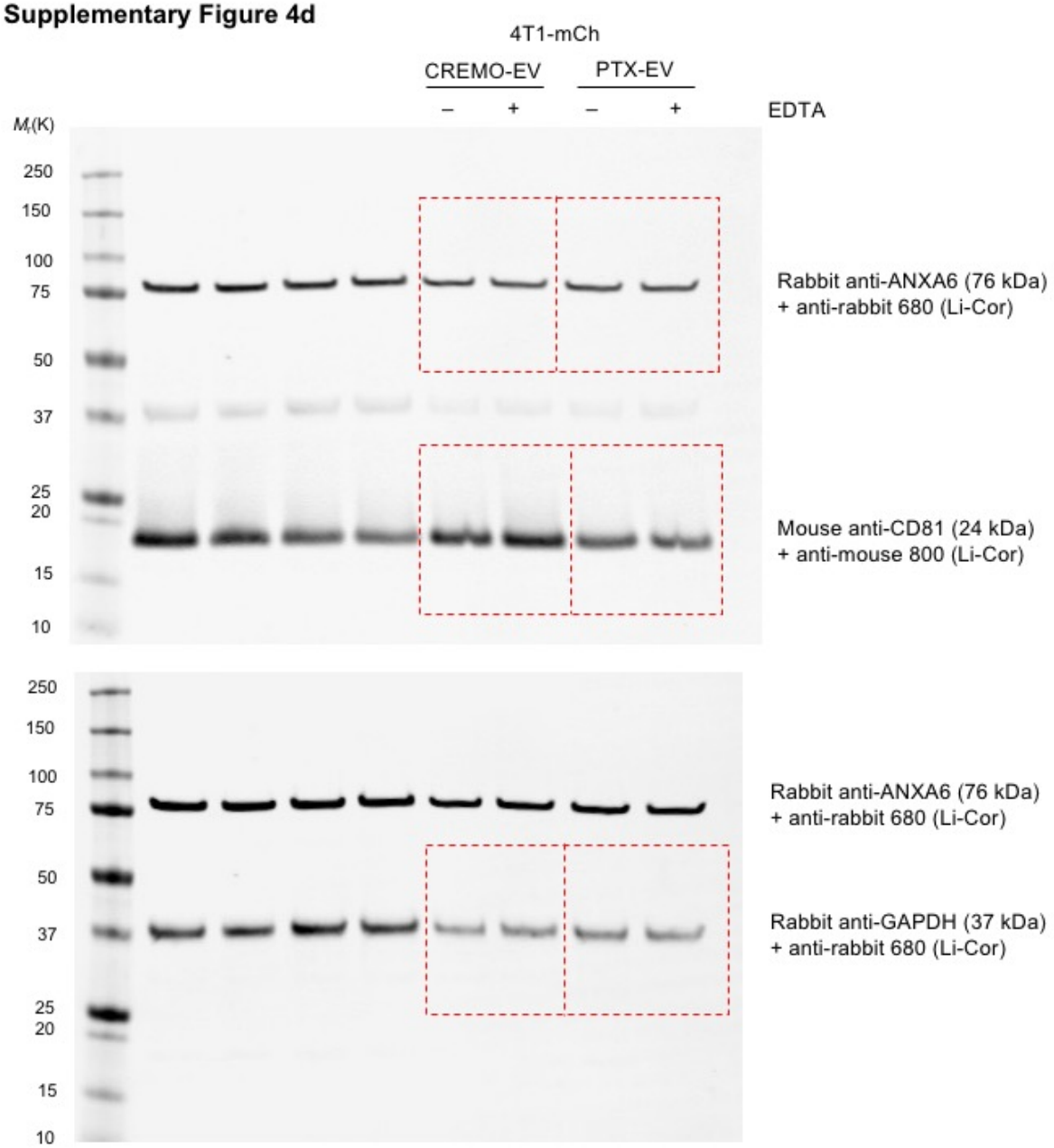

Supplementary Figure 9

Unprocessed blots (continued)

Repeat #2 associated to Supplementary Fig. 4d (not shown)

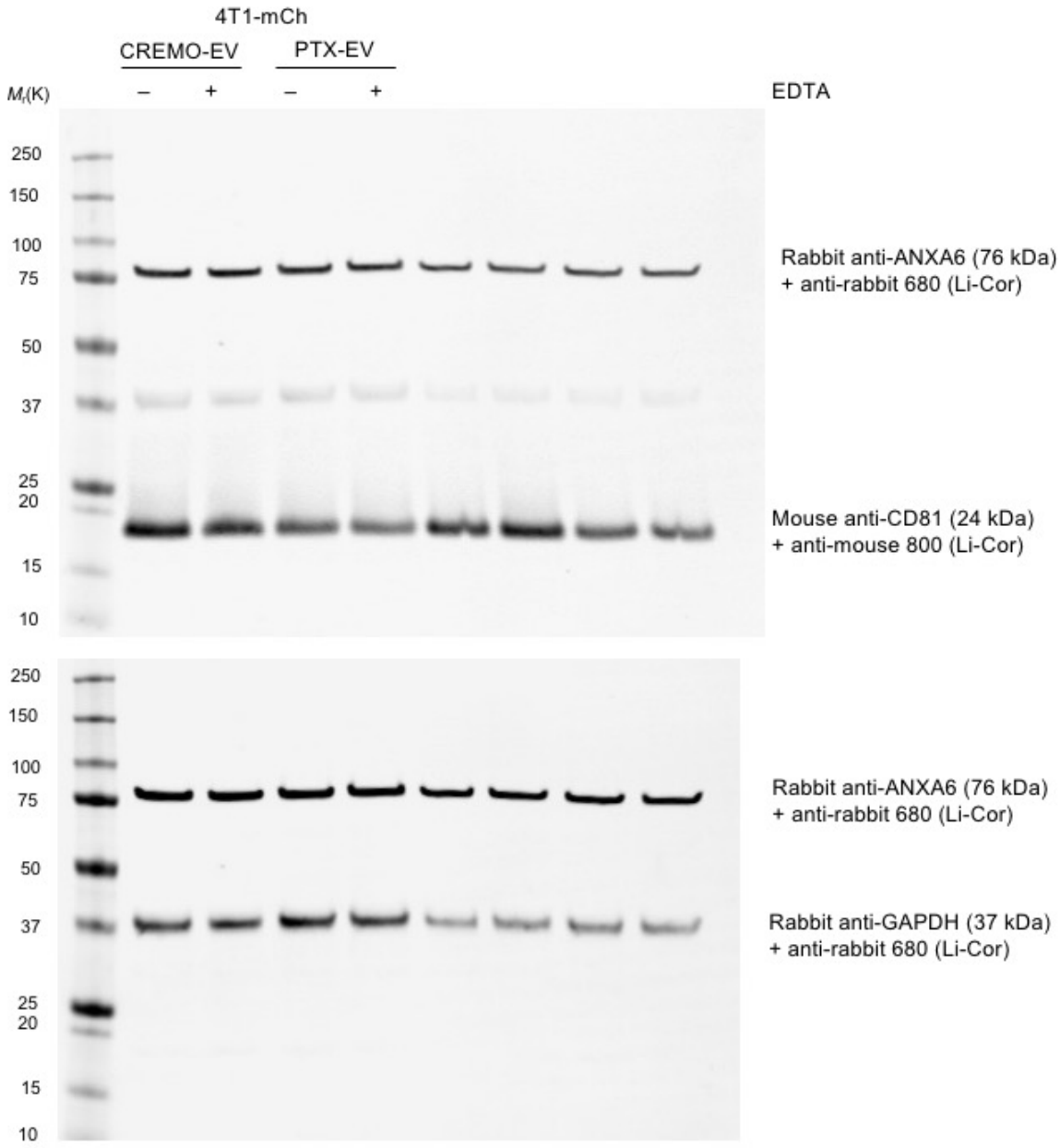

Supplementary Figure 9

Unprocessed blots (continued)

Repeat #3 associated to Supplementary Fig. 4d (not shown)

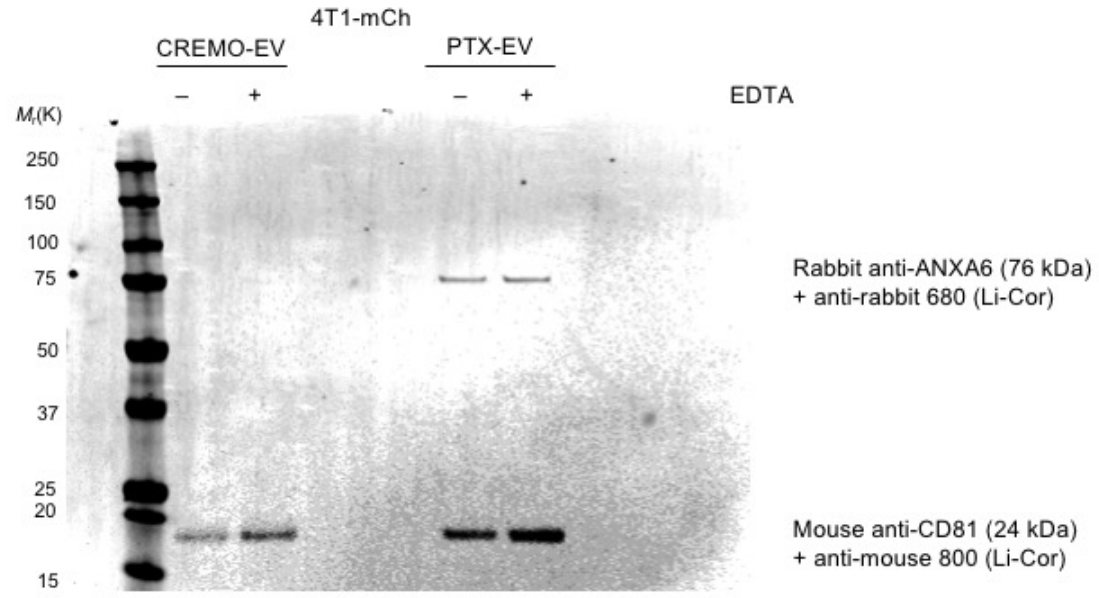

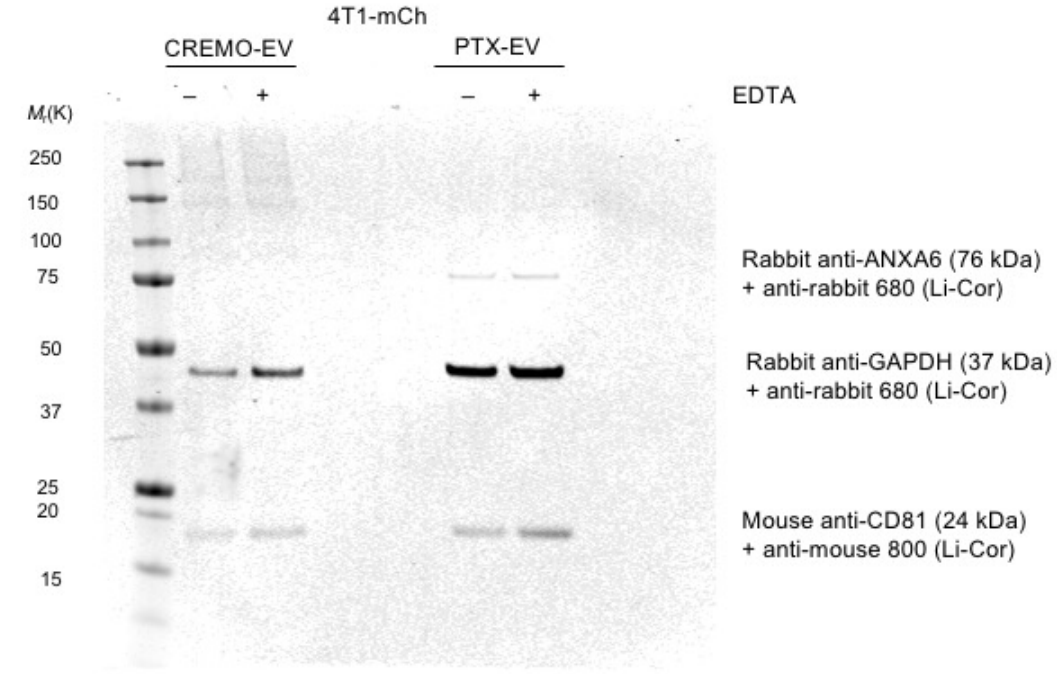

Supplementary Figure 9

Unprocessed blots (continued)

Supplementary Figure 4f

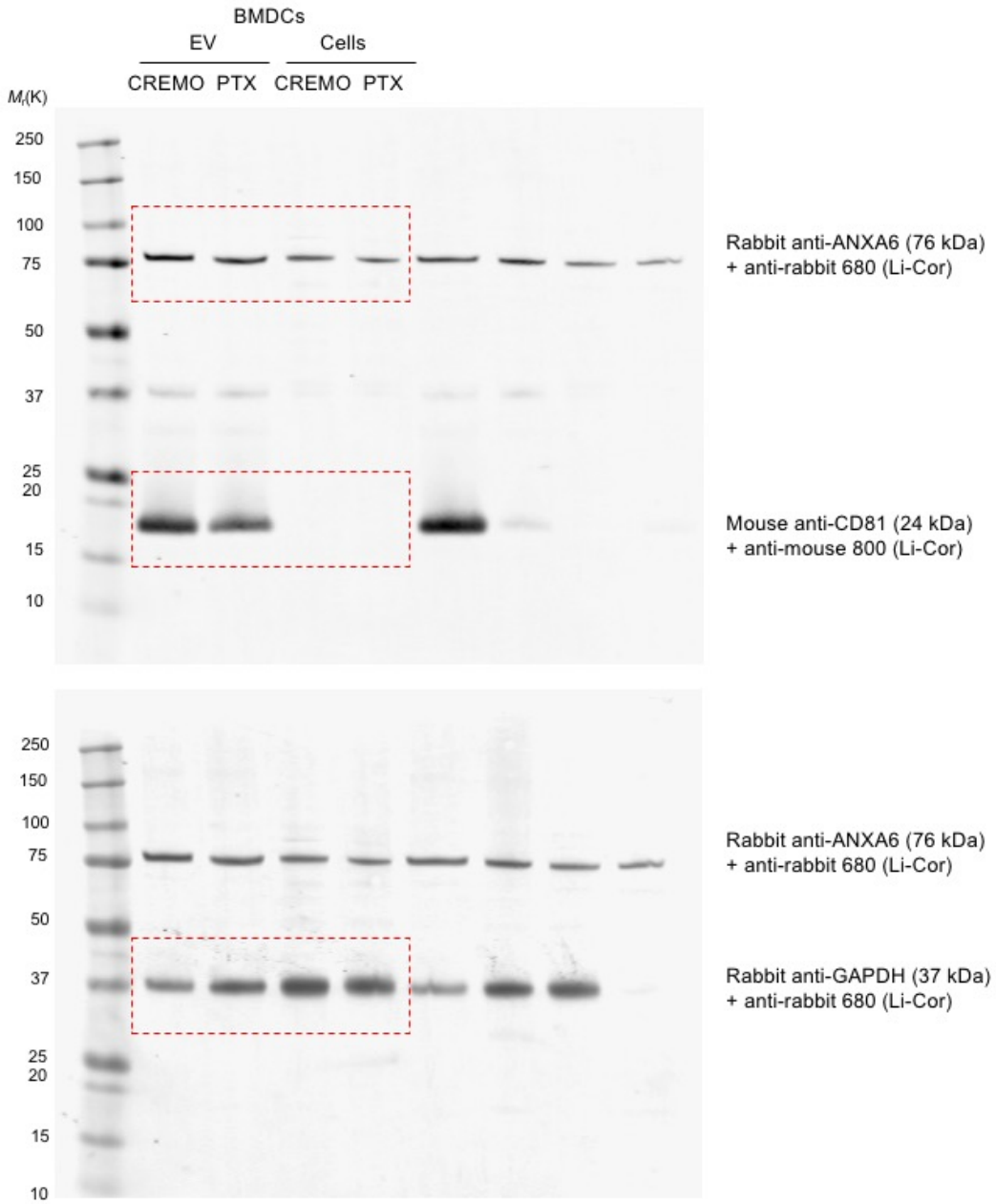

Supplementary Figure 9

Unprocessed blots (continued)

Supplementary Figure 4f

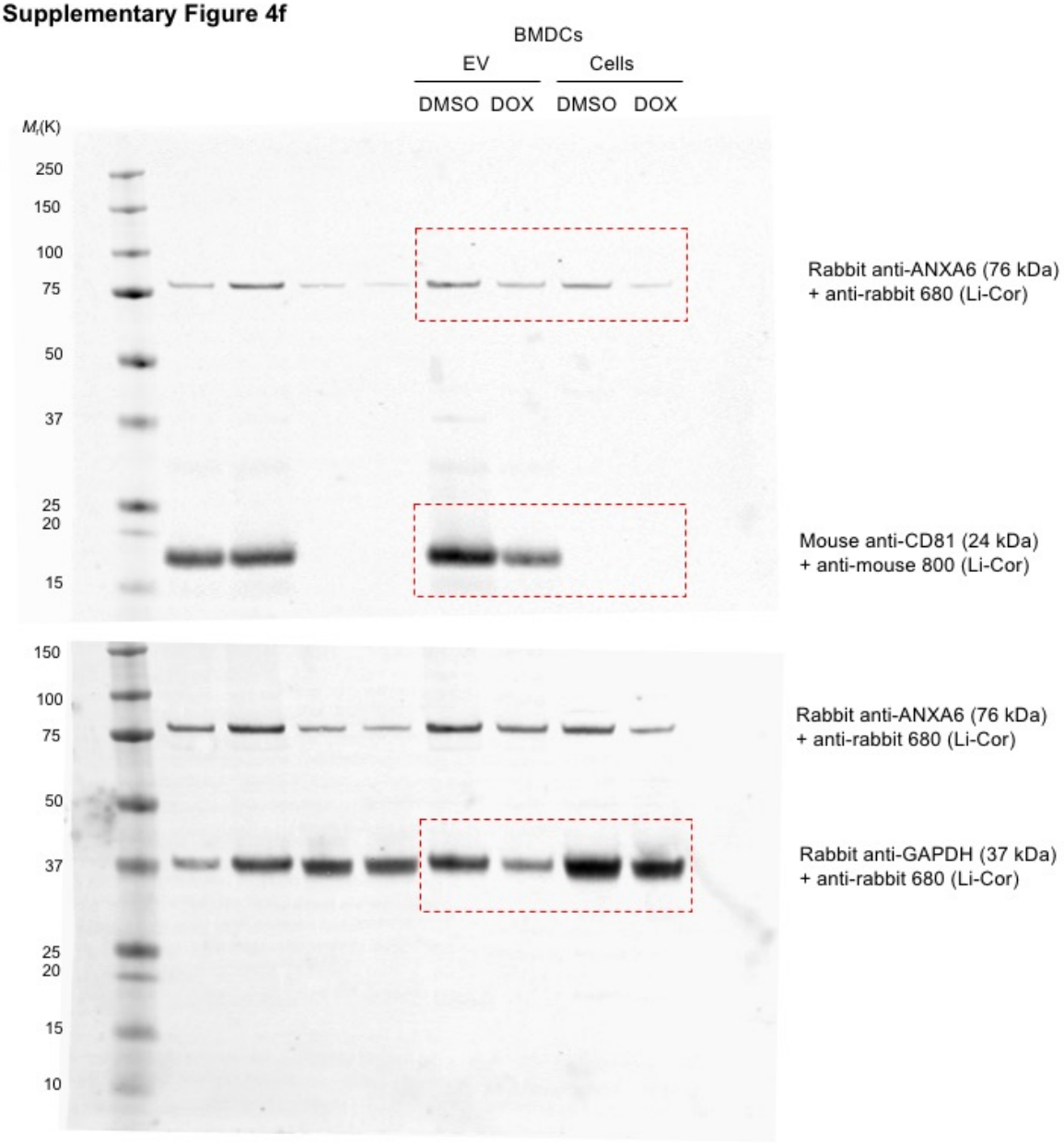

Supplementary Figure 9

Unprocessed blots (continued)

Repeat #2 associated to Supplementary Fig. 4f (not shown)

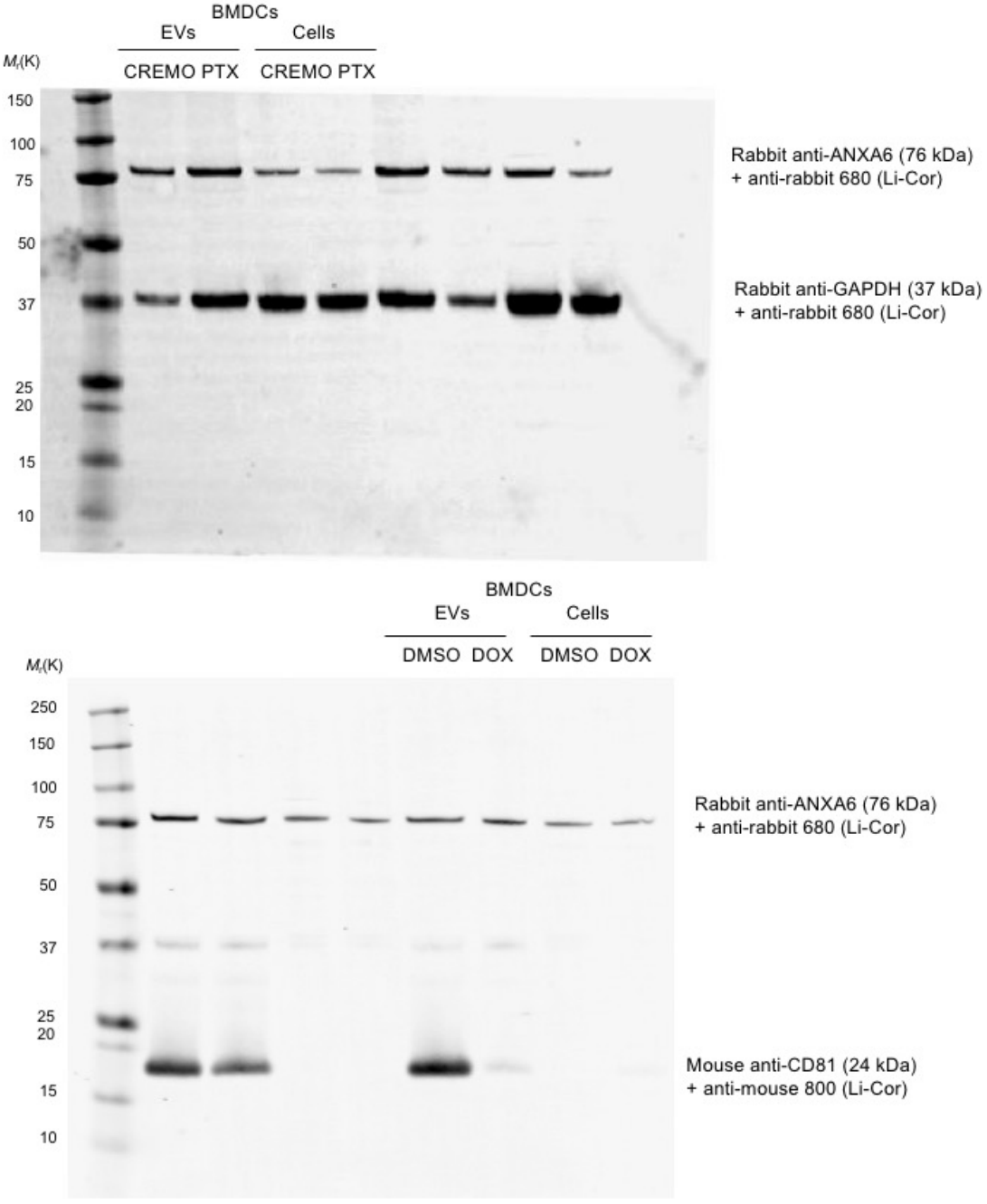

Supplementary Figure 9

Unprocessed blots (continued)

Supplementary Figure 4h

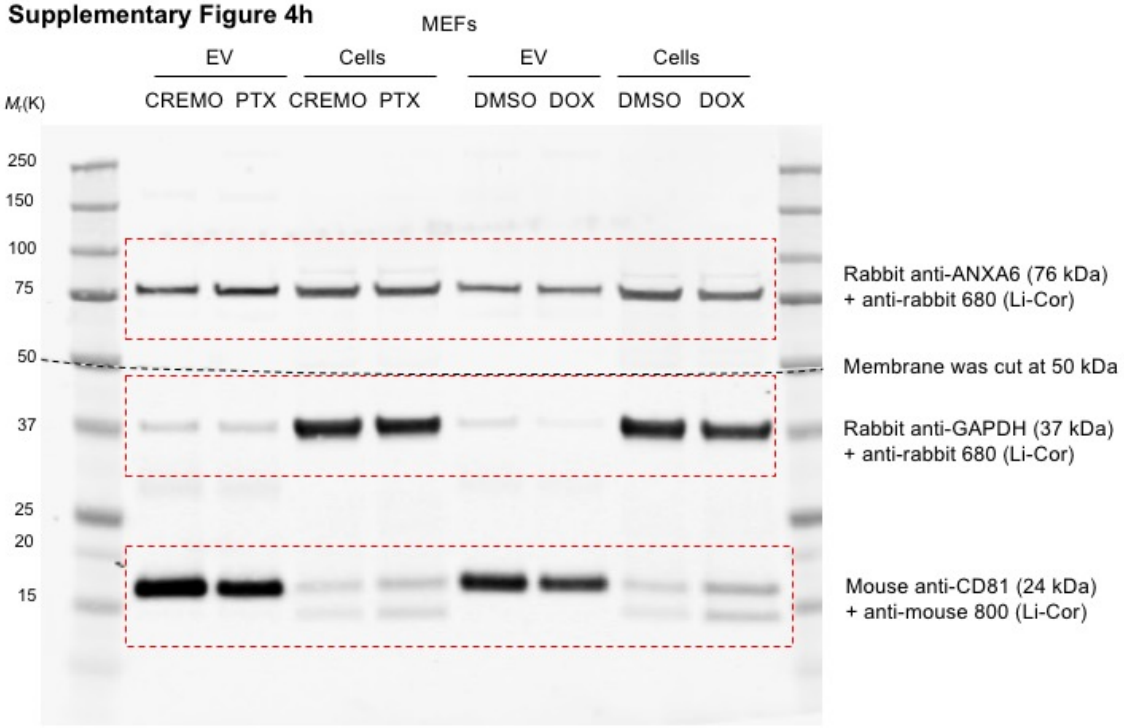

Supplementary Figure 4i

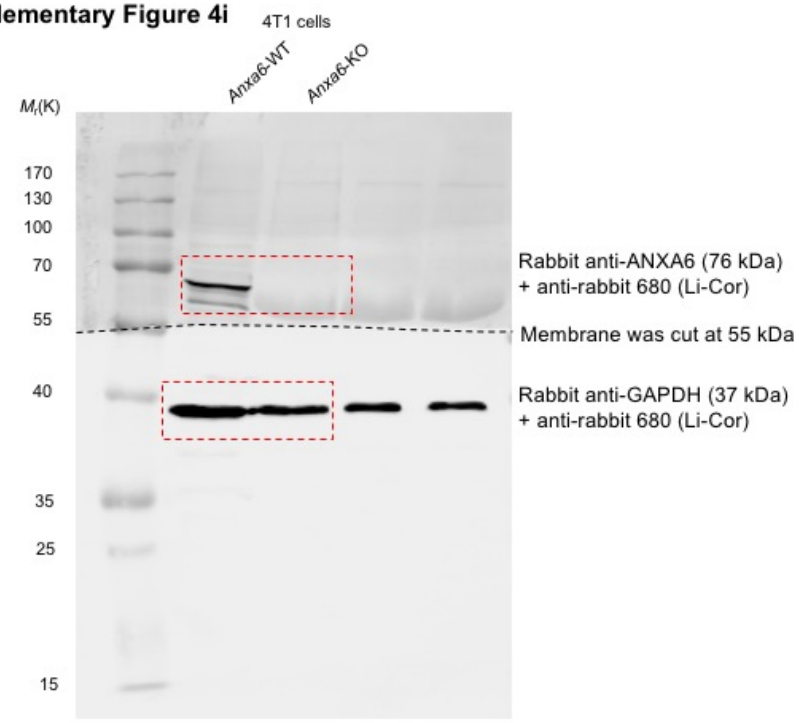

Supplementary Figure 9

Unprocessed blots (continued)

Supplementary Figure 6a

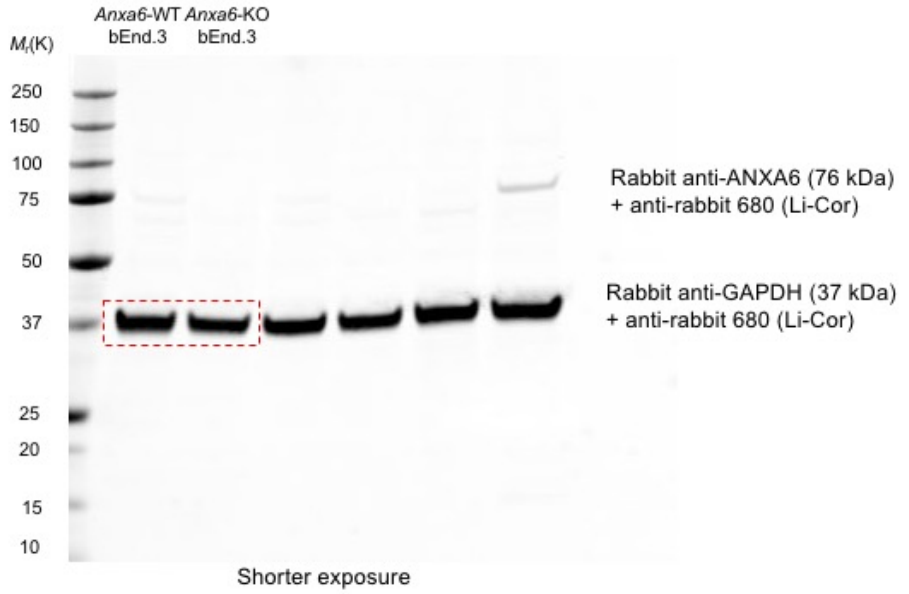

Shorter exposure

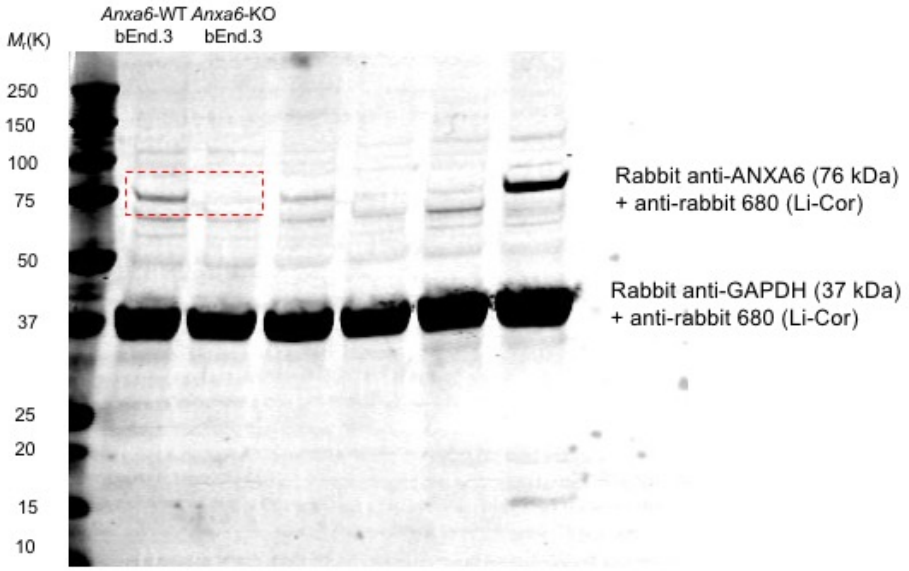

Longer exposure

Supplementary Figure 9

Unprocessed blots (continued)

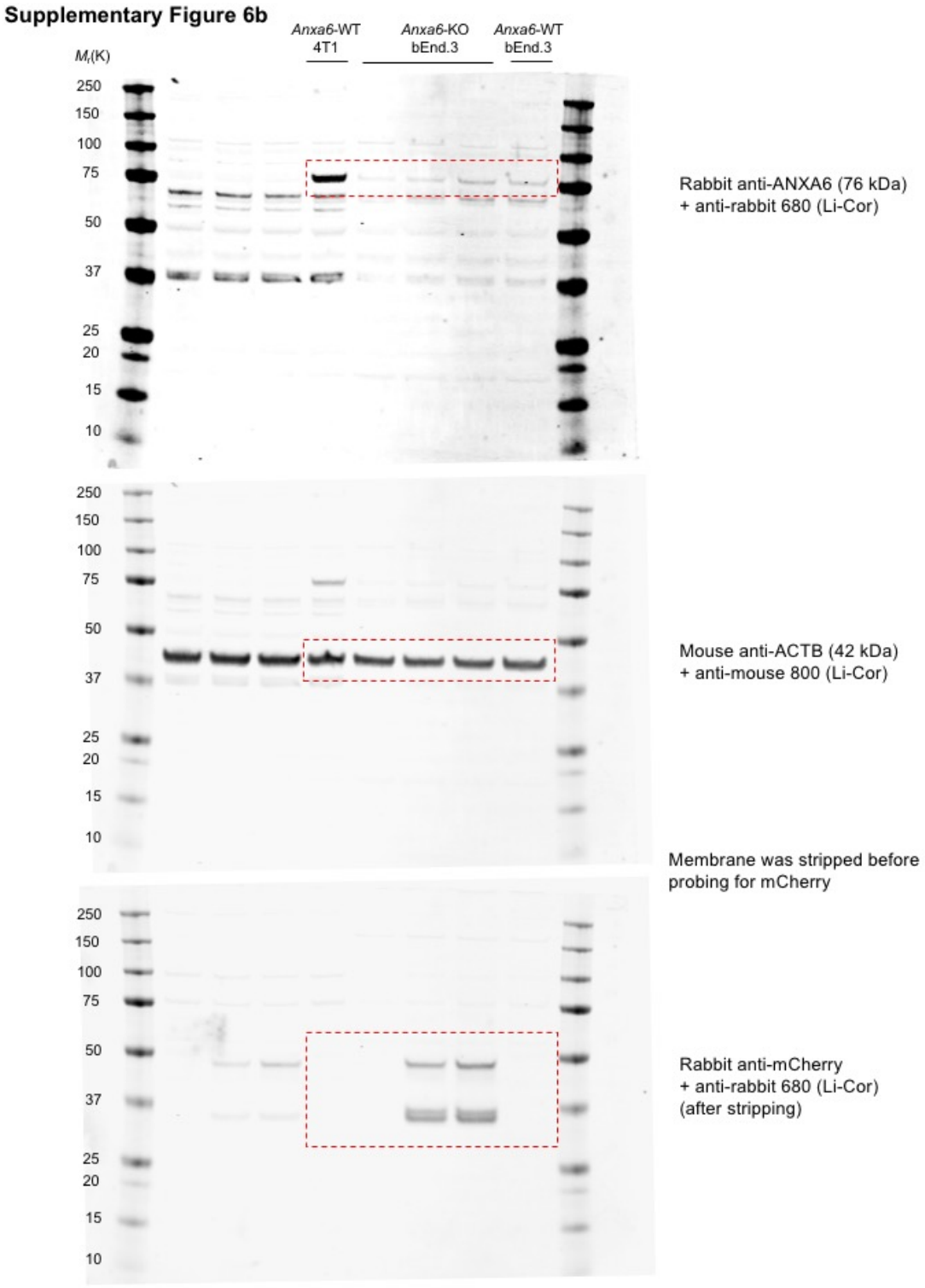

Supplementary Figure 9

Unprocessed blots (continued)

Supplementary Table 1
Protein quantification in CREMO-EV and PTX-EV (n=6 independent EV preparations per condition) isolated from 4T1 cells, determined by LC-MS/MS analysis
The table shows number of peptides per protein (minimum number: 4). Statistical analysis by unpaired two-tailed t-test; p-values adjusted after correcting for a false discovery rate using a Benjamini-Hochberg method.

Supplementary Table 2
Medical record of breast cancer patients
The table shows clinical data for the patients whose EVs were analysed in the study.

Supplementary Table 3
LC-MS/MS analysis of EVs in the plasma of breast cancer patients
The table shows time schedule of each blood collection and associated LC-MS/MS values, obtained as number of exclusive ANXA6 peptides (top) or normalized quantitative values (bottom).

Supplementary Table 4
List of antibodies used in flow cytometry (FC), immunofluorescence (IF), Western blotting (WB) and ELISA analyses
The table shows a comprehensive list of antibodies used in the study.

Supplementary Table 5
Statistics Source Data
Numerical values for all data shown in the main and supplementary figures.

References

58 Kitamura, T. *et al.* Monocytes Differentiate to Immune Suppressive Precursors of Metastasis-Associated Macrophages in Mouse Models of Metastatic Breast Cancer. *Front Immunol.* 8, 2004 (2017).

59 Xu, J. Preparation, culture, and immortalization of mouse embryonic fibroblasts. *Curr Protoc Mol Biol* Chapter 28, Unit 28 21, doi:10.1002/0471142727.mb2801s70 (2005).

60 Squadrito, M. L. *et al.* Endogenous RNAs modulate microRNA sorting to exosomes and transfer to acceptor cells. *Cell Rep.* 8, 1432-1446 (2014).

61 De Palma, M. & Naldini, L. Transduction of a gene expression cassette using advanced generation lentiviral vectors. *Methods Enzymol* 346, 514-529 (2002).

62 Cianciaruso, C. *et al.* Primary Human and Rat beta-Cells Release the Intracellular Autoantigens GAD65, IA-2, and Proinsulin in Exosomes Together With Cytokine-Induced Enhancers of Immunity. *Diabetes* 66, 460-473 (2017).

63 Chiou, N.-T. & Ansel, M.K. Improved exosome isolation by sucrose gradient fractionation of ultracentrifuged crude exosome pellets. *Protocol Exchange* DOI:10.1038/protex.2016.057(2016).

64 Gray, C. *et al.* Simultaneous intravital imaging of macrophage and neutrophil behaviour during inflammation using a novel transgenic zebrafish. *Thromb Haemost.* 105, 811-819 (2011).

65 Motoike, T. *et al.* Universal GFP reporter for the study of vascular development. *Genesis* 28, 75-81 (2000).

66 Keklikoglou, I. *et al.* Periostin Limits Tumor Response to VEGFA Inhibition. *Cell Rep.* 22, 2530-2540 (2018).

67 de Araujo, M. E., Lamberti, G. & Huber, L. A. Isolation of Early and Late Endosomes by Density Gradient Centrifugation. *Cold Spring Harb Protoc* 2015, 1013-10164 (2015).

68 Chopra, T. *et al.* Quantitative mass spectrometry reveals plasticity of metabolic networks in Mycobacterium smegmatis. *Mol Cell Proteomics* 13, 3014-3028 (2014).

69. Consortium, E.-T. *et al.* EV-TRACK: transparent reporting and centralizing knowledge in extracellular vesicle

research. *Nat Methods* 14, 228-232 (2017).
70 Vizcaino, J. A. *et al.* 2016 update of the PRIDE database and its related tools. *Nucleic Acids Res* 44, 11033 (2016).